Shelf, Shear and Staircases: Glider Observations in the North Atlantic

A thesis submitted to the School of Environmental Sciences of the University of East Anglia in partial fulfilment of the requirements for the degree of Doctor of Philosophy

Callum Rollo

June 2022

.

Supervisory Team

Karen J. Heywood
Rob A. Hall

Centre for Ocean and Atmospheric Sciences
School of Environmental Science
University of East Anglia
Norwich, UK

Alexander B. Phillips

Marine Autonomous Robotic Systems
National Oceanography Centre
Southampton, UK

Abstract

Ocean gliders have established themselves as a key component of the Global Ocean Observing System. Gliders are particularly useful in shelf-break areas that cannot be surveyed by profiling floats, such as those of the Argo program. This thesis uses a legacy glider dataset to examine shelf break processes in an upwelling zone. This dataset covers two periods of upwelling over the NW Iberian margin in summer 2010. During this deployment, equatorward transport was maintained over the shelf for 70 days during one of the strongest upwelling seasons on record.

Using a dataset collected by three gliders in the tropical North Atlantic, a new algorithm for identifying thermohaline staircases in glider data is described. Applying this algorithm, over 14000 thermohaline steps are identified in profiles from the three gliders. It is hypothesised that the incidence of thermohaline staircases is limited by strong background gradients in conservative temperature and absolute salinity. Additionally, fast-response thermistor data are used to examine the sensitivity of automated thermohaline staircase classifiers to the vertical resolution of temperature and salinity profiles. In this analysis, a large number of small thermohaline steps ($<$ 1 m) were found where background gradients of temperature and salinity are strong. These steps are below the detection resolution of Argo floats and are likely underestimated in Argo based surveys.

The use of gliders to collect temperature and salinity profiles for extended periods of time is well established. This thesis examines two new technologies that have recently been applied to gliders: acoustic Doppler current profilers (ADCPs) and automated classification algorithms. The integration of a 1 MHz ADCP into a Seaglider is described, along with the tests, trials, and results of four deployments. The challenges of this sensor integration are explored, with recommendations made for future use of the glider and suggested improvements to the ADCP. In particular, the recommendation is made to increase the beam angle of the ADCP from 17.4 ° to 22 ° to avoid glider stalling. This work includes the production of a user manual for future users of the ADCP glider.

Contents

List of Figures

List of Tables

List of Acronyms

ADCP	Acoustic Doppler Current Profiler
AD2CP	Acoustic Doppler Dual Current Profiler (Nortek 1 MHz ADCP)
AUV	Autonomous Underwater Vehicle
BEAM	Coordinate system where each vector is along an ADCP beam
C-SALT	Caribbean-Sheets and Layers Transect
CAIBEX	Canaries-Iberian Marine Ecosystem Exchanges
CTD	Conductivity, Temperature and Depth
DAC	Dive Average Current
DVL	Doppler Velocity Logger
ENACW	Eastern North Atlantic Central Water
ENACW$_{sp}$	subpolar Eastern North Atlantic Central Water
ENACW$_{st}$	subtropical Eastern North Atlantic Central Water
ENU	Coordinate sytem aligned with Earth: East North Up
ERDDAP	Environmental Research Division's Data Access Program
EUREC^{4}A	Elucidating the Role of Clouds-Circulation Coupling in Climate
GNSS	Global Navigation Satellite System
GOOS	Global Ocean Observing System
GPS	Global Positioning System
IPC	Iberian Poleward Current
LADCP	Lowered ADCP
MARS	Marine Autonomous and Robotic Systems
MEDW	Mediterranean Water
NERC	Natural Environment Research Council
NEXUSS	Next Generation Unmanned Systems Science
NMEA	National Marine Electronics Association
NOCS	National Oceanography Centre Southampton
NRT	Near Real-Time
NVRAM	Non-Volatile Random-Access Memory
NWIM	North West Iberian Margin
PIES	Pressure Inverted Echo Sounder

PLOCAN	Plataforma Oceánica de Canarias
QC	Quality Control
RV	Research Vessel
SAMS	Scottish Association for Marine Science
SOCIB	Sistema d'observació i predicció costaner de les Illes Balears
SG637	Seaglider number 637 Omura. ADCP glider
SST	Sea Surface Temperature
UEA	University of East Anglia
UI	Upwelling Index
UW	Univerity of Washington
VDB	van der Boog et al. (2021b)
vmADCP	Vessel Mounted ADCP
XBT	Expendable bathythermographs
XYZ	Coordinate system oriented with X toward glider nose
YD	Yearday (0 indexed)

Symbols and units

σ_θ	Potential density anomaly
$\Delta(O_2)$	Oxygen supersaturation
$\phi_{heading}$	Heading angle
ϕ_{pitch}	Pitch angle
ϕ_{roll}	Roll angle
l	Distance between transducer and scatterer
z_x	Vertical seperation between transducer x and scatterer
θ_x	angle of beam x from vertical
R_ρ	Density ratio
Tu	Turner angle
α	Thermal expansion coefficient of water
β	Haline contraction coefficient of water
θ	Conservative temperature
S	Absolute salinity
u_h	Eastward velocity at depth h
u_r	Reference velocity
g	Gravitational acceleration
f_0	Local Coriolis parameter
ρ	In-situ density
ϑ_{fa}	Angle to the vertical of fore and aft beams
ϑ_{ps}	Angle to the vertical of port and starboard beams

Acknowledgements

A thesis cover carries only one name, however, no piece of work is an island. This thesis would not have been possible without the guidance, support and encouragement of a host of people. I want give thanks to some of these wonderful people in particular.

First and foremost to my supervisors Karen, Rob and Alex, for believing in me even when I didn't. I couldn't have asked for better. To Gareth and Marcos, for good humoured support and letting me mess around for interminable weeks in their workshop, and on the glider base station, trying to "improve' things. To all the members of the UEA glider group, past and present, for leading the way and making the journey enjoyable.

A big thank you to everyone who ever took time to teach, coach, and mentor others. To Torvalds, Van Rossum, Elbakyan, and the greater open source community. To those who stood as role models for me, knowingly or otherwise: Bastien, Maia, Denis, Filipe and more. To the UEA Scientific Python group, for introducing me to the wonderful world of collaborative coding and helping me find my passion for programming. Each one teach one. Thanks to all the coders who answer questions on stack overflow. The real heroes.

To my family, particularly my mother Sarah Rollo, for baking, proofreading services, and reminders that I still have at least one peer reviewed publication to go before being the most academic Rollo.

Finally to my Norwich friends who joined me cycling, drinking, gaming, kayaking, camping, and making this Fine City a home.

This work was funded by the Natural Environment Research Council (Grant NE/N012070/1) and the Engineering and Physical Sciences Research Council, via the NEXUSS Centre of Doctoral Training in the Smart and Autonomous Observation of the Environment.

1

Introduction

1.1 Currents and velocity shear in the ocean

The ocean plays a critical role in the Earth system through the transport of ocean currents. Heat and salt, oxygen and nutrients, phytoplankton and fish larvae, are all transported by ocean currents. Currents in the ocean drive processes at all scales, from the global ocean conveyor belt and basin scale gyres, to the millimetre scale vorticity features of ocean mixing. These ocean currents exert a strong influence over our society as well (Szuts et al., 2019). From the immediate impact of currents winnowing away the foundations of wind farms to the climate of Europe kept mild by the Gulf Stream, ocean currents affect us all.

At first glance, an observer might assume that currents in the ocean are vertically uniform. Most of our direct observations of the ocean are from the beach, a ship or a plane. The ocean's relative opacity to the electromagnetic spectrum, including visible light, makes measurements of its interior difficult. It is reasonable to look at a feature such as the Gulf Stream and assume that the strong surface poleward current extends all the way down to the sea-floor. However, this is not the case. Underneath the Gulf Stream, a system of counter currents transports water equatorward (Buckley and Marshall, 2016). Vertical variation, or "shear", of horizontal currents is in fact the norm in the ocean. What we observe at the surface does not represent the motion at depth.

Measuring and velocity and velocity shear in the ocean is expensive and difficult. Sending a research vessel to the middle of an ocean basin to winch sensors down through kilometres of water is a technical challenge. The results of this work are only isolated measurements over a limited time period. Observations are particularly sparse near the poles, and during the winter months when ship work is hazardous. By necessity, we estimate and extrapolate from the limited observations we have, but ocean currents are anything but homogeneous or constant. Currents in the ocean vary over timescales of days to years (Davis, 2010; Buckley and Marshall, 2016). We need to observe ocean currents, not just in isolated points over limited time periods, but synoptically.

Since the turn of the century, two novel platforms for ocean observing, argo floats and ocean gliders, have been developed to fill this observational gap. Starting in 1999, the Argo program has used autonomous profiles float to massively increase the number of observations of the open ocean. These autonomous floats have collected over two million profiles (NOAA, 2018). Ocean gliders (described in Section 1.6) are controllable buoyancy powered platforms that can operate in more dynamic environments such as shelf breaks which are not accessible to Argo floats (Testor et al., 2019). Chapter 2 details the results of a glider study in such a shelf break environment. Chapter 3 builds directly on a methodology developed for Argo data to classify thermohaline staircases in glider datasets.

Both of these studies focus on the long term observation of currents and shear structures using temperature and salinity data. Chapter 4 describes an attempt to integrate an ADCP into a glider to observe such processes directly. In the following sections, I provide an overview of the most popular methods used to observe ocean currents, their respective benefits and limitations.

1.2 Indirect estimation of velocity shear

In the open ocean, away from boundaries and with with negligible vertical velocities, ocean velocities are assumed to be governed by the geostrophic approximation. Under these conditions, the Navier-Stokes equations in the horizontal plane reduce to:

$$u_h = \frac{g}{f_0 \rho_0} \int_0^h \frac{\partial \rho}{\partial y} dz + u_r$$

$$v_h = -\frac{g}{f_0 \rho_0} \int_0^h \frac{\partial \rho}{\partial x} dz + v_r$$

Where u_h and v_h are eastward and northward velocity at depth h, g is acceleration due to gravity, f_0 is the local Coriolis parameter (assumed constant), ρ_0 is average density, ρ is density and u_r and v_r are reference velocities at depth. Using the geostrophic approximation, shear of meridional velocity can be calculated from gradients of zonal density and vice-versa. This approach is limited to areas of the ocean in geostrophic balance, and depends on the assumption of a depth of no motion or assumed constant current in order to yield absolute velocities. In many cases these conditions cannot be met. For example near the equator where $f \to 0$, near boundaries where friction plays a non-negligible role, in Ekman layers, or at scales below the Rossby radius of deformation. In these cases, direct observation with an ADCP or other instrument is the only way to determine water velocities.

The geostrophic approximation is commonly used, as estimates of density have been historically easier to collect than direct velocity measurements. It requires only temperature, salinity and pressure. Geostrophy is used successfully, particularly in basin scale observations, to estimate velocities and transports, e.g. the Atlantic meridional overturning circulation (Smeed et al., 2014). All the observations necessary to approximate geostrophic velocities can be collected using ships, moorings, profiling floats and gliders. This is the method used to estimate along shelf transports in Chapter 2.

1.2.1 Use of a glider to estimate geostrophic alongshore flow

Chapter 2 describes the use of a glider to estimate along shelf transports using the velocity shear method from geostrophic currents. This deployment was carried out over the North West Iberian Margin (NWIM), a region with a set of cross poleward and equatorward currents. These currents are shown in Figure 1.1, after Ferreira Cordeiro (2018). The system of currents established during summer upwelling periods has been well studied (Arístegui et al., 2009; Nolasco et al., 2013; Teles-Machado et al., 2015). However, the the week long cruises and isolated moorings have not been able to capture the full variation of the upwelling system over the duration of a summer upwelling season.

A glider deployment during two months of the summer upwelling season was able to capture more variability in alongshore flows and oxygen concentration than previous, isolated ship based surveys. During periods of upwelling, alongshore currents change over a timescale of a few days and cold upwelled waters drive increased productivity. This study demonstrated the utility of gliders as long term monitoring platforms for geostrophic estimates of transport.

This system of geostrophic alongshore currents is an ideal study site for a cross-shelf glider transect to estimate transports from geostrophy. However, this method cannot capture ageostrophic currents, which would require direct observation from an instrument like an ADCP. This study proved that gliders can operate in these dynamic environments, with some limitations. In particular, the glider struggled to maintain its cross shore transect when currents exceeded 0.2 m s^{-1} and could not sample inshore of the 50 m isobath. The limits of glider observations are discussed in the chapter. The uncertainty around transport estimates from geostrophy makes the case for the dpeloyment of an ADCP glider in this environment.

1.3 Small scale shear and velocity

Fine scale shear is a key driver of turbulent mixing in the ocean interior. This phenomenon occurs over scales that are not observable by long range ADCPs, which have bin sizes of several metres. A pronounced example of this is thermohaline staircases. These structures occur over large areas of the open ocean and are made up of mixed layers serveral 10s of ms thick separated by gradient layers that can be less than 1 m thick. These layers of fine scale shear cannot be observed by ship based ADCPs, but can be observed by an ADCP glider. The contribution of staircases to global estimates of mixing is small, estimated at around 7.5 GW (van der Boog et al., 2021a). However, this estimate is based on Argo data binned at 1 dbar resolution. Analysis of data

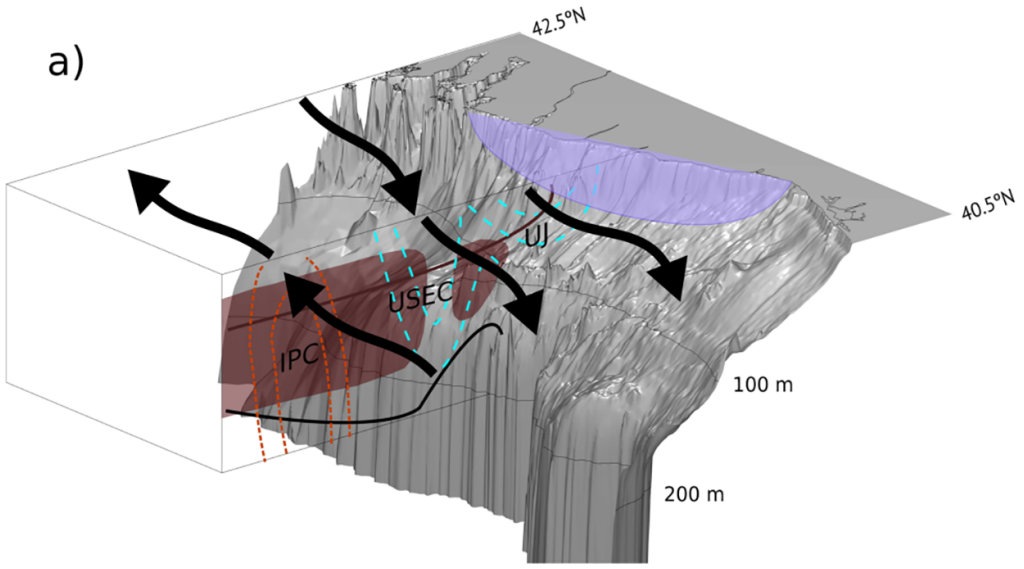

Figure 1.1: The main alongshore currents during an upwelling period on the NWIM. These are the Iberian Poleward Current (IPC), the Upper Slope Equatorward Current (USEC) and Upwelling Jet (UI). The blue shaded region represents cold, upwelled water. Adapted from Ferreira Cordeiro (2018).

binned at 0.2 m showns a large number of small steps below the detection threshold of more coarsely binned data. Consequently, previous attempts to estimate the global contribution of staircases to global mixing could be underestimating this due to missing small steps.

1.3.1 Gliders to classify thermohaline staircases

A recent study by van der Boog et al. (2021b) demonstrated the use of Argo floats to classify thermohaline staircases that occur across large areas of the global ocean. These features are widespread, but relatively poorly studied. The last dedicated study of thermohaline staircases in the tropical North Atlantic was C-SALT in 1987 (Schmitt et al., 1987). In Chapter 3 we use data from three gliders in the tropical Atlantic to build on this study, automatically classifying staircases from glider data comprising over 1000 profiles of temperature and salinity. The use of an automated classifier removes the subjective element of classifying staircases and enables efficient analysis of the large number of profiles collected by the three gliders during a month long deployment .

Using temperature and salinity profiles, it is possible to estimate shear and mixing in thermohaline staircases Schmitt et al. (1987). Using an ADCP glider to directly observe the shear in these staircases would give more accurate measures of shear and could elucidate the reasons for the differences between theoretical and laboratory based staircases, and those observed in the global

ocean. In particular, the highly sheared gradient layers of thermohaline staircases in the ocean are typically an order of magnitude thicker than predicted by laboratory studies Schmitt et al. (1987). Direct observations of velocity at the small scale of these layers (2 - 5 m in thickeness) would help to clarrify the dynamics that are inferred from temperature and salinity profiles.

1.4 ADCPs

The most commonly used instrument for observing ocean currents is the acoustic Doppler current profiler (ADCP). There are many designs of ADCP used to measure ocean velocity across a range of scales from a wide variety of platforms. These include research vessels, moorings, buoys, and autonomous underwater vehicles (AUVs). Though they vary widely in size and appearance, all ADCPs work in a similar manner, using the Doppler effect. This is the effect that relative motion has on reflected sound waves. The sound waves reflected from an object moving toward a sound source will have a smaller wavelength, and correspondingly greater frequency than the originally emitted sound waves. This is the same effect behind the apparent shift in tone of a source such as a siren moving past an observer, and the red shift of distant galaxies. This change in reflected wavelength and frequency is used to calculate the velocity of the reflector relative to the source of the sound waves.

An ADCP has one or more transducers. Each of these transmits short bursts of acoustic energy. This energy travels as sound waves that propagate through the water column and are reflected by suspended solid particles or bubbles. The same transducer measures the reflected sound wave and uses the change in wave frequency to deduce the speed of the reflector relative to the transducer. The time taken for the sound wave to return is multiplied by the local sound speed to estimate the distance between the transducer and reflector. In this manner, time gated returns are used to estimate relative velocities at set distances from the transducer.

ADCPs do not measure the speed of water directly, rather the speed of particles suspended within it. For this reason, ADCPs perform poorly in water with few scatterers, such as the oligotropic open ocean, and in the near surface where entrained bubbles impede acoustic waves (Todd et al., 2017). Multiple transducers are typically employed, as each transducer can only estimate speed in the along-beam direction. A minimum of three transducers are required to determine the 3D movement of water relative to the ADCP. Most designs use four or five transducers for redundancy and increased accuracy e.g. the Teledyne RDI Ocean Surveyor (4 transducers), or Nortek Signature (5 transducers). For more details on the technical operation of ADCPs, including

an explanation of broadband operation and phase shift, consult the Teledyne RDI ADCP primer (Teledyne RD Instruments, 2011).

1.4.1 Ship borne ADCPs

Most modern research vessels are fitted with a vessel mounted ADCP (vmADCP). These are integrated into the ship's hull, sometimes on a drop keel. This can be lowered to stabilise the vessel and put more distance between acoustic sensors and surface sources of acoustic noise and cavitation from propellers. Vessel mounted ADCPs have several advantages. Being ship mounted, energy consumption and data storage are not typically a concern. Compared to other active acoustic instruments, such as the towed arrays used in seismic surveying, ADCPs are small instruments. Even the largest commercially available vmADCPs that operate at 36 kHz, and can observe currents up to a kilometre beneath the vessel, are comprised of transducers less than 1 m in diameter. vmADCPs also benefit from the high accuracy and sampling frequency of ship Global Navigation Satellite Systems (GNSS) such as GPS (USA) and Galileo (EU).

vmADCPs do have some drawbacks. Surface vessels pitch and roll at a variety of frequencies; correcting for these in the vmADCP data is critical and non trivial (Humon, 2021). On a large vessel in moderate swell, the flexing of the vessel can cause misalignment between the vmADCP and the GNSS receiver, which must be corrected for. Owing to their mounting below a vessels waterline, vmADCPs cannot sample the uppermost part of the water column, typically missing the uppermost 10 metres or more. Finally, vmADCPs are limited to the depth range of the sensor. Under ideal conditions, vmADCPs can collect data up to 1200 m below the surface, leaving most of the ocean unobserved. To increase the range of ADCP sampling from a ship, ADCPs are mounted on a CTD rosette, this is referred to as a lowered ADCP (LADCP).

LADCPs have a much greater range than vmADCPs. They are able to sample the water column from the surface down to the maximum extent of the CTD winch cable, plus the range of the ADCP. LADCPs typically use smaller, higher frequency transducers of 150 or 300 kHz. This decreases the bin size of the collected data, increasing its resolution. The processing of LADCP data is standardised, with many authors following the method of Thurnherr et al. (2010). LADCPs have a far greater combined range, achieved by overlapping profiles. However, the resulting data can be difficult to process as the CTD rosette is subject to the ship's motions transmitted via the cable, while its movement relative to earth is not known to the same accuracy as the ship's. In character and processing, an ADCP mounted on a glider is most similar to an LADCP.

1.4.2 ADCPs vs DVLs

ADCPs and Doppler velocity loggers (DVLs) are very similar instruments. Both employ multiple acoustic transducers in a diverging convex geometry. The principle difference is that DVLs measure only one velocity along each beam, typically from a known reflector such as the seafloor, to estimate the relative velocity between the DVL unit and the reflector. DVLs are principally used for navigational purposes. Because they provide only one measurement of velocity, that of water or ground relative to the platform, DVLs do not provide any information about the velocity shear of the water column. They can provide a single measurement of water velocity V_w if the velocity of the vehicle relative to the ground V_g is independently known, for instance via a GNSS transceiver. The terms DVL and ADCP are often used interchangeably, even when referring to the same instrument (e.g. Cusi et al. 2017). In this thesis, ADCP refers to an instrument than time gates acoustic returns from an emitted acoustic pulse into bins at approximately fixed distances from the transducer. A DVL measures the relative velocity of the platform and a single reflector.

1.5 From shear to velocity

Whether measured by ADCP or deduced from the geostrophic approximation, vertical profiles of horizontal velocity shear must be integrated to estimate velocity. Two methods are commonly used for this combination of overlapping shear profiles: vertical integration of shear and the velocity inversion method. Vertical integration of shear simply integrates shear estimates vertically from a known velocity such as a depth of no motion or a bottom lock. One of the most popular methods is described by Thurnherr et al. (2010) as used for LADCP data. The same approach can be used for ADCP data from AUVs. Velocity inversion is a more complex procedure that treats each estimate of local shear separately, creating a linear series of equations that can be solved by a least squares calculation (Todd et al., 2017)

The advantage of the velocity inversion method is that many constraints can be applied during the inversion with linear additions, while the simpler shear method requires extensive post processing to achieve this. The two methods are contrasted in detail in Thurnherr et al. (2015).

The vertical profiles of horizontal velocity produced by these methods are relative. To obtain absolute (earth relative) velocity, we must reference the velocity profile to a known velocity. This can be achieved with a velocity at a known depth or through the use of a depth averaged velocity integration constant. Known velocities are commonly used in shallow water environments, where ADCPs can

obtain a "bottom lock" on the sea-floor, or in deep quiescent environments where a depth of no motion can be assumed (Fong and Monismith, 2004). In the open ocean, it is more common to use a depth average current. Reference to depth average current is the approach employed most commonly when analysing data from gliders (Rusello et al., 2012; Todd et al., 2017).

1.6 Gliders primer

Ocean gliders are small, buoyancy powered vehicles that profile with a characteristic sawtooth sampling pattern (Figure 1.2). Gliders use short wings to transform vertical speed into horizontal motion. The first gliders were produced at the turn of the century and now, after 20 years of development, they are an established platform for oceanographic research and monitoring. Gliders are a keystone of the Global Ocean Observing System (GOOS) (Testor et al., 2019). Gliders are capable of long endurance deployments, profiling the upper 500 - 1500 m of the ocean at a fraction of the cost of a dedicated research vessel. Gliders are more limited in scope than research vessels, typically only measuring a few variables and with no sample collection ability. Gliders require deployment and recovery from a vessel in at least 50 m of water at the beginning and end of their 1 - 3 month long missions. The geostrophic method has been used to indirectly estimate current velocities from gliders since their inception, but the use of ADCPs on gliders is a relatively recent development.

A key concept in the operation of gliders is the flight model described in Frajka-Williams et al. (2011). Between the surface GPS fixes at the beginning and end of each dive, the glider has no direct method of determining its location. Instead, the motion of the glider through the water is estimated indirectly. Vertical speed is calculated from pressure changes and horizontal speed is estimated from the glider's pitch angle and angle of attack. Using the heading from the glider's compass, one can establish its course through the water. This method is referred to as dead reckoning. When the glider surfaces and achieves a GPS fix, the distance travelled relative to the earth is established. The difference between these two distances is the displacement of the water while the glider was submerged. Dividing this discrepancy by the dive time yields an approximate water velocity. This velocity is referred to as dive average current (DAC). Assuming that the glider dive was conducted at a constant vertical speed, this DAC is approximately a depth averaged current over the vertical extent of the dive. This DAC is used to reference geostrophic shear from gliders and is considered to be accurate to 1 cm s^{-1} (Eriksen et al., 2001; Merckelbach et al., 2008).

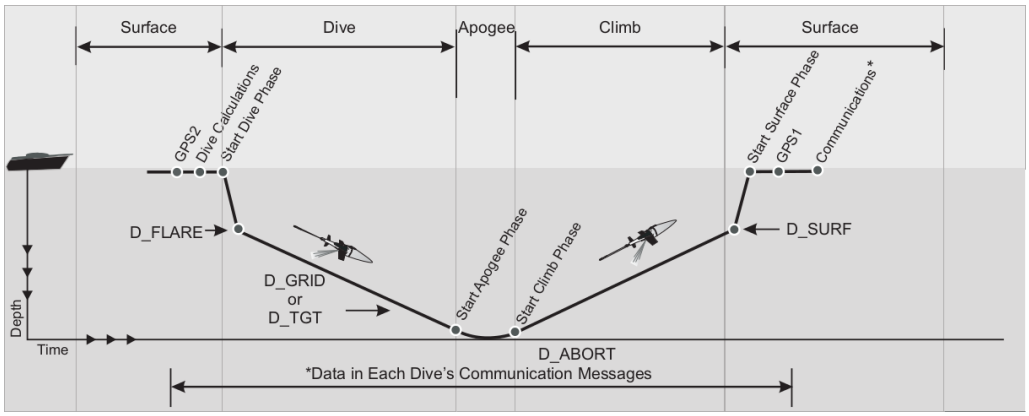

Figure 1.2: The standard shape of a glider dive, including GPS fixes which are used to calculate dive average current. From IRobot (2012)

1.7 Thesis overview

This PhD project was funded by the Next Generation Unmanned Systems Science (NEXUSS) Centre for Doctoral Training. NEXUSS was created to tackle challenges in the environmental sciences via the use of smart and autonomous observing systems. Observational campaigns in physical oceanography are increasingly centred on autonomous observing systems such as profiling floats and gliders. Over the last two decades, gliders have evolved from specialist experimental vehicles to proven, reliable platforms suitable for integration with a wide range of sensors. Experimenting with new sensors and sampling strategies can increase the volume and range of observational data collected by these platforms. This enables a greater insight into underlying oceanographic processes. Chapter 4 describes the process of integrating, testing, and deploying the ADCP Seaglider SG637 Omura, along with preliminary data analysis. Chapter 5 is a manual of operation for this ADCP glider, compiled from extensive testing and deployment of the system.

The testing of Omura required several field deployments over three years. During this time, previously unpublished collected by a standard glider, SG510 Orca, was used to study a shelf-break region which could be the subject of future ADCP-glider deployments. This was a shelf break study of the Iberian margin near Vigo, Spain in summer 2010. This campaign focused on upwelling and alongshore geostrophic flows as part of the Canaries-Iberian Marine Ecosystem Exchanges (CAIBEX) project. We observed continuous equatorward transport over the shelf and upper slope during 70 days, due to unusually persistent upwelling favourable conditions. Two periods of strong southward winds precipitated upwelling events observed by the glider. We recorded peaks in chlorophyll *a* leading peaks in dissolved oxygen in near surface waters. The results of this work are presented in Chapter 2. The contents of this chapter were published in 2020 by the American

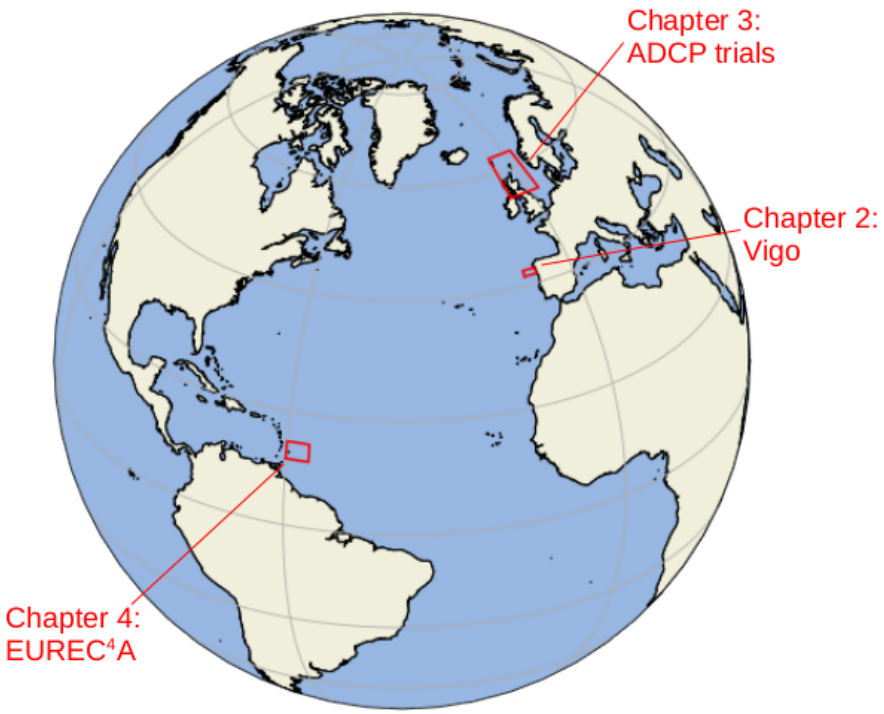

Figure 1.3: Map showing areas of glider deployments covered by the three following chapters of this thesis.

Geophysical Union in JGR: Oceans (Rollo et al., 2020a).

After extensive testing, Omura was deployed east of Barbados for three weeks in January 2020. This deployment was carried out as part of the Elucidating the Role of Clouds-Circulation Coupling in Climate (EUREC^{4}A) campaign. Results from EUREC^{4}A are presented in Chapter 3. During this deployment, we observed two periods of thermohaline staircasing at the edge of the region identified in the C-SALT experiment 35 years prior. To quantify the extent and step characteristics of these structures, I created a classification algorithm to detect thermohaline staircases in glider data. Using this dataset, we hypothesise four criteria that must be met for extensive thermohaline staircases to form and persist. This chapter was submitted to the European Geosciences Union journal Geoscientific Instrumentation, Methods and Data Systems in October 2021.

The key theme linking these glider deployments is improving the methodology for observing ocean currents and shear over a range of scales. Fine scale shear is a key driver of turbulent mixing in the ocean interior, as explored in Chapter 3. This mixing occurs at scales too small for ship mounted ADCPs, but could be

directly observed by an ADCP equipped glider. Large scale geostrophic currents can be monitored by gliders, as shown in Chapter 2. An ADCP equipped glider could extend this analysis into ageostrophic flows. Both of these studies make the case for gliders as a part of the global ocean observing systems filling the gap between long duration, low temporal resolution Argo floats and tradional ship based observations.

Chapter 6 reviews the progress made with Omura and automated glider data processing over the course of this PhD. I discuss the core challenges of integrating an ADCP onto a Seaglider and make recommendations for future work, with a particular focus on Omura.

2

Glider Observations of the Northwestern Iberian Margin During an Exceptional Summer Upwelling Season

2.1 Key points

- A glider observed two upwelling events during a 70 day deployment over the Northwestern Iberian Margin in summer 2010.
- During upwelling, decreasing temperature and increasing chlorophyll a concentration lead increasing dissolved oxygen concentration by 6 days.
- Equatorward flow persisted over the shelf and upper slope throughout the deployment.

2.2 Abstract

Glider observations from the Northwestern Iberian Margin during the exceptionally strong 2010 summer upwelling season resolved the evolution of physical and biogeochemical variables during two upwelling events. Upwelling brought low oxygen Eastern North Atlantic Central Water from 190 m depth onto the shelf up to a depth of 50 m. During the two observed periods of upwelling, a poleward jet developed over the shelf break. The persistent southward, upwelling favourable winds maintained equatorward flow on the outer shelf for two months with no reversals during relaxation periods, a phenomenon not previously observed. During upwelling, near surface chlorophyll *a* concentration increased by more than 6 mg m^{-3}. Oxygen supersaturation in the near surface increased by more than 20 %, 6 days after the chlorophyll *a* maximum.

2.3 Plain language summary

In summer 2010, an autonomous underwater vehicle was used to measure changing water properties in the ocean offshore of Vigo, NW Spain. During summer, winds blowing southward along the Iberian coast push surface waters offshore, causing deep, cold, nutrient rich water to rise to the surface. The nutrients brought up with this cold water enable growth of phytoplankton, impacting higher trophic levels and local fisheries. During June and July 2010 we observed two episodes of deep water rising and the subsequent increases in phytoplankton. Increases in dissolved oxygen concentration and ocean current speed were also observed. Using a robotic underwater glider allowed us to obtain high resolution observations over a longer time period at a fraction of the cost of a research vessel cruise.

2.4 Introduction

Eastern Boundary Upwelling Systems are some of the oceans' most productive areas, covering less than 1 % of the ocean but accounting for up to 20 % of the global wild fish take (Pauly and Christensen, 1995). The Northwestern Iberian Margin (NWIM) forms the northernmost extent of the Canary Current Upwelling System, an Eastern Boundary Upwelling System of the North Atlantic. The NWIM hosts a seasonally varying multicore flow that exhibits strong variability (Teles-Machado et al., 2015). With the northward movement of the Azores High and the intensification of the Icelandic Low in summer, episodic southward winds blow along the Iberian coastline (Peliz et al., 2002; Nolasco et al., 2013). These southward winds drive warm surface waters offshore by Ekman transport, inducing the upwelling of cooler, nutrient rich water from as deep as 200 m and enhancing local primary production (Barton, 2001). During upwelling periods, typically 7-10 days (Huthnance et al., 2002; Ferreira Cordeiro et al., 2018), the coastal sea level lowers, the thermocline rises and an equatorward coastal jet develops over the shelf (Arístegui et al., 2009).

The NWIM extends 350 km along the west coast of the Iberian peninsula, from Cape Mondego to Cape Finisterre (Figure 2.1). The NWIM consists of a shelf 50-60 km wide that slopes gently to the shelf break between the 200 and 300 m isobaths before dropping to 2000 m over a distance of 15 km. The glider deployment area, in the neighbourhood of Cape Silleiro, is known to feature intensified upwelling in summer (Huthnance et al., 2002; Relvas et al., 2007). The shelf and slope region host seasonally varying meridional flows detailed by Herrera et al. (2008); Ferreira Cordeiro et al. (2018). Offshore, the North Atlantic subtropical gyre transports water equatorward in the broad, slow Portugal Current (Arístegui et al., 2009). The most variable current over the slope is the Iberian Poleward Current (IPC). The IPC transports water poleward, primarily driven by meridional density gradients (Peliz, 2003). During summer, this poleward flow coexists with two equatorward flows, the Upper Slope Equatorward Current, a topographically steered jet along the slope, and the intermittent Upwelling Jet that transports shelf waters equatorward (Ferreira Cordeiro et al., 2018). These currents are shown in schematic in Figure 1.1. The current closest to the coast is the UI, the USEC lies over the upper contiental slope, with the IPC further offshore. Glider data in Figure 2.1.a show the UI at the eastern end as the strongest equatorward current, and the USEC over the slope. The glider did not travel far enough offshore to directly observe the IPC.

Upwelling is a response to atmospheric forcing. When southward winds blow along the coast of the NWIM, surface waters are transported offshore by Ekman

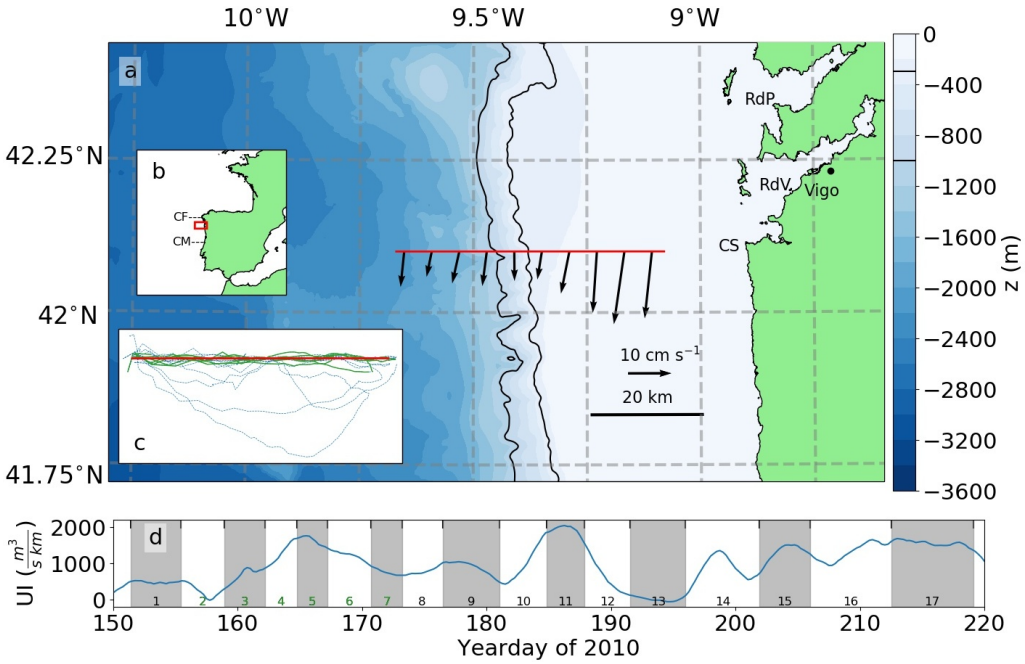

Figure 2.1: (a) Location of the glider section offshore of Vigo, NW Spain. Grey dashed lines at 1/4 degree intervals. Black lines demarcate the 300 and 1000 m isobaths, the shelf break and maximum profiling depth of the glider respectively. Red line marks the glider's nominal section. Arrows are the detided dive average currents, averaged over the deployment. Cape Silleiro is marked with CS. The mouths of the two southern Rías Baixas estuaries are marked: the Ría de Pontevedra (RdP) and Ría de Vigo (RdV). Bathymetry from the EMODnet Bathymetry Consortium (2018). (b) Limits of the Northwestern Iberian Margin, Cape Finesterre (CF) in the north and Cape Mondego (CM) in the south. Red box is area shown in (a). (c) Track of the glider during its 17 transects of the section, same scale as (a). Glider's nominal section in red. Green lines are transects 2-7. (d) Upwelling Index (UI) calculated with winds from the FNMOC model over yeardays 150-220 (30 May to 9 August) 2010. Shading shows the timing of the 17 numbered glider transects. Background shading indicates the direction of glider travel (grey: westward transects, white:eastward transects).

transport. These waters are replaced by cooler subsurface waters that rise to replace them. Equatorward flow then develops centered on the front between warm surface waters that have been displaced offshore and cool, dense subsurface waters that have replaced them. This current is the UI and is in geostrophic balance, running equatorward parallel to the coast (Fiuza et al., 1998). The front typically moves offshore as more cool water is upwelled (Ferreira Cordeiro, 2018).

Three water masses are typically observed in the upper 1000 m over the NWIM. In the deeper waters over the slope, Mediterranean Water (MEDW) is observed, typically below 550-600 m (Fiuza et al., 1998; van Aken, 2000). Above the

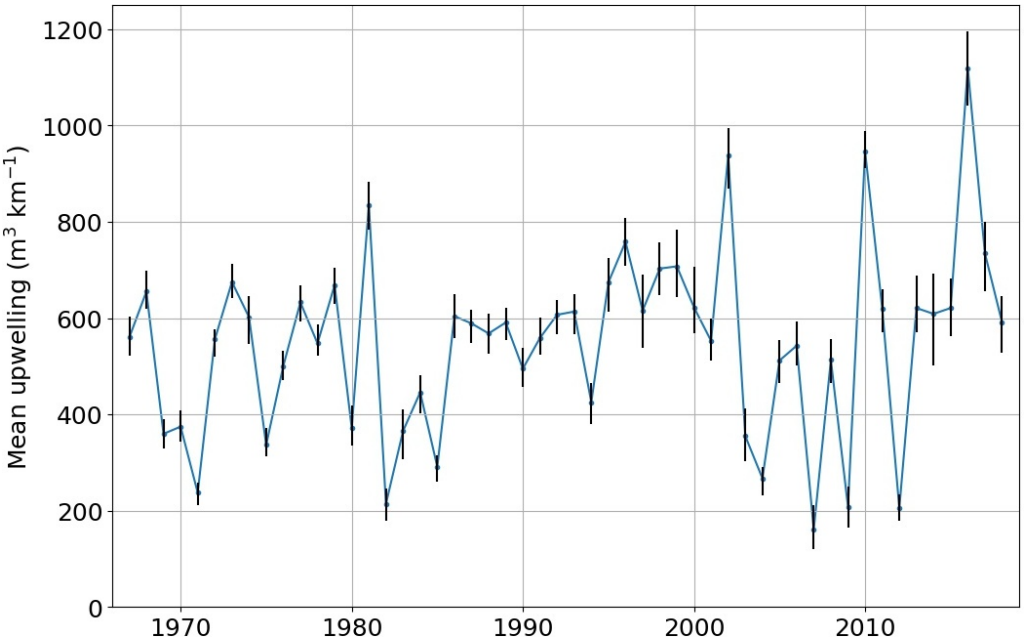

Figure 2.2: Mean and bootstrapped uncertainty range of the Upwelling Index for the 70 day interval 30 May to 8 August inclusive of each year.

MEDW two modes of Eastern North Atlantic Central Water (ENACW) are distinguishable; the subpolar ($ENACW_{sp}$) and subtropical ($ENACW_{st}$) modes (Ríos et al., 1992). The two converge in the vicinity of Cape Finisterre around 42-44 °N (Peliz et al., 2002) and are approximately divided along $\sigma_\theta = 27.1$ kg m^{-3}. The overlying $ENACW_{st}$ is warmer, saltier and more oxygen rich than $ENACW_{sp}$, as has been observed elsewhere in the north east Atlantic (Damerell et al., 2016; Ferreira Cordeiro et al., 2018; Hall et al., 2017). $ENACW_{sp}$ is typically observed from depths of 550-600 m up to 250-180 m. $ENACW_{st}$ is observed higher in the water column, from 250 m to 20-70 m where it mixes with warm, brackish outflow of the Rías Baixas estuarine inlets to form the surface waters of the upper 20-70 m. These light surface waters flow offshore past the shelf break. The surface waters are the warmest and most highly oxygenated waters of the NWIM. In summer, much of the vertical displacement of these water masses is driven by upwelling events (Álvarez-Salgado et al., 2000).

Upwelling episodes boost productivity along the shelf break, increasing primary production by up to 50 % compared with open ocean values (Joint et al., 2002). Due to upwelling, the NWIM hosts high concentrations of zooplankton and pelagic fish, enhancing its biological and economic importance (Rossi et al., 2013). During upwelling events, substantial cross-shelf exchange can take place (Brink, 1998). These events of enhanced primary productivity and offshore transport are the focus of this study.

$$UI = \frac{\tau}{f} \tag{2.1}$$

The 2010 summer upwelling season was unusually strong. Winds originated from the direction $0 \pm 45°$ (i.e. within 45° of north) for 82 % of the deployment. The mean wind speed was 8.2 m s^{-1} and the mean Upwelling Index (UI) was 950 ($\pm$ 40) m^3 km^{-1} s^{-1}. UI was first described by Bakun (1973). UI is the portion of Ekman transport perpendicular to the coastline, which is calculated as the alongshore wind stress τ divided by the Coriolis parameter f (Equation 2.1). A positive value of UI is indicative of upwelling favourable conditions. As UI is a representation of Emkan transport, its units are of cubic meters of water transported cross shelf per km of coastline. UI for the region for each year over the same yearday range averaged 550 ($\pm$ 190) m^3 km^{-1} s^{-1} (Puertos del Estado, 2019). In 2010, UI was two standard deviations above the mean (Figure 2.2). Similarly strong upwelling conditions occurred during 1981, 2002 and 2016. These unusually strong conditions resulted in a summer dominated by upwelling.

To observe this variability during the upwelling season at high spatial and temporal resolution, an autonomous ocean glider was deployed at the NWIM during summer 2010. The deployment is described in Section 2.5.1. Data processing and gridding are presented in Section 2.5.2. In Section 2.6 we present the results, in Section 2.7 we discuss the results and make recommendations for future observational campaigns on the NWIM. In Section 2.8 we summarise the key results.

2.5 Data collection and processing

2.5.1 Data collection

From 1 June to 5 August 2010, Seaglider SG510 Orca occupied an onshore-offshore section at 42.1 °N across the shelf and slope from 9.1 to 9.7 °W (Figure 2.1). Each passage through the section is referred to as a transect. Seagliders are small, buoyancy-powered vehicles that profile to 1000 m with a sawtooth dive pattern (Eriksen et al., 2001). The glider profiled over bathymetry of 150 to 2000 m. Individual dive cycle duration varied from 30 minutes on the shelf to 4 hours over the deep slope. During a dive the glider travels between 500 m and 4 km horizontally. Each dive cycle yielded two profiles, one when the glider was descending, one when it was ascending. The glider recorded measurements every 5 s above 200 m and every 10 s below 200 m. The glider has a typical vertical speed of 0.1 m s^{-1}, resulting in vertical sampling resolutions of approximately 0.5 m and 1.0 m respectively. The glider travelled zonally at 0.1-0.3 m s^{-1} relative

to the ground.

The glider was equipped with a Paine Corporation pressure sensor, an unpumped Seabird CT sail measuring temperature and conductivity, a WETLabs ECO Puck triplet sensor measuring chlophyll *a* flourescence, backscatter and colored dissolved organic matter, and an Aanderaa 4330F oxygen optode. Transects covered on average 45 km and took 2-6 days. Transect time increased towards the end of the deployment due to biofouling that increased drag on the glider. This is apparent in the increased time taken to complete transects later on in the mission (Figure 2.1d). The glider completed the section 17 times. Some transects were truncated, due to strong episodic equatorward currents on the inner shelf that prevented the glider from progressing, but all were greater than 36 km (Figure 2.1c). Due to strong equatorward currents, the glider deviated meridionally from its intended zonal track with a standard deviation of 2.8 km (Figure 2.1c). Considering these deviations to be small, we have projected all samples onto a zonal section. We compared the temperature-salinity characteristics of all transects (not shown). Transects all sample the same water masses, even those with large meridional deviations. Transects 2 and 6 have been chosen as typical examples of non-upwelling and upwelling conditions respectively. Transect 2 took place after a period of relaxation favourable conditions, whereas transect 6 was conducted at the peak of the first upwelling event (Figure 2.1).

The shelf break is defined as the 300 m isobath shown in Figure 2.1. Throughout the text, "shelf" refers to waters east of the shelf break, "slope" refers to waters west of the shelf break. Yeardays (YD) are used throughout, with January 1st 2010 as yearday 0. The first day of this deployment 1 was June 2010, yearday 151.

2.5.2 Data processing and gridding

The hydrodynamic flight model for the glider was tuned following the methods of Frajka-Williams et al. (2011). Dive average currents (DACs) were calculated from the difference between the glider's flight path calculated from GPS fixes at the beginning and end of each dive, and the glider's flight path from the flight model. This method consists of calculating the path that a glider takes through the water, using its buoyancy, pitch, roll and vertical speed calculated from pressure change over time. The difference between the expected surfacing location of the glider, and the observed surfacing location from GPS is attributed to advection of the glider while underwater. Assuming a constant vertical speed, this distance divided by the time that the glider was underwater is an estimate of the vertically averaged current. This dive average current is then used as the reference velocity

when calculating absolute velocities from velocity shear calculated by geostrophy, as calculated in Section 1.2.

The flight model regression is very sensitive to drag coefficients, which varied greatly over the glider deployment. Parasitic drag increased by over 200 % due to biofouling. To accommodate this, the glider flight model was calculated using batches of 30 dives, allowing the friction coefficients to vary over the 1050 dives analysed. The DACs were inspected for directional biases that can arise from a poorly calibrated compass, but no substantial differences were found. Thermal lag of the CT cell was corrected following Garau et al. (2011). These corrections were implemented with the UEA Seaglider Toolbox (Queste, 2014).

To remove tidal currents from the DAC time series, dives were separated into two subsets, onshore and offshore of the shelf break, following the method of Sheehan et al. (2018) who separated DACs into three spatial bins for tidal analysis. We used the shelf break, defined as the 300 m isobath, as the dividing line between these two bins. These two datasets, each comprising approximately one month of DAC observations, were treated as discontinuous time series and harmonic analysis was used to extract the M_2 and S_2 tidal constituents. The combined M_2 + S_2 tidal current had a maximum amplitude of 0.5 cm s^{-1} over the slope and 2.0 cm s^{-1} on the shelf. The tidal constituents were validated against the TPXO tide model (Egbert and Erofeeva, 2002). The choice of two domains was made as the M_2 tidal component in the region varies substantially between shelf and slope (Quaresma and Pichon, 2013). Each bin also satisfies the Rayleigh criterion for distinguishing between the M_2 and S_2 tides with time series of greater than 14.8 days (Sheehan et al., 2018). For the purposes of this paper, DAC is assumed to be an approximate barotropic current where the glider sampled the full water column and an approximate vertical average current in the upper 1000 m, where the bathymetry exceeded the glider's profiling depth. The M_2 and S_2 tidal constituents were subtracted from the DACs before using the DACs to reference geostrophic shear. DACs are typically considered accurate to within 1 cm s^{-1} (Eriksen et al., 2001; Merckelbach et al., 2008). Acknowledging that this detiding will not remove all tidal constituents from the DACs, we have incorporated a 2 cm s^{-1} uncertainty in our calculations of geostrophic currents. This uncertainty in geostrophic velocity is used for uncertainty estimates in alongshore transports.

The WETlabs ECO Puck measures fluorescence as a proxy for chlorophyll *a* concentration (henceforth chlorophyll). The ECO Puck excites chlorophyll by emitting at 470 nm and records florescence at 695 nm. Chlorophyll fluoresces at a range of wavelengths centred on 682 nm (Maxwell and Johnson, 2000). The chlorophyll florescence data are calculated using a linear equation $y = m(x - c)$,

where y is chlorophyll concentration (mg m^{-3}) and x is the sensor output (counts). We used the manufacturer supplied gradient $m = 0.121$ and a dark counts level $c = 48$, 8 % lower than the manufacturer supplied value, such that the sensor registered 0 chlorophyll at depths greater than 150 m. An in-water calibration was carried out with co-located CTD casts on 1 June (YD 151), 29 June (YD 179) and 29 July (YD 210) (Brown, 2013). Chlorophyll values were corrected for the effects of non-photochemical quenching following the methodology of Thomalla et al. (2018). As the principal interest of this study is the cross shelf and temporal variability of chlorophyll, we are not aiming for an approximation of chlorophyll concentration better than a factor of two.

The Aanderaa optode is a low power foil type sensor as described by Alkire et al. (2012). Dissolved oxygen concentration was calculated using manufacturer calibration constants. The oxygen concentration was then corrected for temporal drift by applying a linear correction in time such that oxygen concentrations at 850-950 m depth remained constant in time. Winkler bottle samples were used to calibrate the ship CTD O_2 sensor on 29 July (YD 210), 15 September (YD 257) and 29 September (YD 271). This calibration was applied to CTD casts on 1 June (YD 151), 29 June (YD 179) and 29 July (YD 210) (Brown, 2013).

Temperature and salinity data for each transect were interpolated with an Objective Analysis Barnes function (Barnes, 1994) onto a grid with spacing 1 km horizontal by 1 m vertical, using a horizontal smoothing distance of 8 km and vertical smoothing of 8 m. This horizontal distance was chosen as it is the first internal Rossby radius of deformation over the shelf slope at the middle of the section. These gridded values were then used to calculate the potential density, absolute salinity and conservative temperature using the Gibbs Seawater toolbox (IOC and IAPSO, 2010). We found the geostrophic velocity field calculated from these interpolated data to be largely insensitive to smoothing distances from 0.5 to 15 km. Dissolved oxygen concentration and chlorophyll concentration were gridded using the same methodology.

Hovmöller plots were constructed by a linear interpolation of samples taken within $\pm$ 2.5 m vertically of the plot level. These samples were interpolated to a grid spaced 1 km horizontally and 8 hours in time, using a smoothing distance of 8 km and smoothing time of 3 days. This smoothing time was chosen as it is the typical response time of the NWIM to changes between upwelling and downwelling states (McClain et al., 1986).

Geostrophic currents were calculated from thermal wind, using the detided glider DACs as a reference velocity. The geostrophic approximation is commonly used with glider datasets in upwelling regions (Todd et al., 2011a; Pietri et al., 2013), with estimated uncertainties of 1 -2 cm s^{-1}. Geostrophic currents calculated with

this method compare well with ADCP data (Pietri et al., 2013). Bottom velocities were nearest neighbour extrapolated to fill gaps between glider sampling and bathymetry over the shelf and slope, with no extrapolation past the maximum measurement depth (1000 m). A Monte Carlo method was used to estimate uncertainty in the alongshore transports by applying random Gaussian noise with a standard deviation of 2 cm s^{-1} to the DACs, the largest source of error in estimation of geostrophic currents from glider data. Ageostrophic velocities are included in the dive average current estimated from the glider flight model. We are not able to estimate the uncertainty introduced by the relatively slow transects of the glider.

UI for the Rías Baixas is calculated by the Puertos del Estado at 6 hour intervals using the FNMOC model (Puertos del Estado, 2019). Satellite sea surface temperature (SST) are taken from CMEMS Atlantic European North West Shelf Seas - Reprocessed SST Analysis - ODYSSEA from AVHRR Pathfinder v5.3, daily product 0.04 degrees resolution. Chl a satellite data are from MODIS (Hu et al., 2012), daily product 0.0104 degree resolution. Bathymetry from EMODnet is used in this study (EMODnet Bathymetry Consortium, 2018).

We use units of conservative temperature and absolute salinity following IOC and IAPSO (2010). All densities are potential density anomalies σ_θ = potential density - 1000 with units of kg m^{-3}. Oxygen supersaturation, $\Delta(O_2)$ is calculated as

$$\Delta(O_2) = \frac{c(O_2)}{c_{eq}(O_2}) - 1, \tag{2.2}$$

where $c(O_2)$ is the measured O_2 concentration and $c_{eq}(O_2)$ is the O_2 concentration at an absolute pressure of 101325 Pa, calculated with potential temperature and salinity (Garcia and Gordon, 1992, 1993). A positive value represents oxygen supersaturation, a negative one represents oxygen undersaturation.

2.6 Results

2.6.1 Initial Conditions

Prior to upwelling (Figure 2.1d transects 1, and 2), conditions across the section were typical of relaxation. Isopycnals were near horizontal, with a layer of warm > 18 °C, low salinity < 35.9 g kg^{-1}, low density $\sigma_\theta < 26.0$ kg m^{-3} water occupying the upper 20 m over the shelf and slope (Figures 2.3c, 2.4a and 2.4b). Vertical chlorophyll and $\Delta(O_2)$ distributions were similar across the section, with a subsurface chlorophyll maximum of 2.1 mg m^{-3} at 38 m and a $\Delta(O_2)$ maximum of 12 % from the surface to 25 m (Figures 2.5a and 2.5b). Water above the $\sigma_\theta = 26.9$ kg m^{-3} isopycnal was supersaturated in oxygen, water

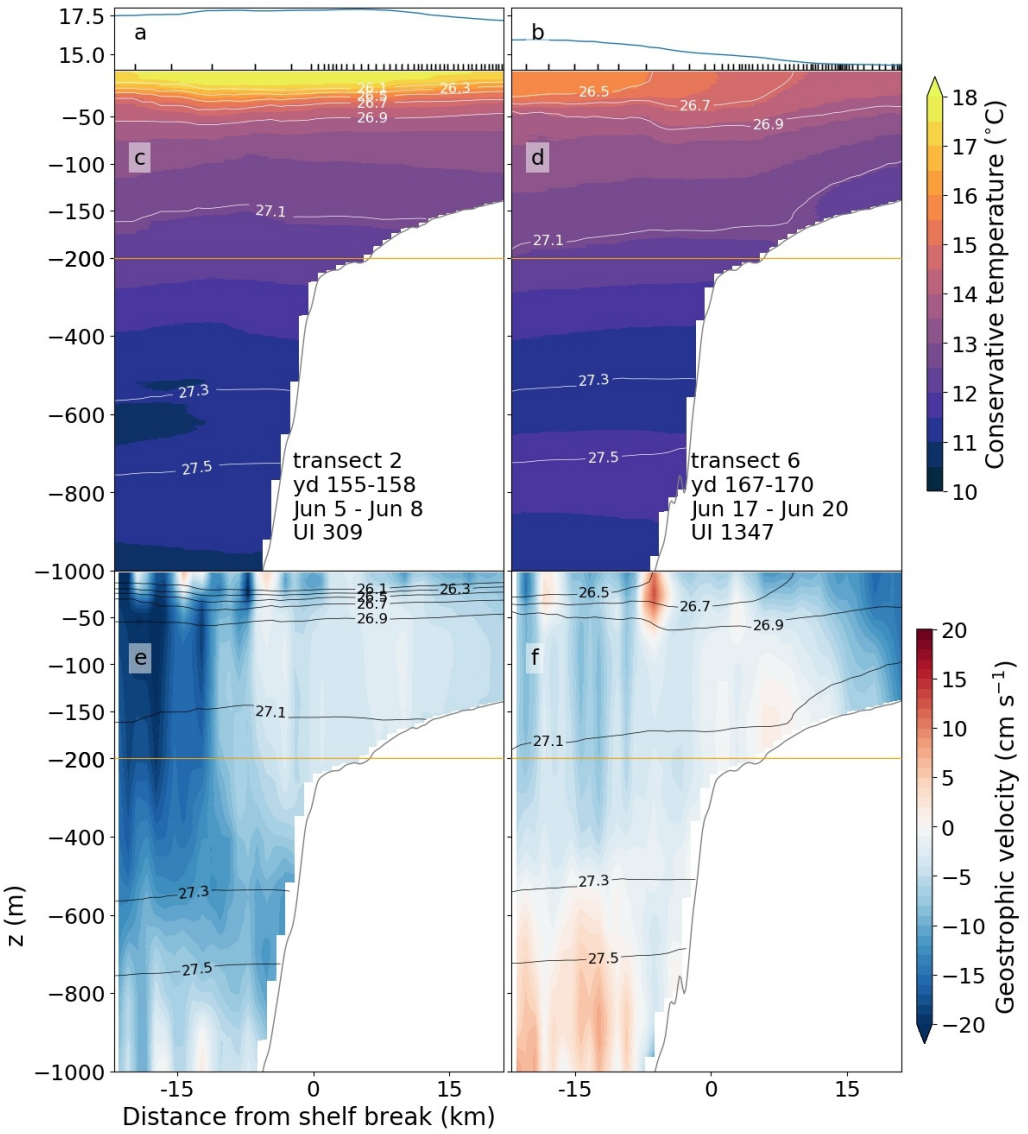

Figure 2.3: Conservative temperature (a-d) and meridional velocity (e & f). (a & b) Conservative temperature averaged over the uppermost 5 m, black ticks mark the surfacing of the glider during the transect for that column. (e & f) Meridional geostrophic velocity, negative velocity is equatorward. Density plotted with black lines. (a,c,e) Transect 2. (b,d,f) Transect 6. Density isopycnals mark the approximate boundaries between $ENACW_{st}$ and $ENACW_{sp}$ (σ_θ = 27.1 kg m^{-3}) and between $ENACW_{sp}$ and MEDW (σ_θ = 27.3 kg m^{-3}). Note that the vertical scale changes at z = -200 m.

below this isopycnal was undersaturated. The greatest chlorophyll concentrations and greatest $\Delta(O_2)$ were at the eastern end of the section, over the shelf. Below the pycnocline $\Delta(O_2)$ was greater over the shelf break and lower over the inner shelf, particularly near the sea floor where $\Delta(O_2)$ of less than -16 % was observed (Figure 2.5b).

During transects 3 and 4 (8-14 June), increasing wind speeds mixed the surface

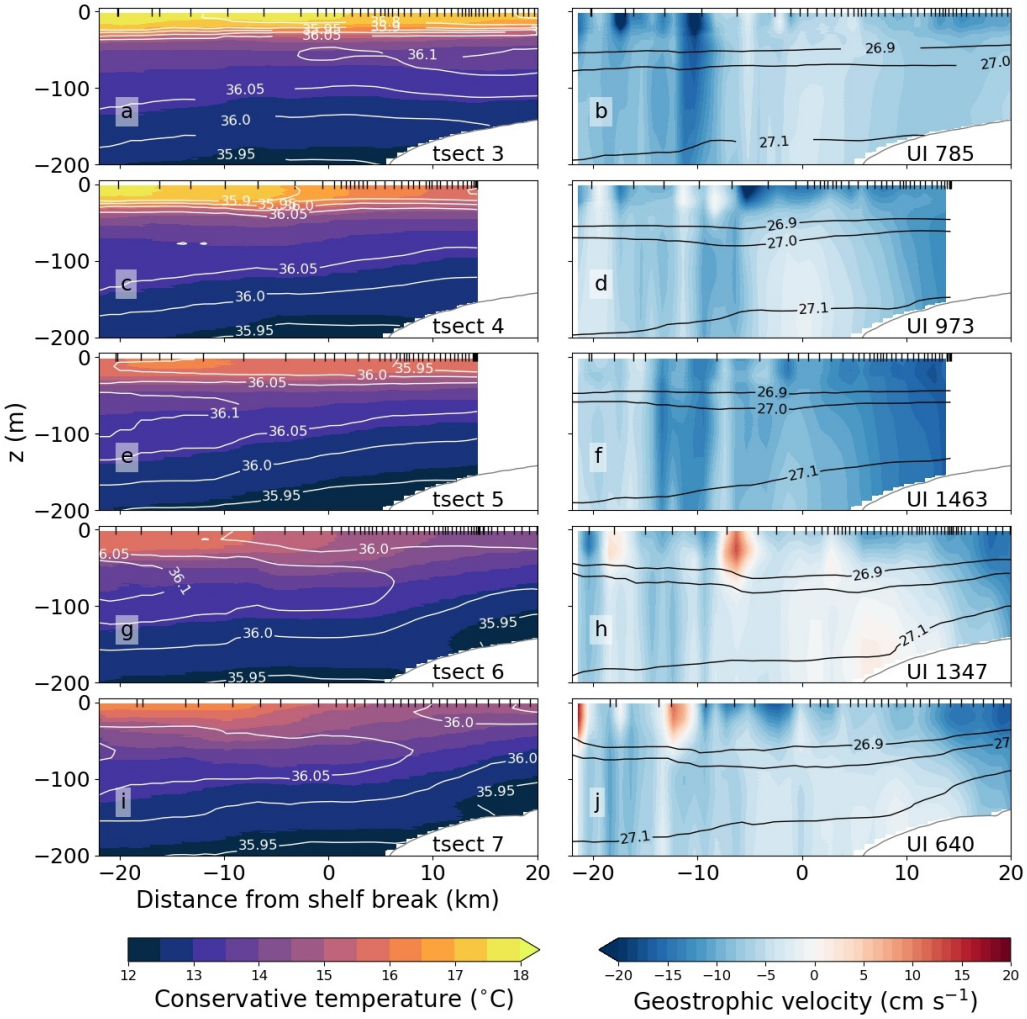

Figure 2.4: Evolution of conservative temperature (a,c,e,g,i) and meridional geostrophic velocity (b,d,f,h,j) during the first upwelling event, transects 3-7. (a,c,e,g,i) Contours are absolute salinity (g kg^{-1}). (b,d,f,h,j) Contours are density. UI on each figure in m^3 s^{-1} km^{-1} and is the value at the time the glider crossed the shelf break. Black ticks at the top of figures mark surfacings of the glider.

waters, increasing the mixed layer depth from 5 to 15 m (Figure 2.4). Chlorophyll in the upper 30 m increased by 0.8-1.6 mg m^{-3} and the subsurface chlorophyll maximum shoaled to 27 m (Figure 2.5c). After transect 4, the subsurface $\Delta(O_2)$ maximum was not observed. Wind speed increased to 13 m s^{-1} during transect 4.

2.6.2 First upwelling event

The first upwelling event began on 14 June (YD 164, Figure 2.6). This occurred during transects 4-7 of the deployment (Figures 2.4 and 2.5). The onset of upwelling was first apparent in the increase in the equatorward current over the

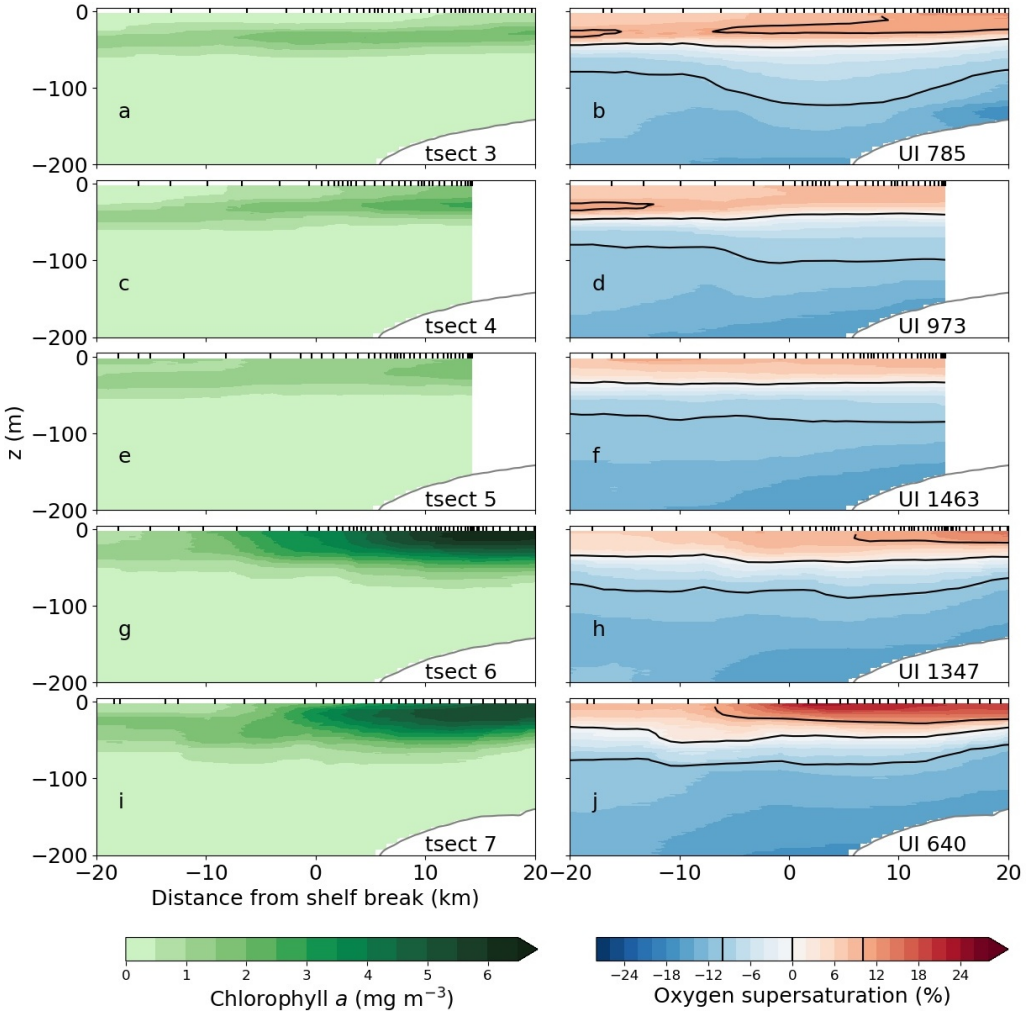

Figure 2.5: Evolution of chlorophyll a concentration (a,c,e,g,i) and oxygen supersaturation ($\Delta(O_2)$) (b,d,f,h,j). (b,d,f,h,j) -10, 0 and 10 % $\Delta(O_2)$ contours in black. Annotations as in Figure 2.4.

outer shelf from 3 to 8 cm s^{-1} during transect 4 (14 June, Figure 2.6a). The warm, low density surface waters were displaced 30 km offshore in 4 days (Figures 2.4a and 2.4c). The front between the warm surface water and cooler upwelled water moved offshore at approximately 0.1 m s^{-1}, consistent with previous observations of frontal translation during upwelling (Rossi et al., 2013). This reflects the large volume of water upwelled displacing the warmer, less dense waters offshore. This translation. speed was inferred from the observed horizontal displacement of isopycnals between glider transects. Strong equatorward currents at this time prevented the glider reaching its easter waypoint during transect 4 (Figure 2.6). Because of this, we have no glider observations for the shelf more than 14 km inshore of the shelf break for 10 days. This period coincided with the wind speed peak of the first upwelling event. Satellite data show surface cooling and elevated chlorophyll a

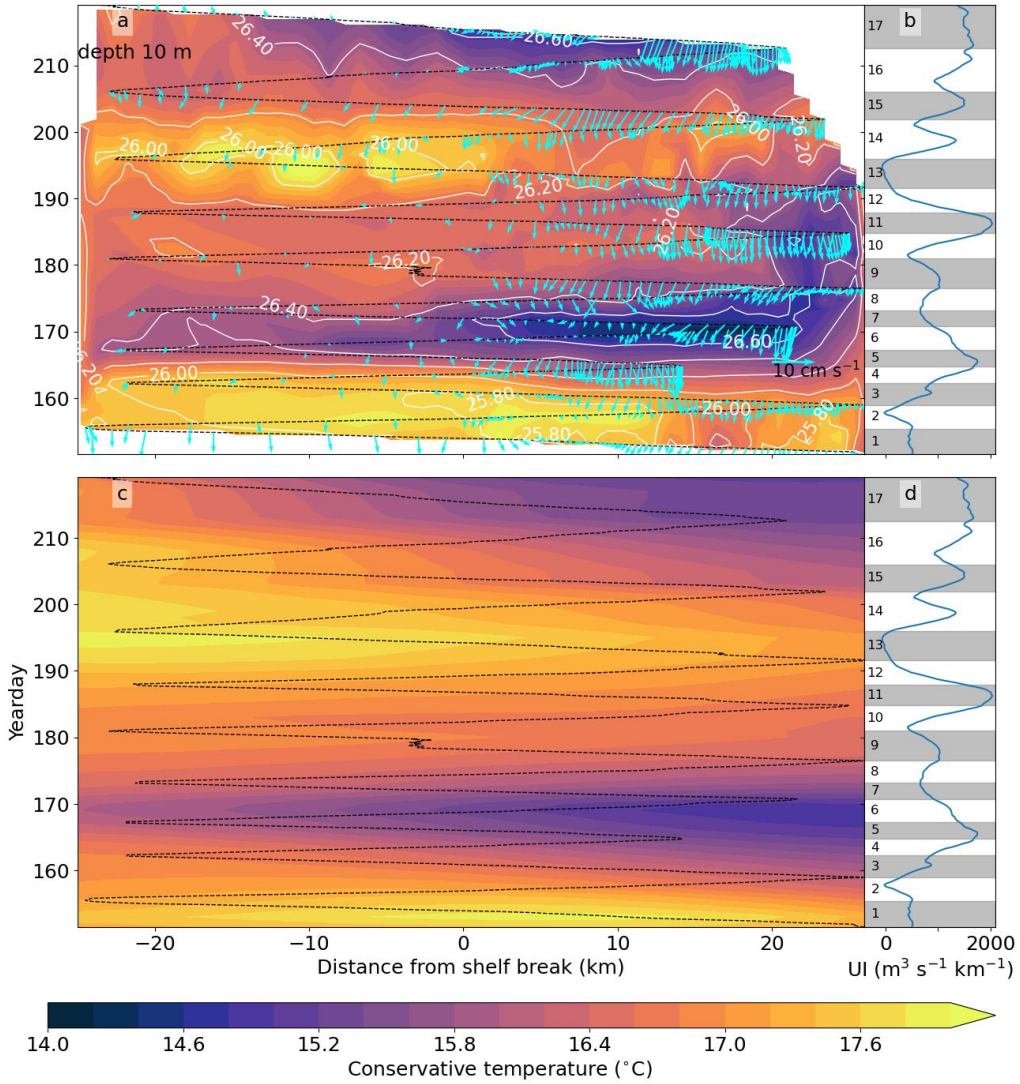

Figure 2.6: (a) Conservative temperature at 10 m depth. Black dashed line demarcates glider track in time. Black lines are potential density anomalies in kg m^{-3}. Cyan vectors are detided dive average currents. (c) Satellite observed SST with glider track overlaid. (b & d) Upwelling Index (UI) with glider transects shaded and numbered as in Figure 2.1.

concentrations during this time period (Figures 2.6c and 2.7c).

After the offshore advection of the warm low density water, near surface waters over the shelf became cooler and more saline (Figures 2.4g and 2.4i). Temperature near the surface decreased by as much as 3.0 °C at the eastern end of the section (Figure 2.6a). An across slope temperature gradient of 0.1 °C km^{-1} in the upper 20 m was observed (Figure 2.3b) typical of a front between warm surface and cool upwelled waters (Ferreira Cordeiro, 2018). Over the shelf, the $\sigma_\theta = 27.1$ kg m^{-3} isopycnal shoaled from 180 m to shallower than 100 m (Figures 2.4b and 2.4h). A core of cool, saline water with temperature-salinity characteristics between those

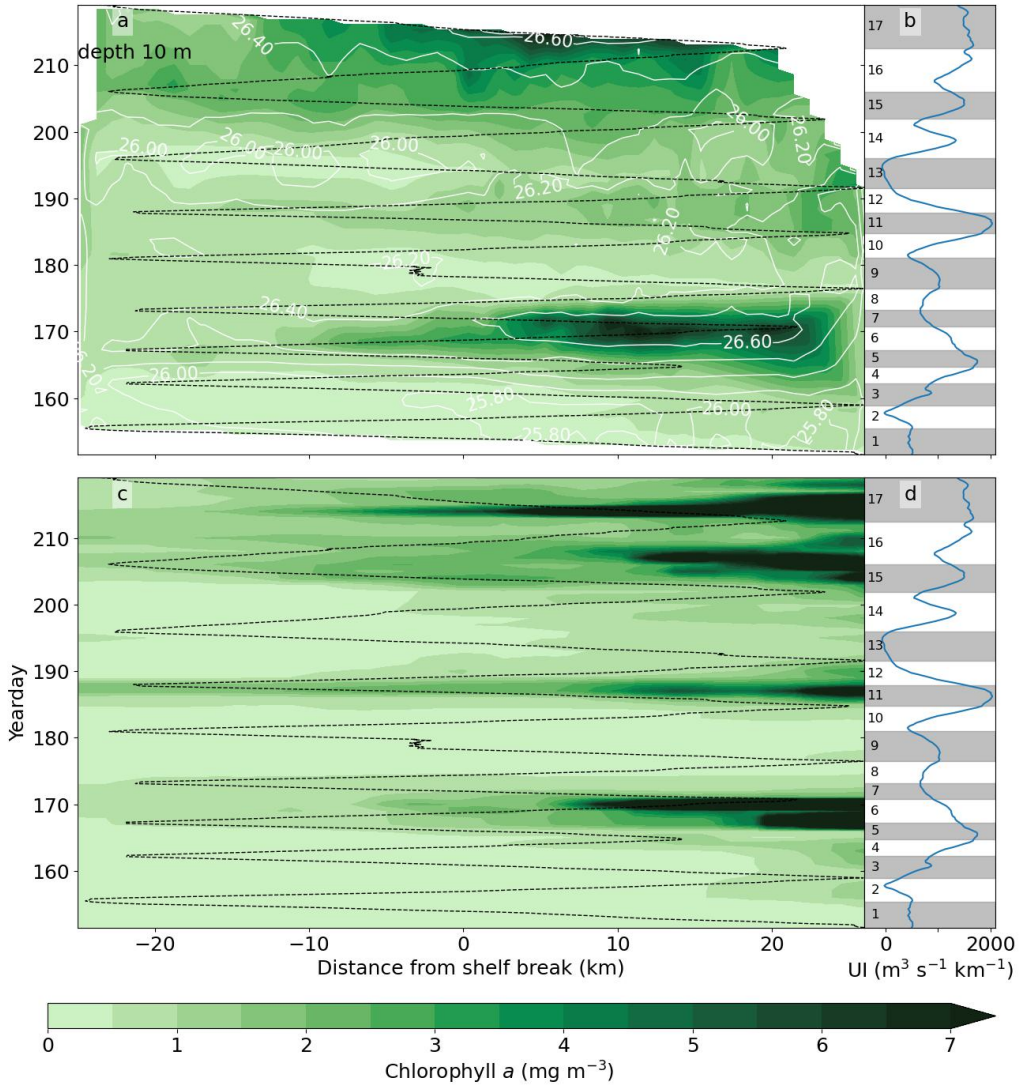

Figure 2.7: As Figure 2.6 for Chlorophyll a concentration.

of ENACW$_{st}$ and ENACW$_{sp}$ was upwelled onto the shelf during transects 6 and 7 (17-23 June, Figures 2.4g and 2.4i). The presence of this water on the shelf suggests upwelling of waters from depths of greater than 190 m, as has been observed previously (Huthnance et al., 2002). The change from near horizontal isopycnals pre-upwelling to isopycnal slopes of 4 m km^{-1} across the shelf break is pronounced (Figures 2.3c and 2.3d). The $\sigma_\theta = 27.0$ kg m^{-3} isopycnal shoaled by 20 m over the shelf, similar to that observed during summer 2009 by Ferreira Cordeiro et al. (2018). During the upwelling event, isopycnals outcropped over the shelf break (Figure 2.3f).

Prior to the first upwelling event, average chlorophyll concentrations were similar on the shelf and over the slope, though concentrations over the slope exhibited more variability (Figure 2.8a). Chlorophyll concentrations increased after the development of full upwelling, coincident with the decrease in near

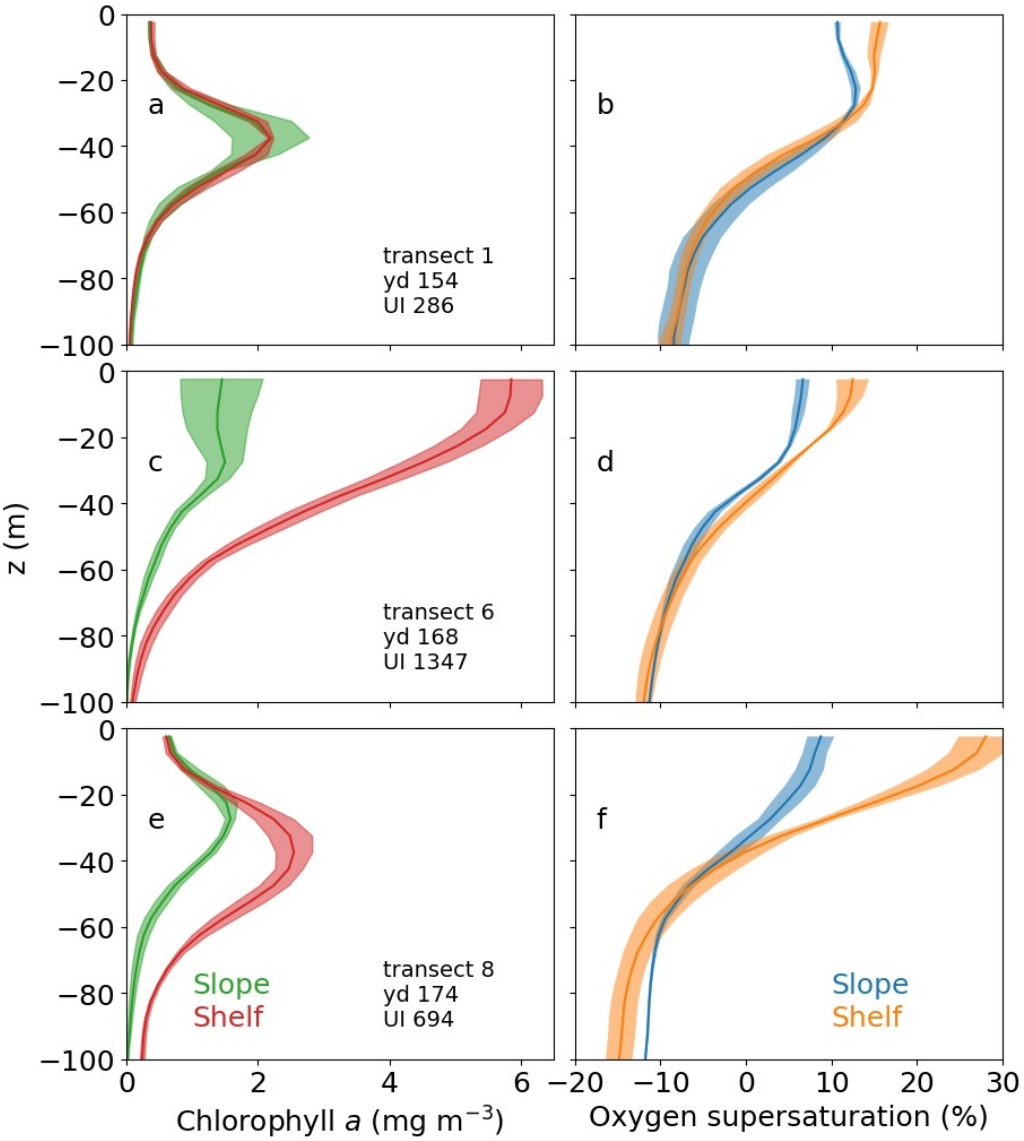

Figure 2.8: Mean vertical profiles of chlorophyll concentration (a,c,e) and $\Delta(O_2)$ (b,d,e) before and during the first upwelling event. The green and blue lines are the average of the water column over the slope, more than 5 km west of the shelf break. The red and orange lines are the average of the water column over the shelf, more than 5 km east of the shelf break. Uncertainty of 1 standard deviation is shaded around each profile. Transect number, yearday of the transect and UI during the transect are shown on each panel.

surface temperature (Figure 2.7). Higher chlorophyll concentrations were observed over the shelf than the slope for the entirety of the upper 100 m during transect 6 (Figure 2.8c). The subsurface chlorophyll maximum over the shelf shoaled to 12 m and near surface concentrations surpassed 6.0 mg m^{-3} over the inner shelf more than 10 km inshore of the shelf break during transects 6-7 (Figure 2.7). The chlorophyll maximum changed in character from subsurface to surface. $\Delta(O_2)$ followed the same pattern as chlorophyll but

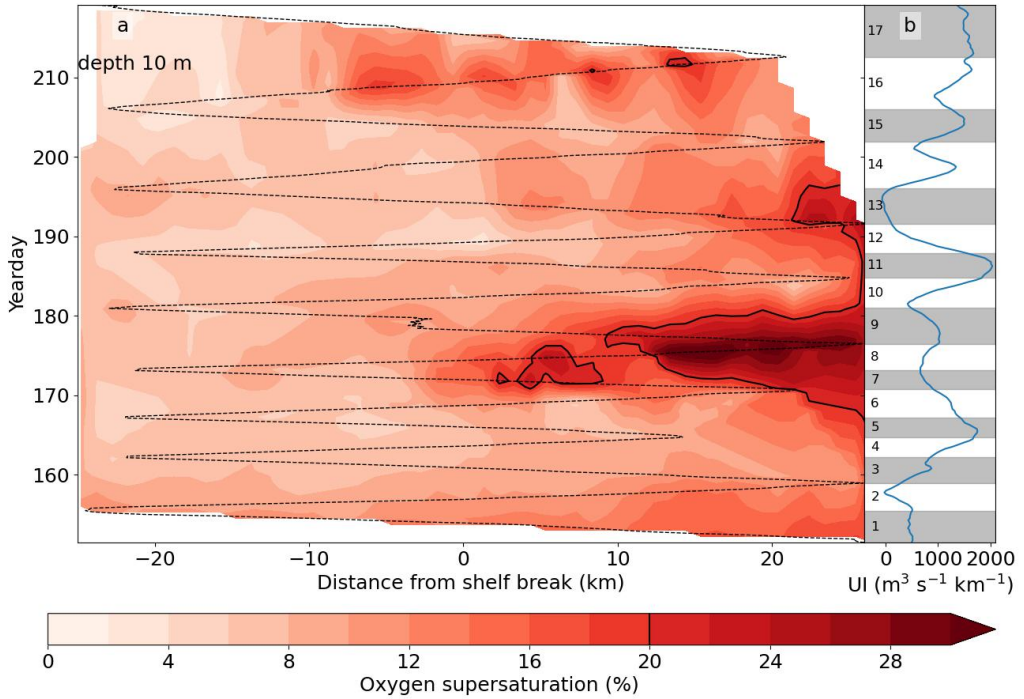

Figure 2.9: As Figure 2.6a and 2.6b for $\Delta(O_2)$. 20 % $\Delta(O_2)$ contour in solid black.

peaked during transects 8-9, 6 days later (Figures 2.7 and 2.9). $\Delta(O_2)$ increased most in the near surface over the shelf to greater than 28 %. during transect 8, the greatest supersaturation observed during the deployment (Figures 2.8f and 2.9). Chlorophyll and $\Delta(O_2)$ over the slope increased only slightly during the same time period (Figures 2.8c-2.8f).

After peaking during transect 7, maximum chlorophyll concentration over the shelf decreased to 2.3 mg m^{-3} and the subsurface chlorophyll maximum descended to 43 m during transects 8 and 9. $\Delta(O_2)$ over the shelf also decreased, reaching a minimum during transects 10 and 11, 8 days later than the minimum of chlorophyll in the near surface (Figures 2.7 and 2.9).

A brief period of strong equatorward wind around YD 188 (8 July, transects 10-11) increased equatorward current speed on the shelf (Figure 2.6a). However, this event was short lived and caused only a modest decrease in temperature on shelf at the eastern end of the transect (Figure 2.6a). Small increases in chlorophyll (0.5 mg m^{-3}) and $\Delta(O_2)$ (10 %) in the near surface were observed during the following transects 12-13 (Figures 2.7 and 2.9). The effects of this period of increased winds were mainly limited to the inner shelf, more than 10 km east of the shelf break (Figures 2.6, 2.7 and 2.9). The lack of response to this period of increased equatorward wind could be due to its short duration. The response time of the margin is around 3 days (McClain et al., 1986). This event may have

been too short to trigger a fully developed upwelling signal.

2.6.3 Partial relaxation and second upwelling event

A relaxation of the southward winds during YDs 191-194 (11-14 July, transect 13) brought surface warming of 2.0 °C over the slope and a decrease in the strength of equatorward flows (Figure 2.6). This relaxation was not sufficient to reverse the equatorward flow on the shelf, as has been observed during periods of northward winds in other years. (Ferreira Cordeiro et al., 2018) observed poleward flow over the inner shelf during periods of relaxation. This could also be due to observational limitations, as the glider was unable to reach the inner shelf where water depths are less than 50 m 2.1). Chlorophyll concentrations over the slope and shelf decreased (Figure 2.7).

During the final three transects of the deployment (21 July-8 August) a second upwelling event developed. This second event followed a similar pattern to the first with increased equatorward currents over the shelf and upwelling of cold, dense water decreasing near surface temperature by 2.0 °C (Figure 2.6). During the final transect, chlorophyll concentrations observed over the shelf increased to similar levels as observed during the first upwelling event (Figure 2.7). The highest chlorophyll concentration in the near surface were observed on the outer shelf at 5 km east of the shelf break (Figure 2.7). Assuming a similar lag between chlorophyll and $\Delta(O_2)$ in the near surface as observed during the first upwelling event, it is likely that $\Delta(O_2)$ increased past the end of the deployment. The second upwelling was not as strong as the first either in the decrease in surface water temperature (Figure 2.6) or in the increase in chlorophyll (Figure 2.7). This is despite the upwelling index being as great as during the first upwelling event, and remaining above 500 $m^3\ km^{-1}\ s^{-1}$ for longer. The upwelling index cannot explain all of the variability of surface conditions and other factors, such as advection by the strong and temporally varying meridional currents, may play a role.

2.6.4 Geostrophic currents and transports

As expected for the NWIM, along slope flows dominated, as shown by the DACs (Figure 2.6). During the deployment, the wind was primarily perpendicular to the glider transect, so Ekman flow contributed little to along slope velocities. After detiding and gridding (Section 2.5.2), we assume the velocity structure we observe to be dominated by geostrophic flow. The DACs include ageostrophic contributions from wind stress. The DACs estimated from the glider flight model show very little cross shelf net velocity. There is clear evidence for Ekman transport in the near surface translating the front offshore (Figure 2.4), this offshore advection in the near surface must be compensated

by water flowing onshore at depth to replace it. Consequently, the dive average currents have a zonal component of near 0.

The alongshore flow averaged horizontally and vertically over the entire section, and over its shelf and slope subsections, was equatorward in every transect, though poleward transport as part of eddies was present (Figure 2.6a). Average equatorward transport was 0.17 (± 0.07) Sv over the shelf and 0.83 (± 0.6) Sv over the slope. Averaged over the 17 transects (not shown) surface intensification of southward flow over the shelf is apparent, particularly at the near-shore end of the section, with a maximum flow speed of 15 cm s^{-1} (Figures 2.4 b,d,f,h,j). A minimum in southward flow speed of 2 cm s^{-1} was observed near the sea floor at the shelf break (Figure 2.3). Over the slope, equatorward flow is strongest at 50-150 m, the typical depth of $ENACW_{st}$. Equatorward flow weakens with depth, reaching a minimum flow speed below 700 m, at the depth of MEDW (Figure 2.3e and 2.3f).

During the 2 months of observation there was substantial variability in the strength of the equatorward transport. During upwelling, current speed increased over the shelf and the flow became more surface intensified (Figures 2.4d, 2.4f and 2.4h). Transport on the shelf increased from 0.13 (± 0.04) Sv to 0.18 (± 0.08) Sv during the two upwelling events. This flow is strongest at the near-shore end of the section (Figure 2.3f). The flow can be reasonably expected to extend further inshore, as has been observed in previous upwelling seasons on the NWIM (Rossi et al., 2013; Ferreira Cordeiro et al., 2018) and therefore our transport is likely an underestimate.

Over the slope, a broad equatorward flow dominated in the upper 500 m (Figure 2.3e). This flow was observed to weaken at depth, with a sporadic poleward flow below 500 m (Figure 2.3f). No relation was found between the UI and meridional transport over the slope. Small eddies were observed in the near surface throughout the deployment (Figures 2.4e and 2.4f). These moved offshore (westward) during the first upwelling event at 2 cm s^{-1}, similar to the upwelling event observed by Rossi et al. (2013).

2.7 Discussion

During June and July of 2010, the shelf and slope near Cape Silleiro experienced summer upwelling similar in character to that of previous years, but stronger (Relvas et al., 2007). In contrast to previous years, which featured cycles of upwelling and relaxation (Rossi et al., 2013; Ferreira Cordeiro et al., 2018), upwelling conditions dominated the observational period. A cross shore temperature gradient between cool upwelled water over the shelf and warmer

surface waters offshore was present during the majority of the deployment (Figure 2.6). Isopycnal outcropping was frequently observed over the shelf and upper slope (Figure 2.4).

$$\Delta T = \frac{\Delta T Q_{LH}}{d c_p \rho} \tag{2.3}$$

During the first upwelling event, mean temperature of the upper 20 m of the water column over the shelf decreased by 2.5 °C in less than 8 days (Figure 2.6). Latent heat loss to the atmosphere (Q_{LH}) averaged 120 W m^{-2} during this period of increased wind speed (data from ERA5 Global Reanalysis (Copernicus Climate Change Service (C3S), 2017)). Equation 2.3 shows how the temperature change from latent heat loss to the atmosphere (ΔT) during time period Δt is calculated from latent heat flux Q_{LH} thickness of mixed layer d (20 m), density of seawater ρ (1018 $kg\ m^{-3}$), and the specific heat capacity of water c_p (4184 $J\ kg^{-1}\ C^{-1}$). Over 8 days this latent heat loss to the atmosphere would cool the uppermost 20 m of the water column by 1.0°C. Incorporating sensible heat loss and incoming solar radiation, the net heat flux over the same period was an order of magnitude smaller. The cooling can only be the result of upwelled deeper water or horizontal advection of a temperature gradient. Previous studies have established upwelling as the mechanism by which cool, nutrient rich water reaches the near surface over the shelf (Relvas et al., 2007; Ferreira Cordeiro et al., 2018). Heat fluxes were calculated with an Eulerian reference frame, not Lagrangian. However, satellite SST data show that cool water features centred on the capes, including Cape Silleiro, expand and contract zonally but do not migrate meridionally (not shown). This is strongly indicative of upwelling, not advection. Surface cooling would not explain the observed changes in salinity, chlorophyll, $\Delta(O_2)$ and near surface currents which can only be the result of upwelling.

Upwelling raised the subsurface chlorophyll maximum and increased chlorophyll concentration throughout the mixed layer over the shelf and shelf break (Figure 2.8). The upwelled ENACW is relatively low in oxygen but the high nutrient concentration promotes phytoplankton growth (Rossi et al., 2013). We take elevated chlorophyll (Figure 2.7) and optical backscatter (not shown) to be indicators of elevated primary productivity and biomass, whilst acknowledging that processes such as photoacclimation or changes in pigment packaging and ecosystem composition can influence chlorophyll without necessarily increasing primary productivity and biomass (Cetinić et al., 2015). Increased primary productivity would account for the observed increase of $\Delta(O_2)$ (Figure 2.8). $\Delta(O_2)$ peaked after chlorophyll (and optical backscatter at 650 nm, not shown)

over the shelf, with a delay of approximately 6 days. Oxygen in the mixed layer will also be affected by air-sea gas exchange, which will cause a further lag in the peak response of $c(O_2)$ with respect to the chlorophyll concentration. This measurable time delay is therefore an important result. Chlorophyll concentration provides a convoluted signal of productivity and biomass, whereas oxygen concentration is an integrated signal of production, giving cumulative net community production. One would therefore expect the integrated signal of oxygen to reach its maximum after the peak in chlorophyll, as is shown in our glider observations.

During crossings 12 and 13, the local maxima of chlorophyll and $\Delta(O_2)$ coincided, as observed by the glider, (Figure 2.7 and Figure 2.9). This could indicate that another mechanism affects the concentration of oxygen in near surface waters. This could be a physical effect such as bubble injection, or a different ecosystem response to that which contributed to the delay between maxima in chlorophyll and $\Delta(O_2)$ observed after the first upwelling event. The absence of observed lag could also be a result of the relatively long transect sampling interval; the time between between crossings 12 and 14 over the inner shelf was 10 days. As is apparent in Figure 2.7c, chlorophyll over the inner shelf can increase and decrease in as little as 3 days. Taking satellite data into account, there is a short spike in chlorophyll around yd 186-188 when the glider is off the shelf (Figure 2.7c). This spike precedes the oxygen maximum observed by the glider around yd 192. This pattern of a short chlorophyll peak preceding a broader peak of $\Delta(O_2)$ as observed during the first upwelling event.

During the first upwelling the chlorophyll maximum and near surface temperature minimum were observed at the eastern (inshore) end of the section. During the second upwelling event, the chlorophyll maximum and near surface temperature minimum were observed 5 km east of the shelf break by the glider. The observations of minimum near surface temperature and maximum chlorophyll near the shelf break during the second upwelling event may be due to observational limitations. During the second upwelling event the glider was travelling slowly due to biofouling. The glider reached the shelf break more than a day after its final sampling of the inner shelf. Satellite SST and chlorophyll data support this interpretation (Figures 2.6c and 2.7c). The bloom initiating with the second upwelling event spread further offshore than the first bloom (Figures 2.7a and Figures 2.7c). Westward DACs over the outer shelf and shelf break may have contributed to this offshore spreading of chlorophyll (Figure 2.6a).

In deeper water (> 50 m) over the shelf, $\Delta(O_2)$ decreased during and after upwelling events (Figure 2.8). A potential cause is the advection of low oxygen

$ENACW_{sp}$ onto the shelf. The upwelling of $ENACW_{sp}$ is visible in the temperature and density transects (Figure 2.3) in the shoaling of the $\sigma_\theta = 27.1$ kg m^{-3} isopycnal over the inner shelf. Biological activity also contributes to low oxygen values in deeper water (Rossi et al., 2013). During upwelling, nutrients depleted by near surface phytoplankton are replenished at depth by microbial remineralisation, consuming oxygen (Álvarez-Salgado et al., 1997; Rossi et al., 2013). Our observations of decreased $\Delta(O_2)$ below 50 m over the shelf agree with observations of near-bottom low-oxygen layers by Rossi et al. (2013).

The persistence of equatorward flow over the shelf throughout the deployment is atypical for the NWIM. Prior studies of the summer upwelling season have observed a reversion to poleward flow over the shelf during relaxation of equatorward winds (Peliz et al., 2002; Rossi et al., 2013; Ferreira Cordeiro et al., 2018). The absence of poleward flow over the shelf in our observations may be due to the time taken for the glider to return to the shelf. After the relaxation of the southward winds during YDs 191-194 (11-14 July), the glider was not present again over the shelf until YD 199 (19 July Figure 2.6). Ferreira Cordeiro et al. (2018) noted poleward flows from a relaxation period of only 5 days of weak winds. The shelf could have experienced poleward flow during the 5 days that the glider was off the shelf. Alternatively, the dominance of upwelling favourable winds in summer 2010 may explain this absence of observed poleward flow (Figure 2.2). No downwelling events were observed during the deployment.

Geostrophic flows matched the typical upwelling season flow regime of NWIM, with a near-shore surface intensified upwelling jet and equatorward flow over the shelf break and upper slope (e.g. the schematic shown by Ferreira Cordeiro et al. (2018)). Our observed equatorward transport over the shelf 0.17 ($\pm$ 0.07) Sv is greater than the seasonal transport of 0.09 Sv for June and July from the numerical modelling study of Teles-Machado et al. (2015). This is expected as the 0.09 Sv is based on a climatology of the years 1989-2008, which all had lower median values of UI than 2010 (Figure 2.2). Our observations of poleward flow near the seafloor over the shelf during upwelling (Figure 2.3f) are in agreement with previous studies observing a poleward countercurrent during upwelling at this location (Ferreira Cordeiro et al., 2018; Teles-Machado et al., 2015).

Offshore of the shelfbreak, a strong equatorward flow persisted throughout the deployment. We do not observe the poleward flow of the Iberian Poleward Current seen in models (Teles-Machado et al., 2015) and observations (Ferreira Cordeiro et al., 2018; Torres and Barton, 2007). This could be because the glider does not sample far enough offshore, turning around at 9.7 °W over

bathymetry of 2000 m, midway down the slope (Figure 2.1). An observational campaign in June and July of 2009 only observed the poleward flow west of 9.8 °W (Ferreira Cordeiro et al., 2018). Earlier observational studies have shown a similar pattern of poleward flows in the upper 200 m west of 9.8 °W during the summer months (Torres and Barton, 2007). The observed pattern of equatorward flow dominance over the shelf and upper slope would be expected during upwelling conditions, with the upwelling jet keeping the IPC offshore as has been suggested by Nolasco et al. (2013).

The slow speed of the glider resulted in considerable time lapse between transects (6 days on average). Due to this, the glider did not observe some events apparent in the satellite chlorophyll data such as the increases in near surface chlorophyll concentration over the shelf YDs 188-190 and 205-208. The time gap between observations of the shelf limited our ability to constrain the timing of some events, such as the lag between the chlorophyll and $\Delta(O_2)$ maxima (Figures 2.7a and 2.9a). The strong currents over the shelf also prevented the glider from reaching its eastern waypoint during the development of the first upwelling event. The glider's short section limited our observations of alongshore currents over the deep slope and of upwelling features inshore of the 160 m isobath. Future glider deployments in the region will need to consider the trade off between section length and the frequency of observations at either end of the section. Alternatively, multiple gliders could be deployed concurrently.

2.8 Summary

An autonomous ocean glider was used to observe the 2010 summer upwelling season over the NWIM. Upwelling of cold ENACW from below 190 m contributed to an increase of near surface chlorophyll concentrations from less than 1 mg m^{-3} to greater than 7 mg m^{-3}. The increase in primary production contributed to a near surface increase of $\Delta(O_2)$ of 16 %, 6 days after the chlorophyll maximum. Decreasing $\Delta(O_2)$ was observed near the sea floor over the shelf during upwelling.

The 2010 summer upwelling season featured atypically strong upwelling favourable winds. Persistent net equatorward flow was observed on the shelf throughout the two month deployment, a phenomenon not previously observed. Equatorward flow increased and became more surface intensified during upwelling and a sporadic, weak poleward jet was observed over the shelf break. The high variability of currents, particularly over the inner shelf, show that this region cannot be adequately characterised by sporadic research cruises.

This was the first, and to date only, deployment of a glider to observe summer

upwelling over the NWIM. This study highlights some of the challenges of using gliders to study shelf break regions, particularly when the length of time between observations over the shelf is longer than the time period of current reversals on the shelf. Despite these difficulties, a single glider was able to occupy a cross shelf section for two months, without the need for a costly ship based campaign. This study serves as a demonstration of the potential for a regularly occupied glider observatory on the NWIM. The major challenge of slow crossing speed and substantial deviation from the intended track due to the force of alongshore currents suggests that a coastal specific glider with a greater variable, and hence speed, would be a better platform to conduct this work. Future studies should plan to use a faster, more energy intensive, profiling strategy to cross the shelf more rapidly and maintain the transect.

2.9 Acknowledgments

Glider data are held at the British Oceanographic Data Centre (Rollo et al., 2020b), https://www.bodc.ac.uk/data/published_data_library/catalogue/10.5285/9b3b453b-2afb-0abd-e053-6c86abc0a59c/. Wind speed and Upwelling Index data were accessed from the Puertos del Estado database (Puertos del Estado, 2019) http://www.indicedeafloramiento.ieo.es/HBaixas/uitimeseries.ui. Bathymetry data from EMODnet Bathymetry Consortium (2018) https://portal.emodnet-bathymetry.eu/?menu=19. Heat flux data from the ERA5 Global Reanalysis was accessed via the Copernicus Climate Change Service Information (Copernicus Climate Change Service (C3S), 2017) https://cds.climate.copernicus.eu/cdsapp#!/dataset/10.24381/cds.bd0915c6. Sea surface fields from CMEMS Atlantic European North West Shelf Seas https://resources.marine.copernicus.eu/?option=com_csw&view=details&product_id=NORTHWESTSHELF_ANALYSIS_FORECAST_BIO_004_002_b. This study has been conducted using EU Copernicus Marine Service Information.

The glider deployment, and investigators JK and KJH, were supported by NERC grant NE/H012532/1. Ship work by the *RV Mytilus* was funded through the multidisciplinary project "Canaries-Iberian Marine Ecosystem Exchanges (CAIBEX)" (CTM2007-66408-C02-01/MAR)(Spanish Ministry of Education and Science). CR was supported by the Natural Environment Research Council (Grant NE/N012070/1) and the Engineering and Physical Sciences Research Council, via the NEXUSS Centre of Doctoral Training in the Smart and Autonomous Observation of the Environment.

We thank Liz Creed (formerly of iRobot, now at Hydroid) for her help during

the deployment and piloting. We thank the crew and scientists of the *RV Mytilus* who made this deployment possible. Also thanks to the piloting team at UEA who kept the glider flying on UEA's first scientific glider mission.

The comments of three anonymous reviewers greatly enhanced this manuscript.

All plots were created with Python matplotlib (Hunter, 2007), Figure 2.1 also used cartopy (Elson et al., 2020). Filled contour plots used the cmocean perceptually uniform colourmaps developed by Thyng et al. (2016).

3

Glider Observations of Thermohaline Staircases in the Tropical North Atlantic using an Automated Classifier

This chapter was submitted to the European Geosciences Union journal Geoscientific Instrumentation, Methods and Data Systems in October 2021.

Key points

- We developed a classifier to identify thermohaline staircases in glider data. This builds on the work of van der Boog et al. (2021b) with increased generalisation and flexibility.
- We identified two periods of thermohaline staircasing and breakdown during a month of measurements in the tropical North Atlantic.
- We hypothesise four criteria that must be met for extensive staircases to form and persist in this region.

Abstract

Thermohaline staircases are stepped structures of alternating thick mixed layers and thin high gradient interfaces. These structures can span several hundred meters vertically, containing mixed layers several tens of metres thick. Thermohaline staircases are associated with double-diffusive mixing. Thermohaline staircases occur across broad swathes of the Arctic and tropical/subtropical oceans and can increase rates of diapycnal mixing by up to five times the background rate, driving substantial nutrient fluxes to the upper ocean. In this study, we present an improved classification algorithm to detect thermohaline staircases in ocean glider profiles. We use a dataset of 1162 glider profiles from the tropical North Atlantic collected in early 2020 at the edge of a known thermohaline staircase region. The algorithm identifies thermohaline staircases in 97.7 % of profiles that extend deeper than 300 m. We validate our algorithm against previous results obtained from algorithmic classification of Argo float profiles. Using fine resolution temperature data from a fast-response thermistor on one of the gliders, we explore the effect of varying vertical bin sizes on detected thermohaline staircases. Our algorithm builds on previous work with improved flexibility and the ability to classify staircases from profiles with poor salinity data. Using our results, we propose that the incidence of thermohaline staircases is limited by strong background vertical gradients in conservative temperature and absolute salinity.

3.1 Introduction

Thermohaline staircases consist of subsurface layers of near homogeneous salinity and temperature (referred to here as mixed layers), separated by thin layers with large temperature and salinity gradients (gradient layers). Staircases formation and growth are driven by double-diffusive processes that arise from

the difference between the molecular diffusivities of heat and salt. Heat diffuses 100 times faster than salt (Stern, 1960). Thermohaline staircases form where the vertical gradients of temperature and salinity have the same sign. These conditions most commonly occur in the Arctic, where cool fresh waters overlie warm salty waters, and tropical/subtropical regions where warm salty surface waters overlie cool, fresh waters. Previous work by Schmitt et al. (2005) estimated that thermohaline staircases raise diapycnal mixing rates in the tropical North Atlantic by a factor or five. Mixing rates control critical oceanographic processes including nutrient fluxes (Oschlies et al., 2003) and the meridional overturning circulation (Kuhlbrodt et al., 2007). Due to their effect on mixing, the global incidence of thermohaline staircases, and the mechanisms that govern them, are the subject of ongoing research.

The effects of thermal expansion and haline contraction on seawater are critical to the formation of thermohaline staircases. The effects of these are often represented by two derived properties, the density ratio $R_\rho = \alpha\theta_z/\beta S_z$ and the Turner angle $Tu = tan^{-1}(\alpha\theta_z - \beta S_z, \alpha\theta_z + \beta S_z)$, where α is the thermal expansion coefficient, β is the haline contraction coefficient, θ_z and S_z are the vertical gradients in conservative temperature and absolute salinity (Ruddick, 1983). The density ratio can be calculated from the Turner angle with $R_\rho = -tan(Tu + 45°)$ (You, 2002). The Turner angle categorises the water column into sections that are statically unstable, prone to salt fingers, prone to diffusion-convection or doubly stable (Ruddick, 1983).

In this study of the tropical North Atlantic, warm salty Subtropical Underwater (22 - 25 °C, 37.0 - 37.6 g kg^{-1}) overlies cooler fresher Antarctic Intermediate Water (4-6 °C, 34.7-35.0 g kg^{-1}) (Fer et al., 2010). In this case, the mechanism driving mixing in the gradient layers is salt finger instability (Radko, 2005). This instability can spontaneously transform smooth, statically stable profiles into stepped patterns such as those in Fig. 3.1. This instability can occur where $45° \leq T_u \leq 90°$ (Figure 3.1.c). Laboratory and theoretical studies have concluded that diapycnal mixing rates of heat and salt are elevated in thermohaline staircases (Schmitt, 1981 & Radko and Smith, 2011). This study aims to improve detection and quantification of thermohaline staircases using ocean gliders. Ocean gliders are used as they can collect more CTD profiles than a single research vessel. However, these observations are only useful if staircases can be accurately and efficiently identified.

Ocean gliders are useful platforms for the observation of thermohaline staircases as they can occupy a virtual mooring far more cheaply than a ship, enabling collection of more profiles. Unlike Argo floats, gliders can hold station, collecting a time series of temperature and salinity profiles at a fixed location. As we are

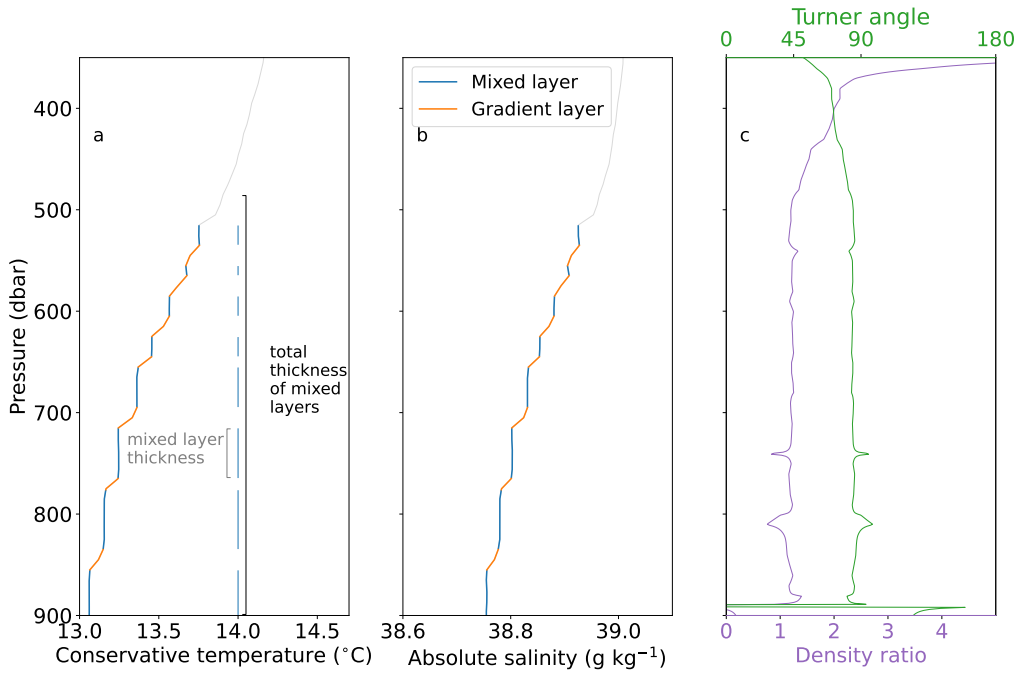

Figure 3.1: Example thermohaline staircase from Argo float 6901769 at 8.9° E, 37.9° N. Grey line is 1 dbar averaged temperature (a) and salinity (b), with blue and orange lines marking the identified steps of the staircase. (c) Corresponding profiles of Turner angle and density ratio.

interested only in the large scale structure of thermohaline staircases, the reduced accuracy of an umpumped glider CTD compared to a pumped ship based system is not a hindrance. Ships are better suited to synoptic studies such as that by Schmitt et al. (1987) as they can rapidly cover a large area. Argo floats have been used to great effect to analyse large scale trends in thermohaline staircases van der Boog et al. (2021b). Gliders are most useful for holding station in a region of interest, such as the tropical North Atlantic, and collecting a long timeseries of profiles.

The tropical North Atlantic has been known to host thermohaline staircases since the 1970s (Schmitt et al. (1987), and references therein). Using ship CTD casts and expendable bathythermographs (XBTs) from ships and aircraft, thermohaline staircases were identified over an area exceeding one million square kilometres by the C-SALT experiment (Schmitt et al., 1987). Staircases were observed at depths of 420-650 m, with individual steps 5-30 m thick. Subsequent studies using a fast-response thermistor chain (Marmorino et al., 1987), tracer release and fine-structure high resolution profilers (Schmitt et al., 2005), seismic oceanography (Fer et al., 2010) and Argo floats (van der Boog et al., 2021b), henceforth VDB, have observed staircases with similar bulk statistics in this region. See Table 5 of VDB for more details. The area identified as strong or weak staircase by Schmitt et al. (1987) appears to be

consistent in time, with subsequent studies by Marmorino et al. (1987) and Fer et al. (2010) observing breakdowns of steps at the edges of these zones. The extent of the thermohaline staircase zone is defined by thermohaline properties. Thermohaline staircases are not observed outside of the area where $R_\rho < 1.7$ (Schmitt et al., 1987).

While the exact formation mechanisms of thermohaline staircases are still a topic of discussion (Radko, 2020), VDB, several key conditions have been identified. Firstly, the Turner angle must fall in the regime favourable to double diffusive processes of diffusion-convection ($-90° \leq T_u \leq -45°$) or salt finger ($45° \leq T_u \leq 90°$). Secondly, the density ratio must be within a critical range. The lower bound for R_ρ is 1, where the gradients in salinity and temperature balance and there is no density stratification. Bryden et al. (2014), Schmitt et al. (1987) and Fer et al. (2010) all observed well ordered staircases up to $R_\rho = 1.7$, with irregular "steppy" profiles up to R_ρ of 2.0 or greater. Theoretical work by Radko (2005) suggests that staircases can only form at $R_\rho < 2$. Fer et al. (2010) consider the range $1 < R_\rho < 2.5$ as conducive to forming thermohaline staircases in the tropical North Atlantic. Energetic features such as velocity shear, slope currents and internal waves can prevent the formation of staircases (Fer et al., 2010; Buffett et al., 2017); though in some cases, the staircases are strong enough to resist breakup (Schmitt et al., 1987), and can even dampen internal wave activity (Radko, 2020). In this paper we suggest that strong vertical gradients in salinity and temperature also reduce the maximum size of mixed layers in thermohaline staircases.

To explore the incidence and structure of thermohaline staircases in the tropical North Atlantic, we analysed over 1000 profiles collected by three ocean gliders in early 2020. Gliders have previously been used to observe thermohaline staircases in the Tyrrhenian Sea in the Mediterranean, primarily to relate seismic reflectors to thermohaline structures (Buffett et al., 2017). However this study is, to our knowledge, the first of its kind in the tropical North Atlantic. This is also the first study to identify thermohaline staircases in glider profiles algorithmically. The large number of profiles collected necessitate an automated classifier, rather than the manual classification previously used on glider datasets. Data collection is detailed in Sect. 3.2. The thermohaline classifier is described in Section 3.2.2. Results are presented in Section 3.3 and discussed in Section 3.4, with subsections on scale sensitivity and classifier limitations in Section 3.4.2 and Section 3.4.3. We summarise our conclusions and recommendations for future avenues of study in Section 3.5.

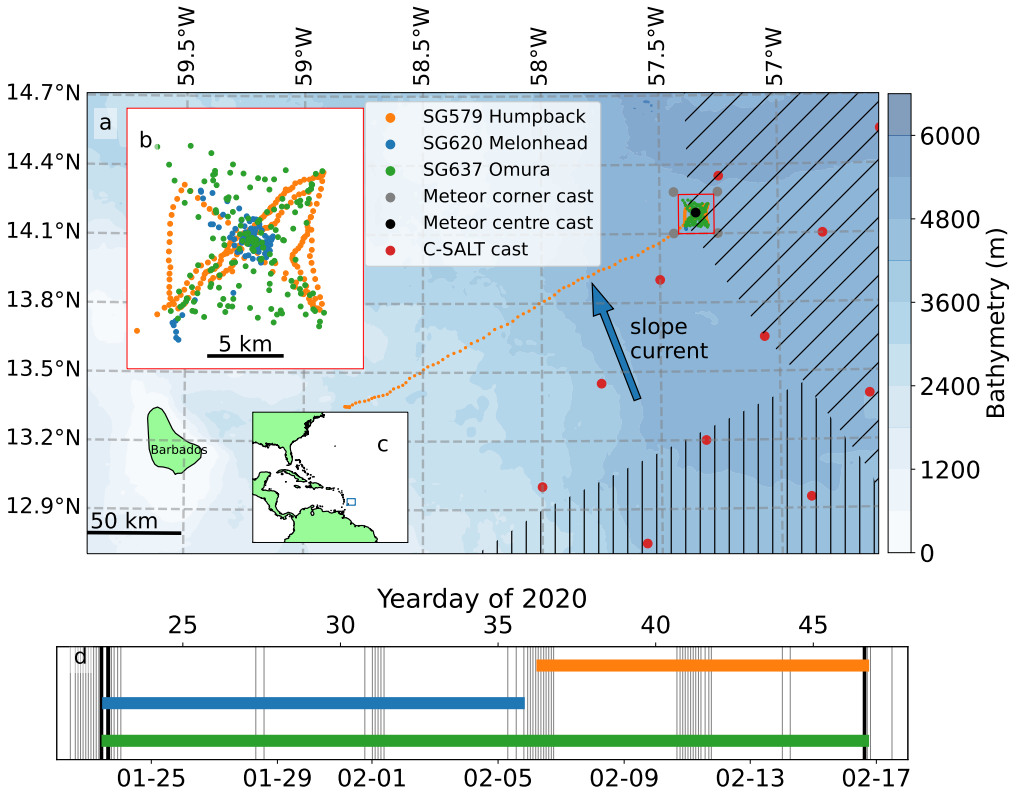

Figure 3.2: (a) Glider survey map. Red dots are CTD casts conducted during the C-SALT experiment in Spring 1985 (Schmitt, 1987). Diagonal and vertical hatching respectively delineate the approximate areas of strong and weak staircases identified by Schmitt et al. (1987). (b) Zoomed detail of bowtie outlined in red on (a). (c) regional context of the area, with area displayed in (a) outlined in blue. (d) Temporal overlap of glider observations at the bowtie and nearby *Meteor* CTD casts. *Meteor* corner casts were taken at grey dots on map. *Meteor* centre casts were taken at the black dot. Colours match legend in (a).

3.2 Data collection and processing

3.2.1 Glider data

During January and February 2020, the RV *Meteor* surveyed the tropical North Atlantic, 200 km ENE of Barbados (Figure 3.2), as part of the EUREC^{4}A campaign (Stevens et al., 2021). During this cruise, the UEA glider group deployed three Seagliders. Seagliders are small buoyancy powered autonomous vehicles with wings that dive with a sawtoothed profile (Eriksen et al., 2001). Seagliders dive to a maximum of 1000 m with a vertical speed of around 0.1 m s^{-1}. In contrast to Argo floats, gliders are capable of manoeuvring to maintain position or follow a survey pattern. Here, each glider dive limb is treated as a separate profile, so that a single descent-ascent cycle yields two profiles. The temporal overlap and dive depths of the three gliders are shown in Figure 3.3. All glider dives were completed within the 10 km wide bowtie

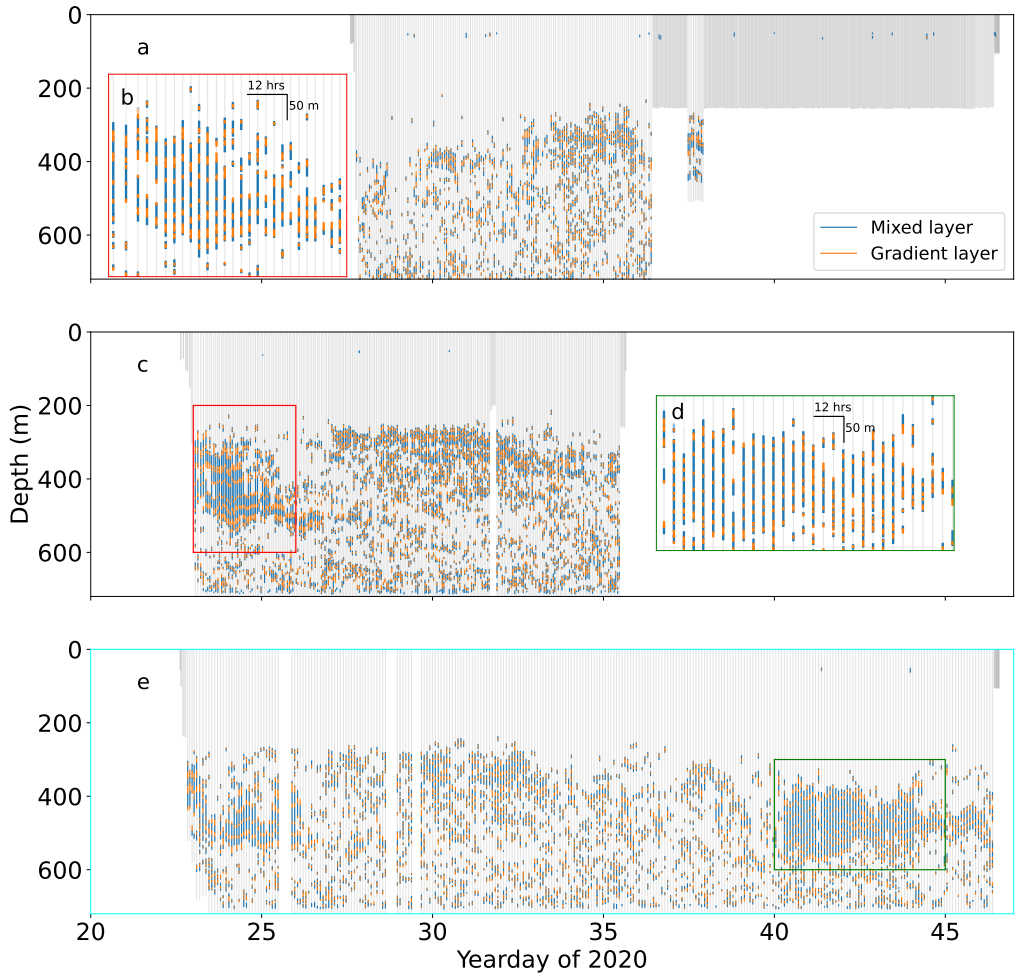

Figure 3.3: All thermohaline staircases detected in glider profiles. (a, c & e) data from gliders SG579, SG620, and SG637 respectively. (b & d) show expanded sections from boxes in c & e in the corresponding colour. Data from (e) are the basis for remaining figures in this manuscript, except where otherwise stated.

pattern shown in Figure 3.2 except SG579, which was deployed 150 km SW of the bowtie and arrived on yearday 36, February 6. Gliders SG579, SG620 and SG637 completed 295, 131 and 155 dive cycles respectively, yielding a total of 1162 profiles for analysis. The gliders sampled every 5 seconds, for a vertical resolution of approximately 0.5 m. Owing to a shallow dive slope, SG637 stalled during dives 22, 23, 41, 42, 43, and 47. Glider stalling reduces water flow through the unpumped CT sail, affecting temperature and conductivity measurements. We removed these dives from the dataset, as can be seen in the gaps in Figure 3.3.e.

Glider profiles were processed using the UEA Seaglider Toolbox (Queste, 2014). This included tuning the hydrodynamic flight model following Frajka-Williams et al. (2011) and thermal lag corrections following Garau et al. (2011). After processing the glider profiles, temperature and salinity profiles were compared

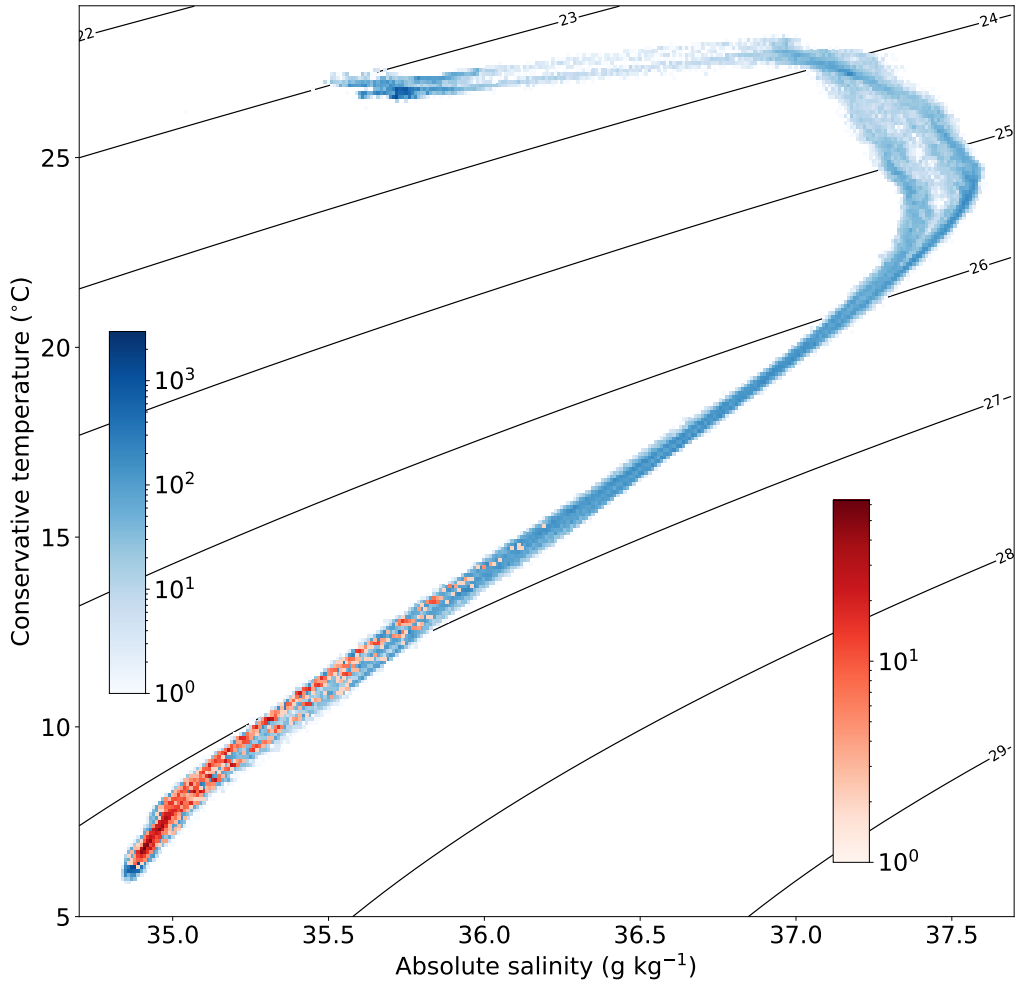

Figure 3.4: Observation density of SG637 temperate and salinity measurements (blue) and identified mixed layers (red). Spacing of the grid is 0.01 g kg^{-3} in absolute salinity and 0.1 °C in conservative temperature. Colour scales are the number of observations in each grid cell. Black lines are isopycnals.

with CTD casts conducted by the *Meteor* (black vertical lines in 3.2.d). Quality controlled CTD profiles were provided by D. Baronowski (Baranowski, 2020). At the bowtie, SG637 dived to 750 m for 25 days, completing a dive approximately every 4 hours. SG579 only dived to 250 m and SG620 was recovered after 13 days. As SG637 recorded the most comprehensive set of observations, it is used for the majority of the subsequent analysis.

To apply the thermohaline staircases classifier to the dataset, we require data at regular depth intervals to ensure that features are consistently identified throughout the dataset. To achieve this, each profile was binned into 1 m depth bins using the median value of samples within the bin. We chose 1 m vertical gridding initially for comparability with VDB's results. The effects of varying bin thickness are discussed in Section 3.4.2. Derived variables including the

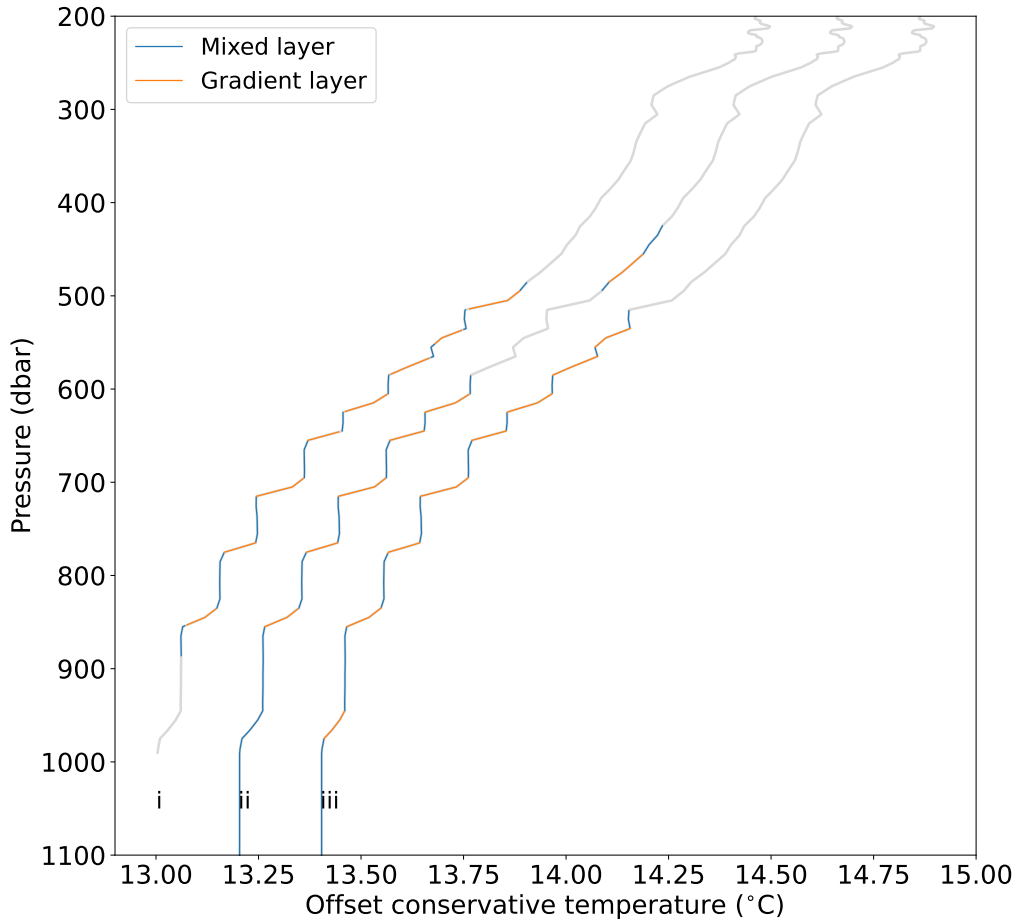

Figure 3.5: The same Argo profile shown in Figure 3.1 classified three times. Three lines on this plot are (i) VDB's result, (ii) our classifier on default settings, and (iii) our classifier with a 10 % decrease in step height ratio and 4 % decrease in maximum permitted density gradient. The first profile is at the correct temperature, subsequent profiles are offset by 0.2 °C

Turner angle, density ratio and vertical gradients in salinity and temperature were calculated at 1 m intervals using a 50 m vertical bin to ensure smooth profiles, following the methods of VDB. A 50 m averaging interval is used as a smaller depth interval can be influenced by individual staircase steps (Shibley et al., 2017). Throughout this paper, temperature refers to conservative temperature, salinity refers to absolute salinity and density refers to potential density. All were calculated using the gsw toolbox implementation of TEOS-10 (Mcdougall et al., 2010; McDougall et al., 2011). Yeardays are used throughout the paper. Yeardays start at 0 on the first of January 2020. Figure 3.2.d uses both yeardays and calendar dates for comparison.

3.2.2 Thermohaline staircase classifier

To evaluate thermohaline staircases in glider profiles, we wrote a classifier following VDB. VDB's detection algorithm, identifies thermohaline staircases in a CTD profile using five steps:

1. Parts of the profile with vertical temperature, salinity and density gradients below a threshold value are classed as mixed layers.

2. Sections between mixed layers are preliminarily classed as gradient layers

3. Gradient layers are excluded if they exceed a maximum thickness, are thicker than the neighbouring mixed layers, or exhibit less variability in salinity and temperature than neighbouring mixed layers. This ensures that mixed layers are separated by thin, steep interfaces.

4. Gradient layers are classified into a double diffusive regime: salt-finger if the overlying mixed layer is warmer and saltier than the underlying mixed layer, diffusive-convective if the overlying mixed layer is cooler and fresher than the underlying mixed layer.

5. Staircases are identified as uninterrupted series of steps in the same diffusive-convective regime. This step removes thermohaline intrusions.

VDB's algorithm was designed to classify a global database of Argo profiles. It performs this duty well, but was specifically written to ingest Argo formatted profiles at 1 dbar vertical resolution. Due to hard coded aspects of VDB's algorithm, it was not possible to apply it directly to our glider dataset. In particular, we aimed to test the effect of varying the vertical bin thickness on the classification of staircases. This is explored in Section 3.4.2. To identify staircases in our dataset, we built our own classifier (Rollo, 2021a) following the steps outlined in VDB, with the following adaptations:

- Able to process profiles at any regularly spaced step in pressure or depth.

- Optional user-defined maximum mixed layer height.

- Optional plotting to show which layers are identified and discarded at each of the steps outlined by VDB in Section 3.

- Option to classify step shape using only vertical variation in temperature, rather than temperature, salinity and density. This is useful if salinity data are poor or recorded as a lower frequency than temperature, as is the case when using a fast-response thermistor.

- Each processing step as a separate, documented function.

- Software tests and validation against synthetic and field data.
- Software published in version-controlled repository (GitHub) to retain full development history.

These adaptations were driven by a need for greater flexibility in the classifier, and requirements imposed by the glider profiles. Substantial salinity spikes were present in the salinity profiles from all three gliders (Figure 3.7.b orange line). To remove these spikes, a 5 m mean boxcar moving average filter was applied to the salinity profiles fed to the classifier (Figure 3.7.b, green line). This removed the spikes, but smoothed the edges of the steps that the classifier identifies. To resolve this problem, we made the classifier able to identify the shape of steps using only temperature profiles. In this mode, salinity profiles are used to classify the staircase into the salt finger regime or the diffusive-convective regime. The classifier includes software tests to ensure that this use of temperature only for initial classification does not change the identification of staircases.

There were no Argo floats in the vicinity when our gliders were deployed, so we could not compare the output of our algorithm and VDB's algorithm on profiles from the EUREC^{4}A campaign. Instead, we applied our classifier to the Argo profile used as a demonstration of VDB's algorithm by VDB Figure A2. The results of this comparison are shown in Figure 3.5. The threshold values used by VDB identity most of the steps in the profile, however, we found that a 10 % decrease in step height ratio and a 4 % decrease in maximum density gradient successfully classified the deepest, shallow gradient layer at 950 m and correctly classified the smaller steps at the upper reaches of the staircase (Figure 3.5 iii). These threshold values are location dependant and some adjustment must be made to make the best classification possible.

Our classifier identified 14205 thermohaline steps in the glider profiles. The glider dataset comprised 1162 vertical profiles recorded over 56 glider days. To make quantitative comparisons across the dataset, we use bulk statistics to analyse how the staircases changed over time. We define total thickness of mixed layers to be the total vertical extent of the profile identified as a part of a mixed layer in the thermohaline staircase, as shown in Figure 3.1.a. Mean mixed layer thickness is similarly calculated on a per-profile basis. Calculating these bulk values enables us to evaluate the temporal evolution of thermohaline staircases, and visualise datasets too large to plot directly.

3.3 Results

Thermohaline steps were identified in 97.7 % of profiles that extended below 300 m. In profiles with at least one mixed layer, the mean number of mixed

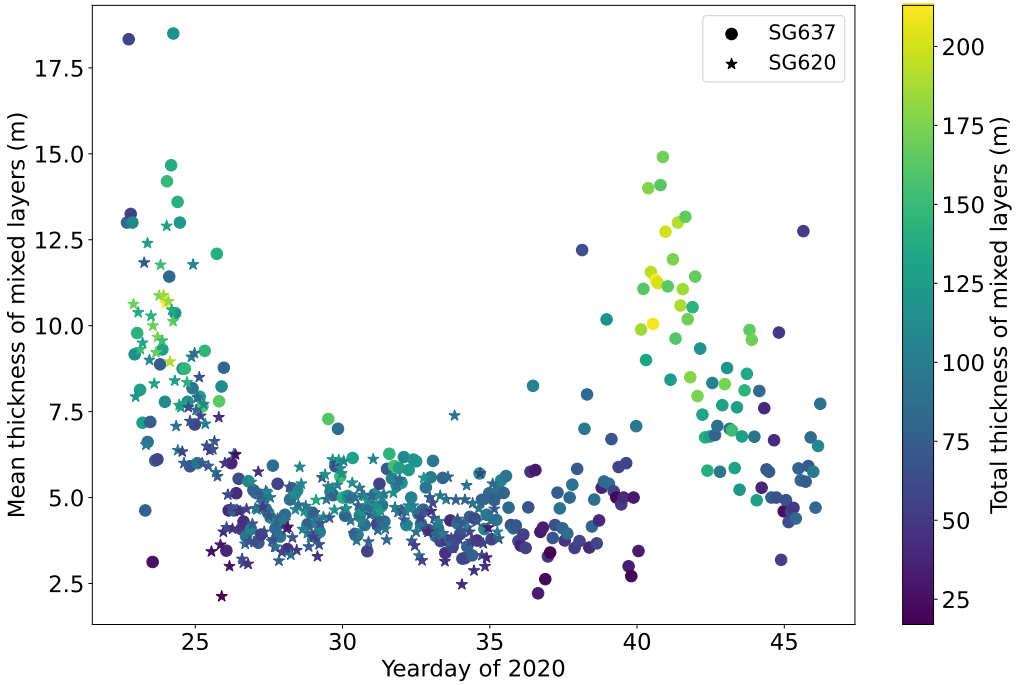

Figure 3.6: Mean thermohaline staircase mixed layer thickness observed by SG620 and SG637.

layers per profile was 14.3. However, coherent series of large steps were more restricted, both temporally and spatially. Staircases with more than three steps greater than 20 m were only observed at the bowtie, and only on two occasions: Yearday 23-25 (Figure 3.3.b) and yearday 40-44 (Figure 3.3.d). The changing thickness of steps is represented in Figure 3.6 which shows the two events of strong staircasing as peaks in mean mixed layer thickness and total mixed layer thickness. The small differences between values recorded by SG637 and SG620 can be attributed to the distance between the two gliders, typically $\approx$ 5 km (Figure 3.2).

SG579 observed few steps at its deployment location. As SG579 travelled eastward larger staircases were encountered and the minimum observed depth of staircases decreased. A front was observed by SG579 as the glider passed over the continental slope on yearday 34. Decreases of 0.5 °C and 0.2 g kg^{-3} in the uppermost 3 m coincided with a peak in chlorophyll a fluorescence and a broad along-slope current of 15 cm s^{-1}. Once past the front and over the abyssal plain, SG579 observed larger and more coherent staircases similar to SG620 and SG637 (Figure 3.3.a). Total mixed layer thickness increased from 58 $\pm$ 25 m to 90 $\pm$ 26 m after yearday 34. Total thickness of mixed layers quantifies the amount of the water column that will experience the effects of increased diapycnal mixing rates Schmitt et al. (2005). In the salt finger regime, the magnitude of property change between steps does not affect effective

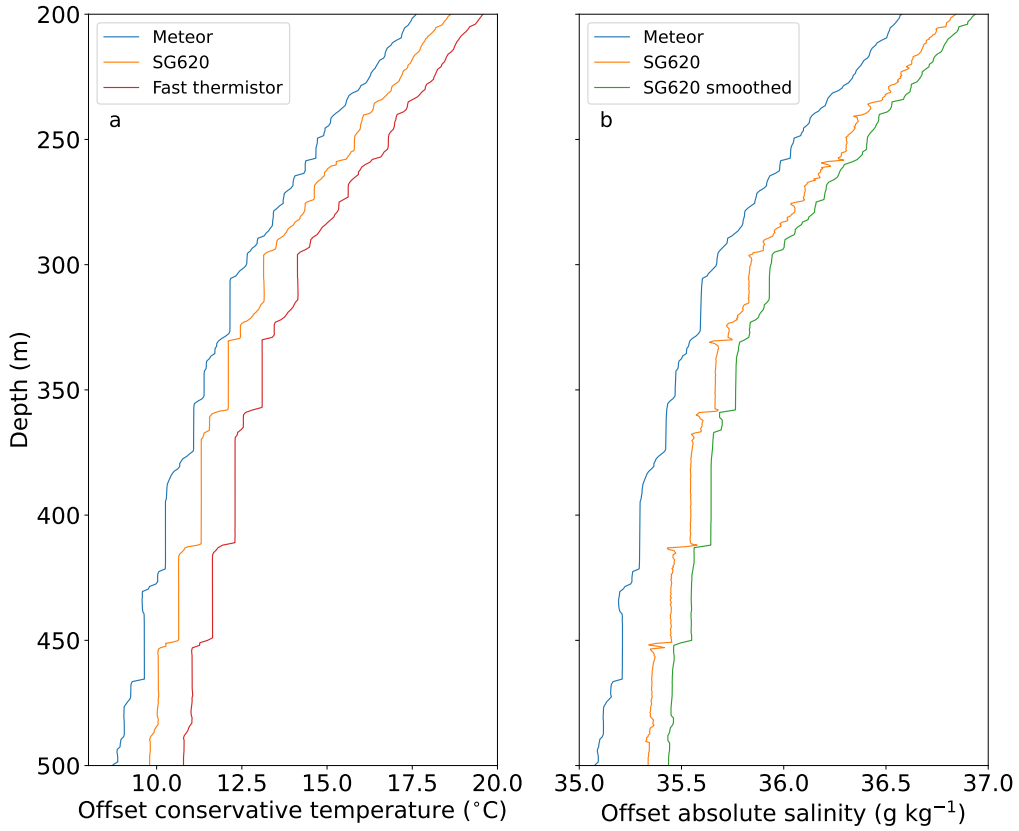

Figure 3.7: (a) Temperature profiles from *Meteor* CTD, SG620 CT sail and fast-response thermistor. (b) Salinity from *Meteor*, salinity from SG620 and SG620 salinity smoothed with a 5 m mean window. The profile from the *Meteor* was taken at the same location 24 hours before the glider dive. As in Figure 3.5 the first profiles is correct, subsequent vertical profiles are offset by 1 °C or 0.1 g kg^{-3}

diffusivities, only the vertical extent is important (van der Boog et al., 2021a).

SG637 observed a sloping front later in the mission. First observed at 200 m on yearday 35, the front reached 750 m, the maximum dive depth of the glider, on yearday 40 (Figure 3.8 a&c). Previous observational studies also observed fronts in the area at depths of 200 - 700 m Marmorino et al. (1987). The passage of this front was followed by the second period of large, coherent staircases at 400-600 m, with total mixed layer thickness increasing from 60 ± 23 m during the passage of the front to 146 ± 38 m in the three days following yearday 40.

Using the observations of all three gliders, we calculated bulk statistics following VDB. Ranges quoted are the 2.5 and 97.5 percentiles: Depth 277-858 m, temperature steps 0.01-0.69 °C, salinity steps 0.001-0.12 g kg^{-3}, gradient layer thickness 1-12 m, mixed layer thickness 1-21 m. The smallest features resolvable within our dataset are 1 m thick. 73 % of the steps identified were in the salt-finger regime. Mixed layer thickness varied with R_ρ (Figure 3.11), the largest staircases were observed around $R_\rho = 1.7$, with a thick tail of steps at

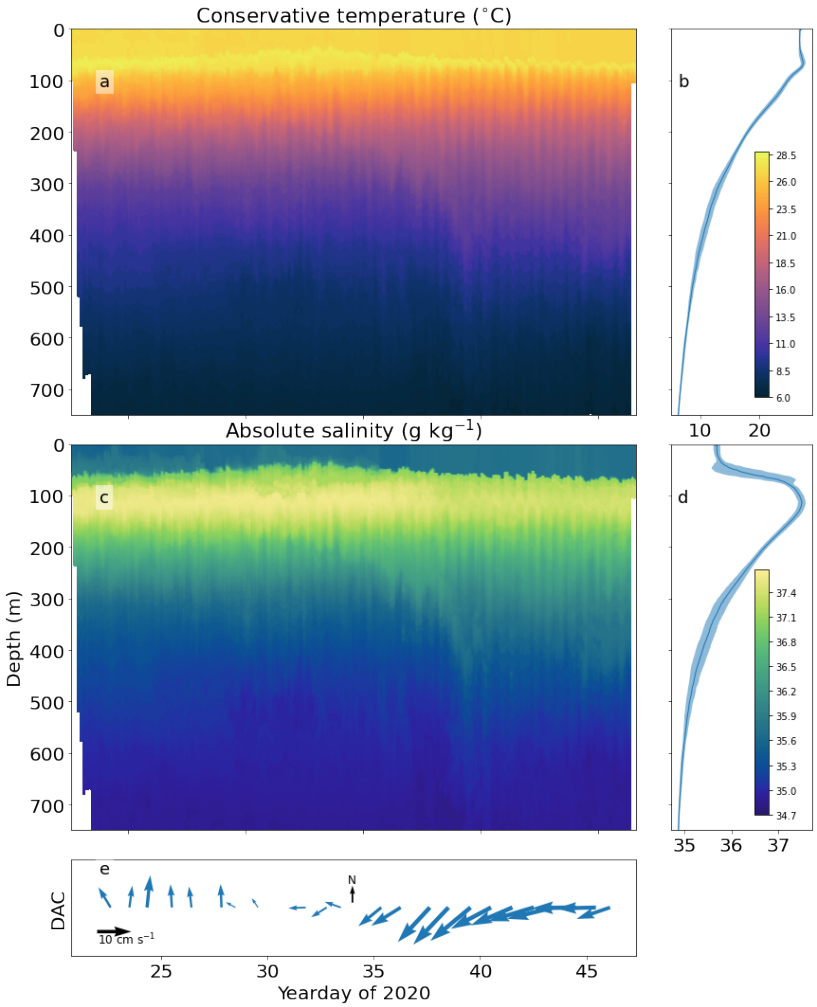

Figure 3.8: (a) Gridded mean conservative temperature from SG637. (b) Mean conservative temperature profile with uncertainty of 1 standard deviation shaded. (c & d) as (a & b) for absolute salinity. (a & c) gridding is 1 m vertically performed on a per-profile basis. (e) Daily mean of the dive average current (DAC).

larger values of R_ρ. No steps were observed at $R_\rho < 1$ (Figure 3.11).

Staircases in the salt finger regime require a Turner angle between 45 and 90 degrees (red area of Figure 3.9a) and a density ratio between 1 and 2.5 (Figure 3.9b). These constraints alone do not explain the distribution of thermohaline staircases in the glider profiles we collected. The absolute vertical gradients of temperature and salinity (Figure 3.9.c & d) partially account for this difference between the expected distribution of staircases and the observed distribution. The vertical gradients are calculated over 50 m to prevent individual thermohaline steps from affecting the results, in the same manner as the Turner angle is calculated (Shibley et al., 2017). Using the critical values of Turner angle and density ratio, as well as upper limits of temperature and salinity gradient, we construct masks of where we expect thermohaline staircases to

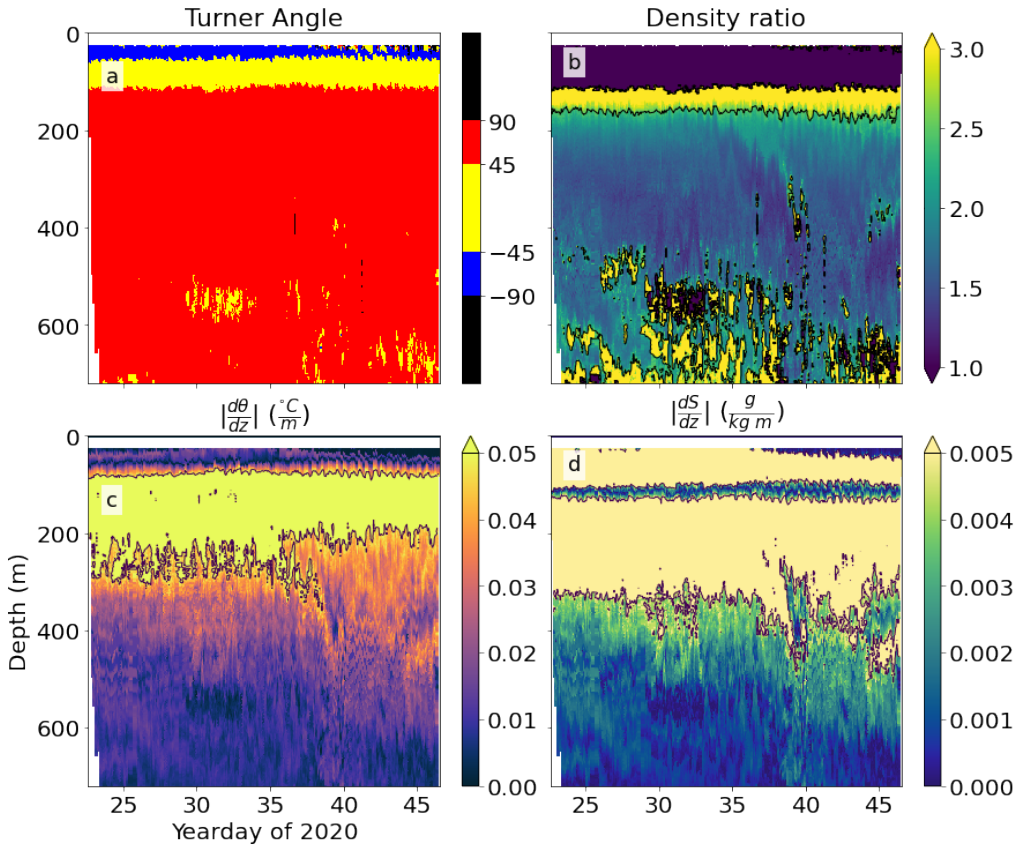

Figure 3.9: Key variables for the formation of thermohaline staircases, calculated from SG637 profiles. a) Turner angle b) density ratio c) absolute vertical temperature gradient d) absolute vertical salinity gradient.

form. These masks are shown in Figure 3.10, with a combined mask of the area that matches all criteria in Figure 3.10 d. These masks suggest that staircases with steps larger than 1 m do not form where the absolute vertical gradients in temperature or salinity exceed 0.05 °C m^{-1} or 0.005 kg m^{-3} respectively.

3.4 Discussion

3.4.1 Thermohaline staircases

The structures we observed during periods of strong staircasing are very similar to those encountered during the C-SALT campaign. Schmitt et al. (1987) recorded mixed layers of 5-30 m thickness separated by gradients with temperature and salinity jumps of 0.5-0.8 °C and 0.1-0.2 psu in the area identified as strong staircasing. The glider bowtie is at the edge of this region (Figure 3.2). This may explain why we did not observe coherent staircases throughout our observational period. Fer et al. (2010) also conducted their observations at the edge of the strong staircasing zone identified by C-SALT and observed intermittent staircases. The location of our observations at the

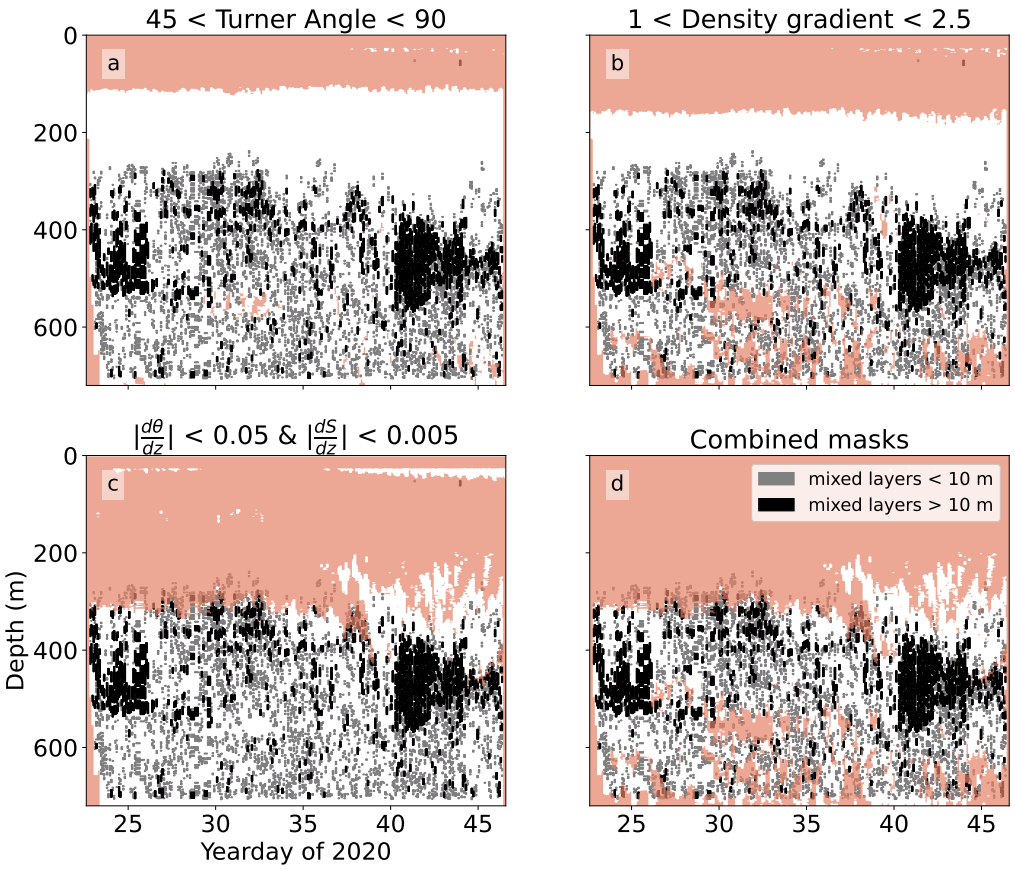

Figure 3.10: Masks shading the conditions in Figure 3.9. Red areas mask where the conditions are not met. Grey blocks are the location of thermohaline mixed layers, black blocks are mixed layers thicker than 10 m.

edge of the staircase zone would also explain the slightly smaller step sizes and temperature and salinity changes observed compared to the averages reported by Schmitt et al. (1987) who observed staircases with the thickest steps and largest changes in temperature between 10° and 14° N, 52° and 57° W, to the southeast of our glider observations. The rapid apparent breakdown of staircases confirms observation by Marmorino et al. (1987) of thermohaline layers disappearing over a distance of a few km. Due to the sampling pattern of the gliders, we cannot definitively determine whether this rapid transition from staircase to non-staircase is a breakdown in the structure or the advection of the edge of the staircase zone past the glider bowtie. Given the historic extent of the staircases in this region (Figure 3.2) and their known persistence of at least 6 months (Schmitt et al., 1987), the latter explanation is more likely.

Density ratio is generally assumed to be the main factor controlling thermohaline staircases formation and persistence. In agreement with previous studies in this region and elsewhere, we observed the largest steps around $R_\rho = 1.7$ (Figure 3.11). However, we also observed mixed layers at substantially larger R_ρ, though the

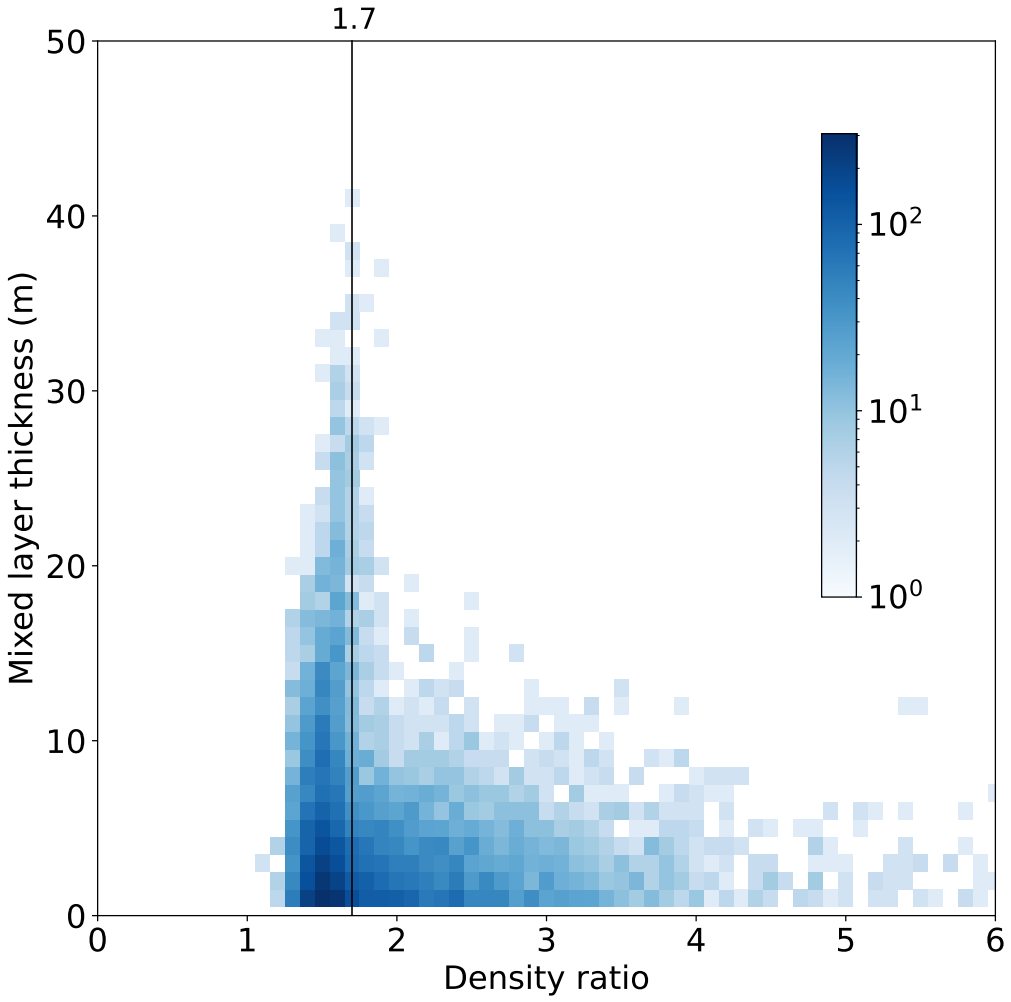

Figure 3.11: Observations of mixed layers classified from all three gliders between 100 and 800 m depth. Colourbar shows number of observations in each grid cell. Cell spacing of 0.1 in density ratio, 1 m in mixed layer thickness. Vertical black line marks the density ratio of 1.7.

maximum thickness of these layers was smaller, as predicted by Radko (2005). R_ρ alone cannot account for the incidence of staircases; we do not observe staircases shallower than 250 m, despite the favourable density ratio (Figures 3.9b and 3.10b). Similarly, Schmitt et al. (1987) did not observe any staircase structure at the R_ρ minimum around 200 m depth, concluding that $R_\rho < 1.7$ is a necessary but not sufficient condition for the formation of staircases. More recent studies (e.g. (van der Boog et al., 2021a)) which classify a much larger number of profiles from a range or regions, use a broader criteria for density ratio of $1 < R_\rho < 10$. This suggests that the upper limit of R_ρ may be better understood as an observational limitation of coarsely sampled profiles than a physical restriction of the incidence of thermohaline staircases.

We propose that strong background vertical gradients in temperature and salinity

prevent the formation of thermohaline staircases. As shown in Figure 3.9, the water column at 200-250 m has a Turner angle and density ratio conducive to staircasing, but also has large gradients in temperature and salinity (greater than 0.05 $^{\circ}C\ m^{-1}$ 0.005 $g\ kg\ m^{-1}$ respectively). Combining masks of all four key variables creates a better predictor of where staircases of large steps will form, particularly those with steps greater than 10 m in thickness (Figure 3.10). This lack of steps in the upper pycnocline, also reported by Schmitt et al. (1987) & Fer et al. (2010) could also be due to observational limitations. In a manner analogous to internal waves, large steps form where background gradients in temperature and salinity are small (Figure 3.5). This is most apparent in the Mediterranean, where the largest steps of several hundreds of metres are found deep in the water column, where background gradients are very small (Buffett et al., 2017). Where background gradients are strong, we would expect small thermohaline steps, possibly below the resolution of our 1 m binned profiles.

Strong horizontal velocity and shear can disrupt thermohaline staircases (Fer et al., 2010). The only velocity data we have for this study are vertically averaged currents from the glider flight model. These data show strong velocities where SG579 crossed the slope current (Fig. 3.2) and when the slope obsered by SG637 between yearday 35-40 (Fig. 3.3). Both of these events corresponded with a decrease in the observed extent of thermohaline staircases. We do not have shear data to compare, but these two observations support those of Fer et al. (2010) that strong velocities disript thermohaline staircases.

The contributions of salt finger theromohaline staircases to vertical diffusivities of heat and salt are calculated using an empirical formula (van der Boog et al., 2021a). The contribution of thermohaline staircases to vertical diffusivities is proportional only to the density ratio, not to the magnitude of the temperature or salinity changes across the step. As such, small thermohaline steps that are present in regions with large density ratio, such as those in at the upper edge of the stiarcase zone in this study, can cause a substatial increase in vertical fluxes of heat and salt. These small steps are the structures most likely to be missed in coarsely sampled profiles. As such, thermohaline staircases would benefit from more fine resolution profiling, such as those observed by microstructure gliders.

Predicting the presence of thermohaline staircases from background gradients can have practical benefits for sub-grid parametrisation. Thermohaline staircases in the tropical North Atlantic can increase diapycnal mixing rates by a factor of 5 (Schmitt et al., 2005). Previous studies have shown that thermohaline staircases occur mostly in well-defined regions (van der Boog et al., 2021a). Building on previous work, this study suggests that a set range of vertical temperature and salinity profiles are conducive to the formation of

thermohaline staircases. Where these characteristic profiles are present in models, differing vertical diffusivities of heat and salt can be applied to parameterise the enhanced vertical diffusivities caused by double-diffusive processes. Most ocean models lack sufficiently fine vertical resolution to directly represent thermohaline staircases comprised of mixed layers $\approx$ 10 m and gradient layers $\approx$ 1 m in the open ocean environment where thermohaline staircases are most often found. The enhanced diapycnal mixing driven by staircases could be parametrised where key conditions are met, removing the need for direct representation of staircases.

The acoustic impedance contrast across a thermohaline step is an ideal reflectors for seismic oceanography. Previous studies (Fer et al., 2010; Buffett et al., 2017) have successfully exploited this characteristic to map out thermohaline staircases over large spatial scales. Often, these 3D maps of staircases are constructed from seismic data and XBTs. Gliders can ably complement the analysis of seismic data. Gliders are particularly valuable for their ability to maintain station or sample a specific region distant from the ship conducting the seismic survey, unlike free floating Argo floats of XBTs which are single use and must be deployed at the required site by ship or aircraft. Seagliders are a useful tool for observing thermohaline staircases in the tropical North Atlantic as the staircases are observed only in the uppermost 800 m (Schmitt et al., 1987, 2005), well within Seagliders 1000 m maximum depth rating. This study has proven the usefulness of gliders in this region. Future seismic oceanography studies in the tropical North Atlantic could benefit from the inclusion of gliders in a similar manner to Buffett et al. (2017).

This is a small study, with less than two months of observations. More work should be done to test this hypothesis and the critical values of temperature and salinity gradients. It would be beneficial to test if observations in other staircasing regions such as the Arctic and Mediterranean exhibit similar behaviour. In particular, staircases in Arctic regions dominated by diffusive-convective processes typically have smaller steps than those in the salt finger regime (VDB). A high resolution glider dataset from the Arctic could reveal more small scale staircases than Argo floats are capable of resolving.

3.4.2 Scale sensitivity of the classifier

One of the key variables not tested by VDB is the vertical spacing of profiles. We took advantage of a high resolution temperature sensor to test the classifier's sensitivity to varying vertical spacing. In addition to a CT sail, SG620 was equipped with a Rockland Scientific microstructure system, including an FP07 fast-response thermistor. The fast-response thermistor sampled at 512 Hz with

a response time of ≈ 10 ms, measuring temperature at a spatial resolution of ≈ 1 mm. We binned the temperature profiles at 0.2, 1 and 5 m to test the effect of vertical bin size on the classifier. Each binned value is the median of all samples within the bin. Even at 0.2 m bin size, each bin average is calculated from over 100 measurements. Salinity values were taken from the nearest CT sail measurement, and the classifier picked steps based solely on temperature structure. An example profile at the three binning intervals is shown in Figure 3.12. The gaps between adjacent mixed and gradient layers are clear in the 5 m binned profile, as a point cannot be part of both the mixed and gradient layer (Figure 3.12b).

When classifying profiles, the three bin sizes give similar results. The differences are most obvious at the upper edge of the staircase zone, where individual steps are smaller (Figure 3.12c). The 5 m binned profile completely erases the ≈ 2 m thick steps. The 1 m binned profile also misses the steps, as the ≈ 50 cm thick gradient layers contain at most 1 point. Our classifier requires two points in the gradient layer to classify it. This sets a minimum layer thickness equal to twice the bin size, a limitation shared with VDB's algorithm. A separate issue is apparent with finely binned profiles. Using a smaller bin size, the 40 m thick step around 420 m is excluded (Figure 3.12b). This is due to the increased variability introduced by the extra points in the profile, exceeding the maximum allowable temperature variation and causing the step to be discarded. Reconciling these behaviours will be a challenge for future iterations of the classifier. Perhaps a more sophisticated moving average filter than the simple boxcar used here could smooth out small perturbations in temperature while retaining the sharp shape of the staircases. Staircases are also smaller in scale toward the surface where the background gradients in temperature are greater (Figure 3.12). Where temperature gradients are strong, a smaller bin size is necessary for accurate identification. A more sophisticated classifier could vary the bin size used to classify staircases with the background gradients in temperature and salinity to compensate for this. This tendency reinforces the need to consider the sensitivity of classifiers to the vertical bin size.

Considering the total results from all of SG620's dives (Figure 3.13) it is clear that finer binning identifies more layers at all depths and of all thicknesses. This is particularly apparent in the upper parts of the pycnocline around 100-200 m. In addition to missing shallow layers, the 5 m binned profiles detect no steps below 500 m, where the temperature changes of the interfaces are smaller. The distribution of density ratio as shown in Figure 3.11 is robust to changes in bin size, with a strong peak of thick mixed layers centered around $R_\rho = 1.7$. However, the 5 m binned profiles detected no steps at $R_\rho > 2.5$. This may explain why early studies, with coarser vertical sampling resolution, did not detect any staircases at

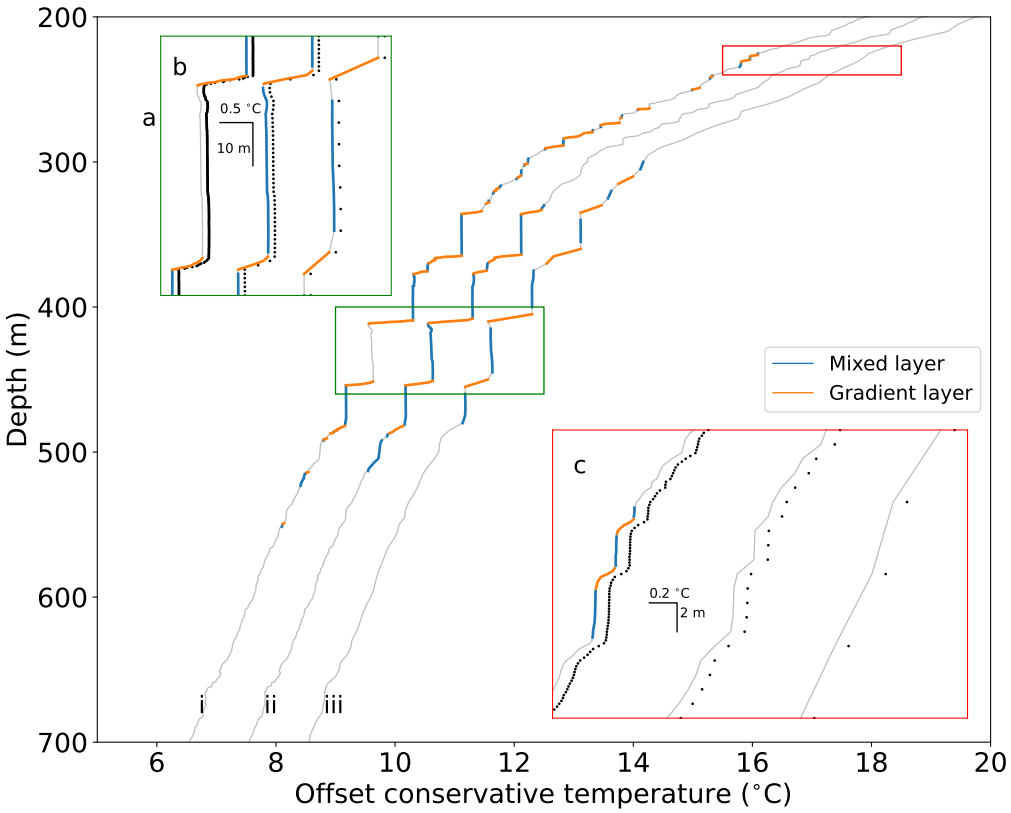

Figure 3.12: SG620 dive 20 fast-response thermistor temperature. Three profiles are the same data binned at 0.2 m, 1 m and 5 m respectively, then classified. b & c are detailed subsamples of the profiles, offset black dots mark the centers of each depth bin.

large values of R_ρ, or in the upper reaches of the pycnocline. This also imposes a limit on the structure detectable from Argo data, which has a minimum detection threshold of 2 dbar (VDB). On bandwidth limited platforms like Argo floats, this issue could be circumvented with on-board processing. Using recorded profiles of temperature and salinity at their maximum resolution, thermohaline staircases could be identified using an algorithm like VDB's algorithm and the location of steps transmitted over a satellite link. This would avoid the need to transmit the high resolution thermohaline profiles while identifying steps at a finer resolution than 2 dbar.

3.4.3 Limitations of automated classifiers

To our knowledge, this is only the second study to use an automated classifier to identify thermohaline staircases, and the first to use one on glider profiles. Early studies with relatively few observations classified staircases manually (Schmitt et al., 1987; Marmorino et al., 1987). Authors sometimes added further detail by classifying staircases as "clean " or "steppy" (Fer et al., 2010).

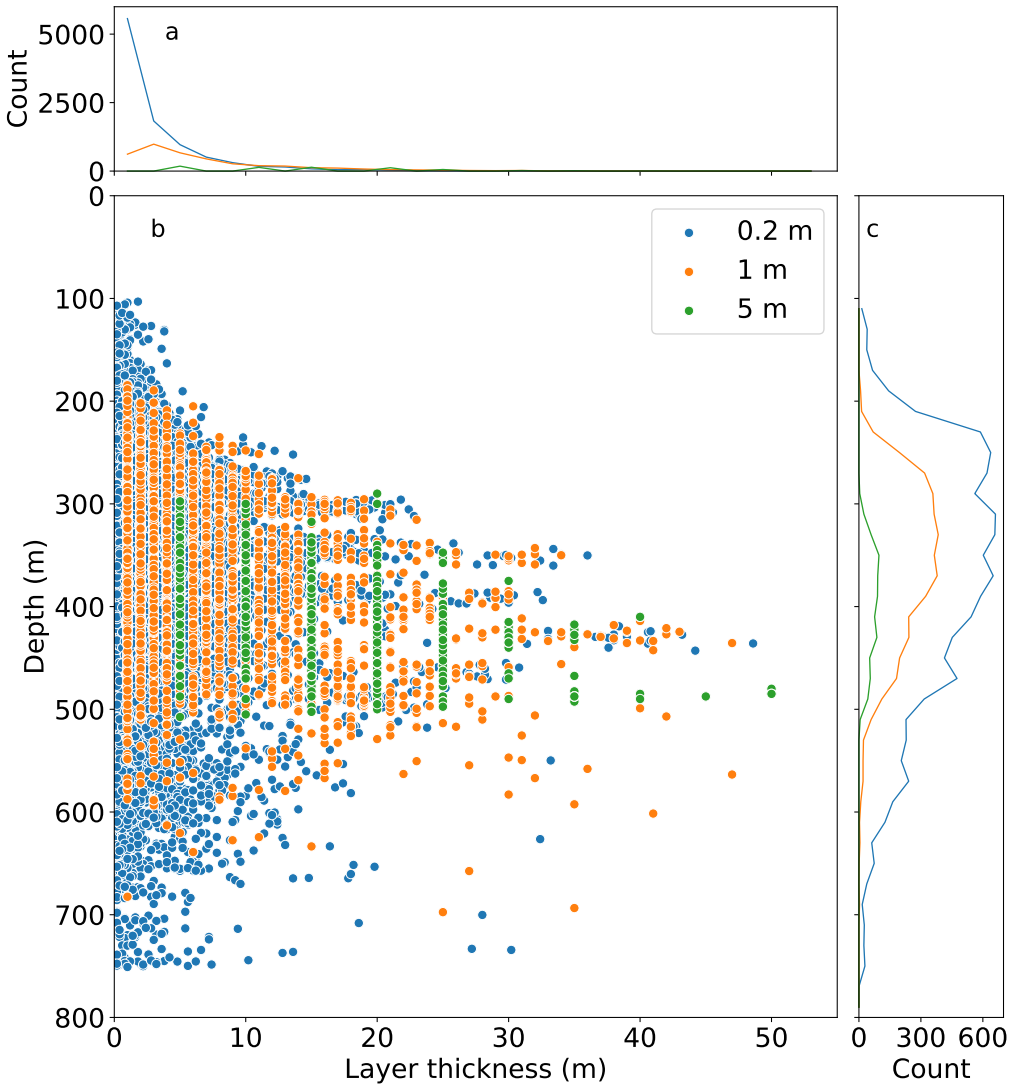

Figure 3.13: All mixed layers identified from SG620 fast-response thermistor data when binned at 0.2 m, 1 m and 5 m. Lines in a) and c) are binned total number of points in b) with bin widths of 2 m and 20 m respectively.

Though more recent work preliminarily identified staircases by threshold gradients e.g. Durante et al. (2019), this was followed by inspection and reclassification by a human operator, again using descriptive labels such as "steppy", "rough" and "slope". Automated classifiers can remove the subjective element from this process, identifying staircases from their physical properties alone in a way that is repeatable and consistent within and between datasets.

The detection of staircases is dependent on the algorithm design and a small number of key parameters, such as maximum allowable density gradient, density variability and thickness of mixed and gradient layers. VDB carried out sensitivity analysis on parameters including maximum mixed layer density gradients, temperature and salinity variability, and gradient layer thickness.

This analysis showed that VDB's algorithm is most sensitive to changes to the maximum mixed layer density gradient and mostly insensitive to other parameters. Smaller maximum density gradients allow only the sharpest, most clearly defined steps. Larger gradients also identify the less well defined rough steps. VDB did not perform sensitivity analysis on vertical bin size due to the limited nature of Argo profiles which are supplied at 1 dbar resolution. Analysis on the effect of vertical bin size, as described in Section 3.4.2, suggests that this is an important factor in staircase identification.

The results from our classifier are robust to changes in the key parameters, and relative differences within the dataset are preserved. However, parameter changes can affect classification of individual profiles. Figure 3.5 shows the result of three classifications of the same same Argo profile. The first profile is VDB's algorithm on default parameter settings, the second is our classifier using the same parameters, the third is our classifier with the maximum density gradient increased by 4 % and the step height ratio decreased by 10 %. In this example, three rough steps are rejected by our classifier using default parameters (ii), as the relatively thicker mixed layers exceed the density gradient criterion. By making critical parameters more strict in profile iii, we achieve a closer, but not exactly matching result to VDB's algorithm (Figure 3.5). The selection of these key parameters is currently a manual process, guided by previous studies that have established threshold values (Bryden et al., 2014; Timmermans et al., 2008). Once chosen however, key parameters are constant for the whole dataset and the classification of staircases is not altered by the user post-classification. We used the parameter set demonstrated in profile iii for this study.

Imperfect data also pose a problem for automated classifiers. In this study, we had to smooth out salinity spikes to prevent false negatives in the classifier (Figure 3.7). Small deviations in temperature and salinity that a human classifier would ignore can also cause steps to be rejected (e.g. Durante et al. 2019 Figure 3). The nine filtering steps in VDB's algorithm and our classifier prevent most false positives, such as the step like structures formed by thermohaline intrusions. However, some visually step like structures are rejected if they fall outside the parameter space (Figure 3.13b). At the other extreme, setting key parameters to large values can allow overly lax step classification. This problem is most apparent at greater depths. In the Mediterranean, where staircases extend below 1500 m, individual gradient layers have small magnitude changes in temperature and salinity. These small steps are harder to positively identify, particularly if there is instrument noise in the temperature and salinity profiles. Using VDB's default parameter values on a profile from the Mediterranean, our classifier combines two mixed layers around 1000 dbar (Figure 3.5 ii). Applying a 4 % decrease in maximum

permitted density gradient and a 10 % decrease in step height ratio correctly identifies these as two separate steps (Figure 3.5 iii). VDB restricted classification to 100-900 dbar, so the performance of VDB's algorithm at this depth is unknown. Future classifiers could resolve the issue of identifying steps of smaller magnitude in deeper water by using varying parameters, perhaps scaling the threshold values for step identification by the background gradients in temperature, salinity and density.

Automated classifiers for thermohaline staircases are in their infancy. We hope that the example created by VDB and built on by this manuscript can be further improved, and that other classifiers may be created to resolve issues raised in this section. We have made our classifier available on GitHub, with full development history, software tests, sample data and a demonstration notebook (Rollo, 2021a). Future work on thermohaline classifiers, and many other code intensive oceanographic projects, could benefit from the iterative, collaborative approach of open source software development enabled by platforms like this.

3.5 Summary

Building on the work of VDB we developed a classifier to detect thermohaline staircases. This improved classifier can operate on datasets at any regular vertical spacing. The classifier can also be used on datasets with suboptimal salinity data, such as profiles contaminated by salinity spikes, or salinity measured at lower spatial resolution e.g. when using a fast-response thermistor. We used this classifier to successfully identify two periods of strong thermohaline staircasing in the tropical North Atlantic. Our classifier is flexible, extensible and designed to be simple to use.

Our classifier could be applied to glider datasets across a range or environments. The classifier would be most beneficially applied to datasets from shelfs, shallow seas and other areas that are undersampled by Argo floats. The improved resolution of microstructure systems makes data from microstructure gliders particularly valuable for this analysis. This higher vertical resolution data shows evidence of small stepped staircases occupying areas with higher background temperature and salinity gradients. These small staircases may be underestimated in global studies, such as VBD, which are based on coraser resolution profiles.

Based on our observations of thermohaline staircases, we hypothesise that strong vertical gradients in temperature and salinity inhibit the formation of staircases in locations where the density ratio is favourable to their formation. Implementation of this result could improve model sub-grid parametrisation of

diapycnal mixing in regions such as the tropical North Atlantic and Mediterranean, where thermohaline staircases are widespread and long-lived.

Using fast-response thermistor data, combined with salinity observations, we were able to classify staircases at the sub metre scale. This is a promising demonstration of automated classification at smaller scales, which can be useful in areas such as the Arctic where small scale thermohaline staircases are known to form.

3.5.1 Code and data availability

Thermohaline classifier code is archived at Rollo (2021a). Glider data are held at the British Oceanographic Data Centre (Rollo, 2021b).

3.5.2 Author contribution

RAH, KJH and CR contributed to the design of the experiment and data collection. CR created the algorithm and produced the figures. CR prepared the manuscript with contributions from KJH and RAH.

The authors declare that they have no conflict of interest.

3.5.3 Acknowledgements

CR was supported by the Natural Environment Research Council and the Engineering and Physical Sciences Research Council, via the NEXUSS Centre of Doctoral Training in the Smart and Autonomous Observation of the Environment Grant NE/N012070/1. This project has received funding from the European Research Council (ERC) under the European Union's Horizon 2020 research and innovation programme (COMPASS, Grant agreement No. 741120). We thank the crew and scientists of the RV *Meteor* cruise M161 for assistance in the deployment and recovery of gliders, in particular Dariusz Baranowski for collection and processing of ship CTD data. Thanks to Gareth Lee and Marcos Cobas-Garcia for the preparation of the gliders, and the UEA glider group for piloting. We used the Python packages numpy (Harris et al., 2020) and pandas (McKinney, 2010) to create the classifier. We used matplotlib (Hunter, 2007), cartopy (Elson et al., 2020) and Jupyter (Kluyver et al., 2016) in the creation of figures.

4

ADCP Integration, Testing, and Trials

4.1 Introduction

This chapter presents the trials and tribulations of the ADCP equipped glider SG637 Omura. Table 4.2 outlines the chronology of Omura activities from early 2018 to summer 2020. Section 4.4 describes the physical integration of the ADCP. Sections 4.4.2 to 4.5 detail the series of bench tests, sea trials and scientific deployments undertaken by Omura to date. During this period, I spent a considerable amount of time testing the ADCP-glider integration and experimenting with different set ups. I have collected my experience and suggestions into a cookbook style instruction manual, intended for future users of Omura and similar systems. The cookbook has been archived online by Rollo (2020a) and included in this Chapter as Section 5. To make use of the ADCP glider system, I have written scripts to extract, process and plot data from Omura. These scripts have been archived by Rollo (2020b).

4.2 ADCPS on gliders

In recent years, several groups have worked to integrate ADCPs into AUVs. A major driver in this work has been the issue of establishing location underwater (Medagoda et al., 2010; Stanway, 2010). Using an ADCP or DVL to measure the velocity of water relative to the platform yields the velocity of the platform through the water. Integrating this velocity over time, combined with an accurate compass, the platform can track its own progress without the need to surface and obtain a GPS fix. This approach does not account for currents. This ability is key for the operation of autonomous subsurface vehicles where regular surfacing is not possible, such as operation under ice (McPhail et al., 2019; Phillips et al., 2020).

While ADCPs offer obvious benefits to AUVs, there are several challenges that have impeded their adoption. Early generations of ADCPs were bulky, power hungry systems that were only suitable for vessel integration. More recent models are small and energy efficient enough to be usable on AUVs, using as little as half a Watt (Nortek Group, 2017a). To calculate the relative velocity of the platform, accurate attitude (the platform's pitch and roll) and heading data must be recorded at high temporal resolution. Platforms such as the Seaglider use a single threaded processor to control the flight, sensors and all on-board processing (IRobot, 2012). This limits the frequency at which attitude data can be recorded without affecting other sensors. This is an issue for sensors, like the ADCP, that require frequent attitude measurements to correctly process the data that they collect. To circumvent this limitation, modern ADCPs like the Nortek acoustic Doppler dual current profiler (AD2CP) record attitude with an internal sensor (Nortek Group, 2017a).

As a subset of AUVs, gliders present both opportunities and challenges for ADCP integration. One of the advantages of gliders as an ocean observation platform is their near silent flight. When not operating the buoyancy pump or pitch/roll motors, gliders are almost noiseless. This has made them attractive platforms for other vibration sensitive sensor payloads, such as hydrophones (Baumgartner and Fratantoni, 2008; Cauchy et al., 2018) and microstructure profilers (Fer et al., 2014; Palmer et al., 2015). Gliders' slow speed through the water and aerodynamic profile results in very little vibration that can contaminate ADCP data. A major challenge of glider ADCP integrations is the power draw of an ADCP. A typical glider mission runs at half a Watt; most of this power is consumed by the pump that drives the glider's motion (Eriksen et al., 2001). Even the newest generation of low power ADCPs are similar in power draw to the pump e.g. the Nortek AD2CP draws half a Watt when active (Nortek Group, 2017a). The endurance of gliders is far greater than that of propeller driven AUVs; missions typically last months rather than days (Testor et al., 2019). The dive profile of a glider also lends itself well to observations of ocean currents. A glider can collect ADCP velocity profiles from the uppermost 1000 m of the ocean every few hours. Direct observation of ocean currents, as opposed to inference through geostophic shear, enables ADCP gliders to estimate ocean velocites at small scales and in ageostrophic conditions. Using gliders enables low cost continuos monitoring of environment. This is particularly useful in shelf breaks, such as that detailed in Chapter 2, where alongshore flows change rapidly over several months, and ageostrophic currents can impact transports. Over the last decade, a range of ADCPs have been integrated into various gliders (Table 4.1).

A small number of groups, often led by oceanographers based at Scripps California and the University of Washington (UW), have undertaken numerous technical and science missions with ADCP gliders. Several different ADCP units have been incorporated into each of the four major glider platforms. These include a Slocum with a Teledyne RD Instruments (TRDI) 4 beam 614.4 kHz instrument (Ordonez et al., 2012); a 3 beam 750 kHz Sontek sensor on numerous Spray glider missions (Davis, 2010; Todd et al., 2011b; Johnston et al., 2013); and a 4 beam 1 MHz Nortek AD2CP mounted on the UW Seaglider (Jonker et al., 2019). These different set ups have real effects on the data collected through several parameters. The operating frequency affects the range of the beams, and pings per ensemble vary between sensors affecting reliability. Some transducer set ups preclude data gathering on either the upward or downward part of the dive, such as the 3 beam Sontek used on most spray glider missions. Regardless of the equipment used however, the principles and methods of data processing remain the same.

Glider	ADCP	Location	Reference
Slocum	TRDI 614.4 kHz	Oregon shelf	Ordonez et al. (2012)
Spray	Sontek Argonaut 750 kHz	California Current System	Todd et al. (2011b)
UW Seaglider	Nortek AD2CP 1 MHz upward looking	Prudhoe Bay Alaska	Jonker et al. (2019)
Alseamar Seaexplorer	Nortek AD2CP 1 MHz upward looking	Northwest Mediterranean	de Fommervault et al. (2019)
Kongsberg Seaglider	Nortek AD2CP 1 MHz downward looking	Various locations	This thesis

Table 4.1: Notable glider ADCP integrations covering the four major glider platforms

There is also the contrast between upward looking ADCPs such as that mounted on the Slocum (Ellis et al., 2015) and Seaexplorer (de Fommervault et al., 2019) and the downward looking sensors on the iRObot Seaglider (Rusello et al., 2012) and Spray (Todd et al., 2017). Downward looking sensors have the advantage of bottom tracking in shallow surveys (Fong and Monismith, 2004). However inclusion of this data in conjunction with the shear method has yielded large errors (Fong and Monismith, 2004; Thurnherr et al., 2015). Upward looking sensors collect more data from the oceans surface layer, though these data bins are often omitted from analysis due to lobe effects and surface waves (Ellis et al., 2015).

4.3 SG637 Omura

The work of this thesis is based on the integration of a Nortek 1 MHz AD2CP onto a Konsgberg M1 Seaglider SG637 Omura (Figure 4.1). Omura was funded through NERC Capital Equipment call to large projects, reference CC16_012. This proposal was written by Karen J. Heywood, Adrian Matthews and Rob A. Hall as part of the BoBBLE project NE/L013827/1. Although it was awarded to UEA, Omura was assigned to MARS to operate. Prior to this thesis, no trials or deployments had been conducted for Omura since she was delivered. The work completed by Kongsberg before delivering Omura consisted of physical integration of the ADCP and creation of a communications protocol between the glider and ADCP. As far as I am aware, Omura is a one-off system.

The Seaglider was developed in Seattle as a joint project between UW School of

Date	Event	Location	Section
Feb 2018	Cancelled sea trials	Canary Islands	4.4.2
Jul 2018	Bench tests at UEA	UEA	4.4.2
Aug 2018	Sea trials round 1	Oban	4.4.3
Nov 2018	Sea trials round 2	Oban	4.4.4
Apr 2019	Scotia deployment	Faroe-Shetland Channel	4.4.5
Jan 2020	EUREC^{4}A deployment	East of Barbados	4.5
Jul 2020	Bench tests & firmware update	UEA	4.5.5

Table 4.2: Timeline of Omura activities

Oceanography and UW Applied Physics Lab, beginning in 1997. The first field trials were reported in 2001 (Eriksen et al., 2001). The Seaglider was licensed to iRobot in 2008 to manufacture Seagliders for the US navy (Guizzo, 2008). This made the Seaglider available for purchase and use by scientists outside of UW. The commercialization rights to the Seaglider were transferred to the Norwigian martime company Kongsberg in 2013 (Kongsberg, 2013). Seaglider was subsequently transferred to the Kongsberg subsidiary Hydroid Inc. in 2019 (Kierstead, 2019). Four months later, Hydroid was itself purchased by the US military shipbuilder Huntington Ingalls Industries (Brenton, 2020). Huntington Ingalls Industries retain ownership of Seaglider at time of writing.

SG637 Omura was constructed by Kongsberg in 2016, software changes and firmware updates detailed in Chapter 4 were supplied by Kongsberg, Hydroid and Huntington Ingalls Industries. A parallel effort to integrate the Nortek AD2CP into the Seaglider has been pursued by UW, who continue to produce the Seaglider in-house for their own use. The UW Seaglider-AD2CP integration is independent of this work. UW decided to mount the AD2CP upward facing and have produced their own firmware to support it (Jonker et al., 2019). At time of writing, the conference paper by Jonker et al. is the only published article relating to the UW AD2CP Seaglider.

4.4 Overview of the ADCP integration and trials

4.4.1 ADCP geometry and glider attitude

The Nortek 1 MHz acoustic Doppler dual current profiler (AD2CP) integrated into the Kongsberg Seaglider M1 is a non-standard broadband 4 head ADCP. The AD2CP is integrated into the rear payload bay of the glider and is

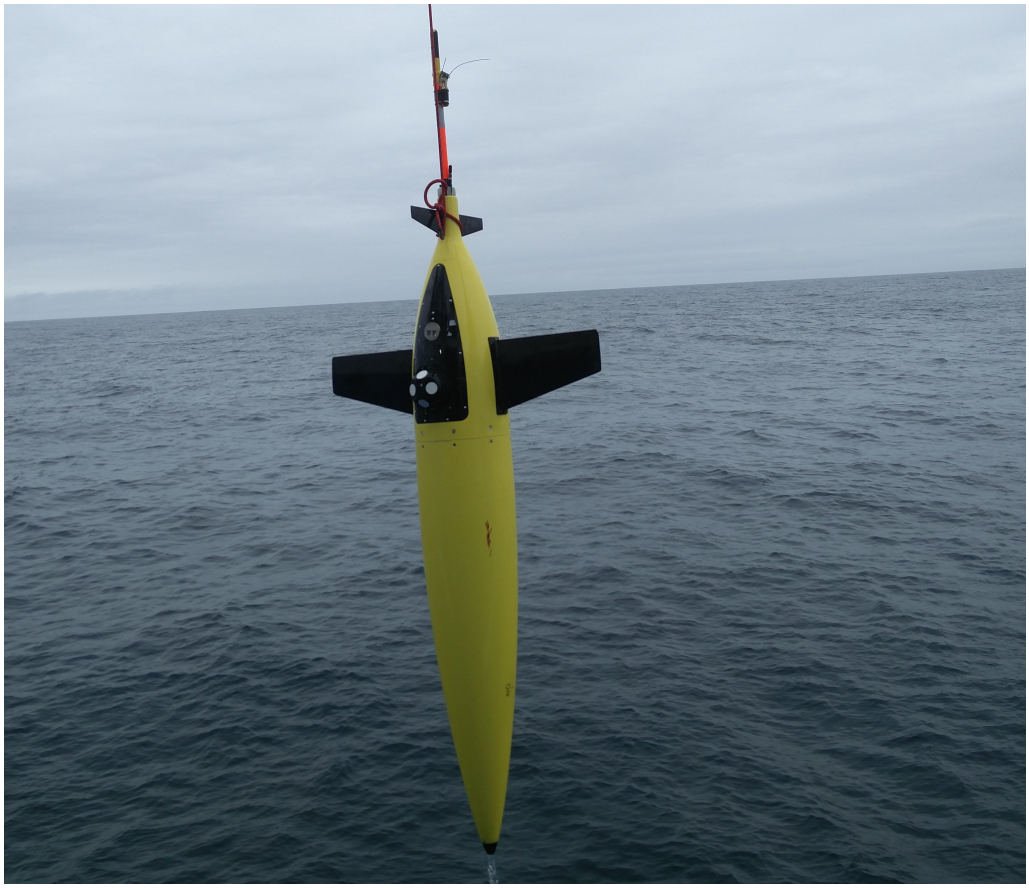

Figure 4.1: Photograph of SG637 Omura during recovery from the Faroe-Shetland Channel, April 2019. This photograph shows the lower side of Omura with the AD2CP and a SeaOwl oil in water sensor visible.

connected to the glider pupae by a wet pluggable Subsea connector (Figure 4.2). The AD2CP produces a broadband chirp, centered around 1 MHz. Compared with a narrowband chirp, a broadband chirp enables the use of smaller sampling bins and increases accuracy of the instrument, at the cost of a smaller range in low-scattering environments (Ordonez et al., 2012). A 4 head setup enables observations during both descent and ascent phases of a glider dive. This design overcomes the issue of some earlier ADCP gliders such as the Sontek 750 kHz ADCP Spray integration, which could only record data during the ascent of a glider dive (Davis, 2010). To enable observations during descent and ascent, the AD2CP uses a "Janus" geometry. The fore and aft transducers of the ADCP are offset from the vertical by 47.5 °, the port and starboard transducers are offset by 25 ° (Figure 4.3). These angles are referred to as ϑ_{fa}: the angle of the fore and aft beams from the vertical and ϑ_{ps}: the angle of the port and starboard beams from the vertical. This varied geometry enables observations of velocity during both descent and ascent when the glider's attitude is optimal: pitch of 17.4°and roll of 0°. For a pitch angle of ϕ_{pitch} (positive down) and roll

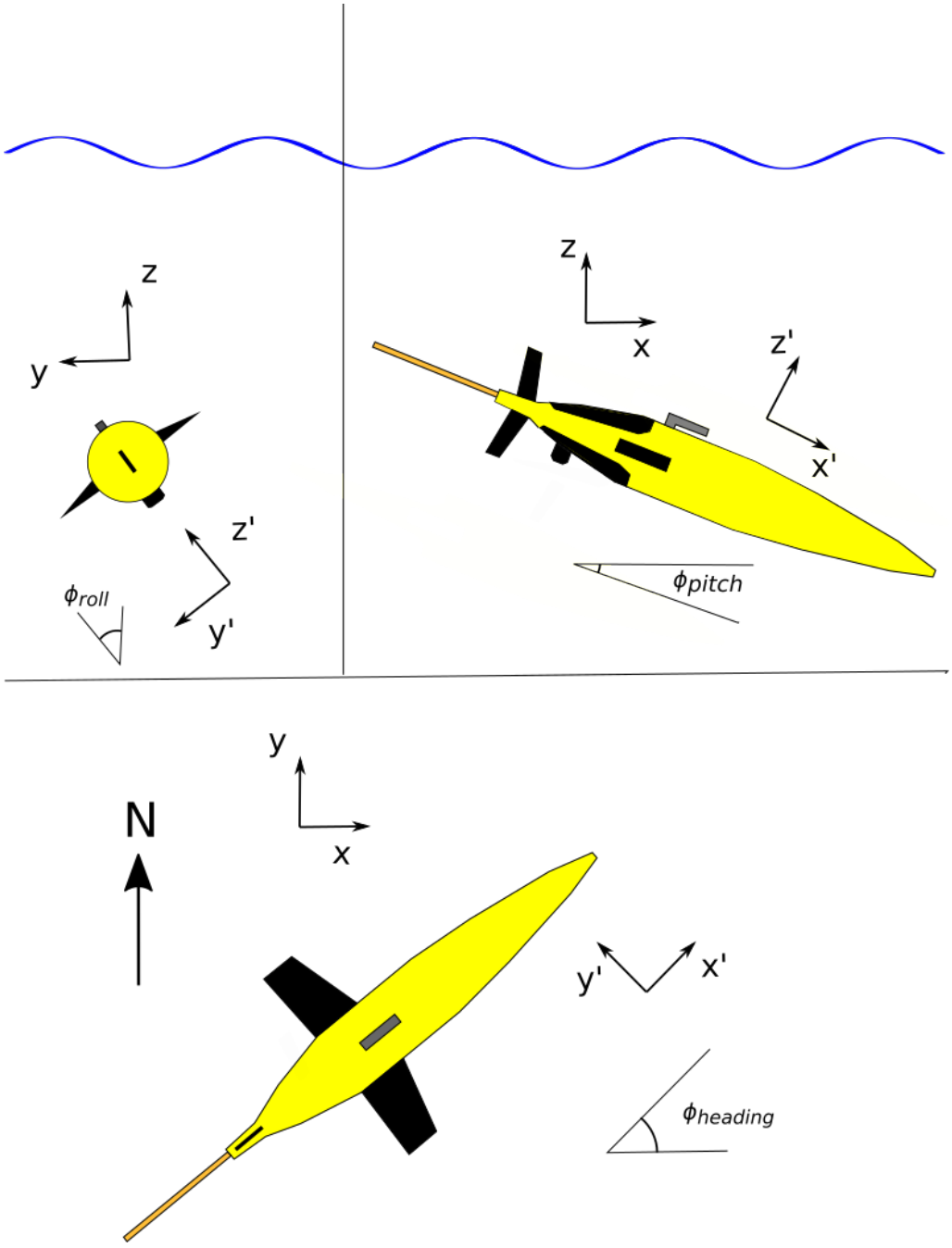

Figure 4.2: The AD2CP is located in the hatch cover on the underside of the glider, visible as a protruding bevelled cylinder just fore of the tail. The two coordinate systems X (earth) and X' (glider) are shown. The angles between these coordinate systems are pitch, roll and heading as shown.

of ϕ_{roll} (positive roll to starboard), a scatterer at distance l from transducer number x as labelled in Figure 4.3 (1: forward, 2: port, 3: aft, 4: starboard), the vertical distance from the ADCP z_x for each beam is shown in Equation set 4.1.

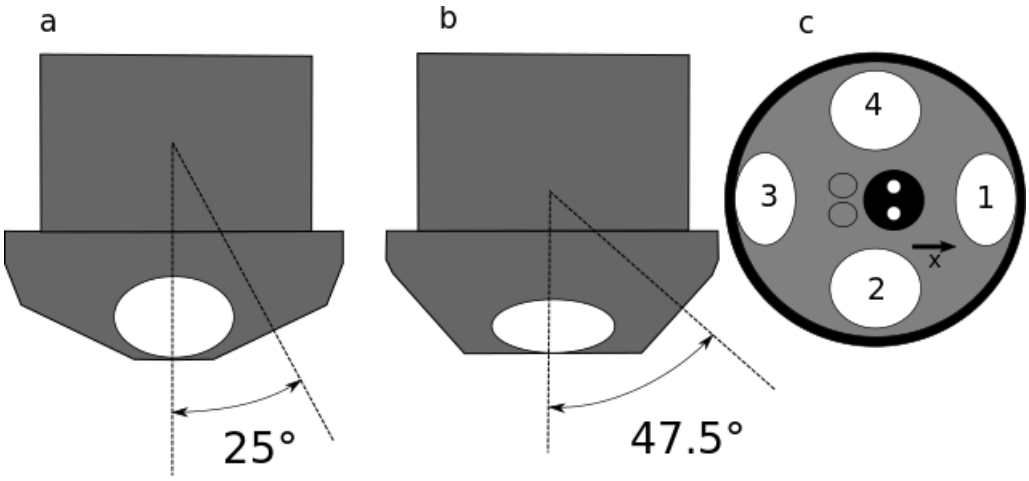

Figure 4.3: Schematics of the AD2CP transducers: a) front view (angle ϑ_{ps}) b) side view (angle ϑ_{fa}), c) bottom view with transducer heads numbered. X arrow in c) points toward the glider nose.

$$\begin{aligned} z_1 &= l\cos(\vartheta_{fa} - \phi_{pitch})\cos(\phi_{roll}) \\ z_2 &= l\cos(\vartheta_{ps} - \phi_{roll})\cos(\phi_{pitch}) \\ z_3 &= l\cos(\vartheta_{fa} + \phi_{pitch})\cos(\phi_{roll}) \\ z_4 &= l\cos(\vartheta_{ps} + \phi_{roll})\cos(\phi_{pitch}) \end{aligned} \tag{4.1}$$

The angle of these beams from the vertical θ_x is $\arccos(z_x/l)$, from this we formulate Equation set 4.2.

$$\begin{aligned} \theta_1 &= \arccos(\cos(\vartheta_{fa} - \phi_{pitch})\cos(\phi_{roll})) \\ \theta_2 &= \arccos(\cos(\vartheta_{ps} - \phi_{roll})\cos(\phi_{pitch})) \\ \theta_3 &= \arccos(\cos(\vartheta_{fa} + \phi_{pitch})\cos(\phi_{roll})) \\ \theta_4 &= \arccos(\cos(\vartheta_{ps} + \phi_{roll})\cos(\phi_{pitch})) \end{aligned} \tag{4.2}$$

When the glider is diving with $\phi_{pitch} = 17.4\ ^\circ$ and $\phi_{roll} = 0\ ^\circ$, $\theta_1 \approx \theta_2 \approx \theta_4 \approx 30.1^\circ$ (Equation set 4.2). The fore, port and starboard beams are arranged approximately in an equilateral triangle around the vertical, optimising the beam spread. All three beams are angled at 30.1° from the vertical, so they observe scatterers at the same depth level. This scenario is depicted in Figure 4.4. Having all beams sample at the same depth is essential for reconstructing vertical shear profiles of the water column (Todd et al., 2017). $\theta_3 = 64.9$, the aft facing beam is turned off during the dive. Correspondingly, when climbing with $\phi_{pitch} = -17.4$, $\phi_{roll} = 0$, $\theta_2 \approx \theta_3 \approx \theta_4 \approx 30.1^\circ$, $\theta_1 = 64.9$. The aft, port and starboard beams

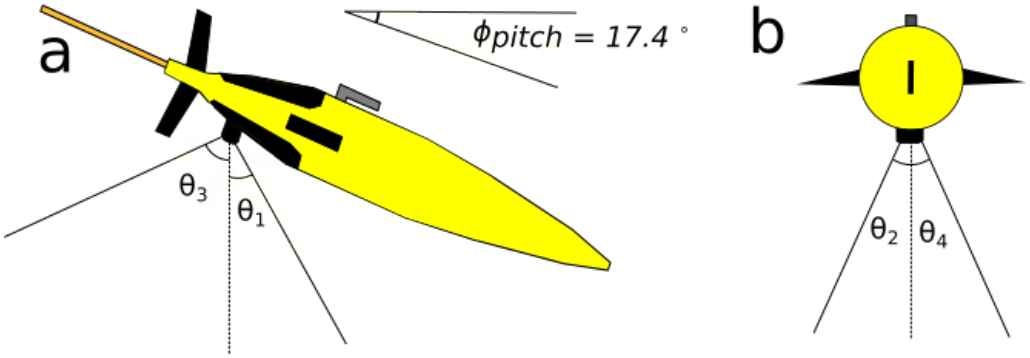

Figure 4.4: The angles of the four ADCP beams when the glider is diving with a pitch of 17.4 ° and roll of 0 °. a) view from port. b) view from tail. The angles of the fore (θ_1), port (θ_2) and starboard (θ_4) beams from the vertical are 30.1 °.

are symmetrical around vertical and the forward facing beam is turned off.

The fore and aft beams are turned off during ascent and descent respectively to reduce energy consumption by the AD2CP. The AD2CP, like most glider sensors, is powered from the glider's primary cells. Reducing power usage of the AD2CP increases the endurance of the AD2CP glider. The AD2CP lacks the high sampling frequency compass/tilt sensor used by some mooring mounted ADCPs to actively change time gates in response to changing sensor pitch and roll. This system is in use on buoy mounted ADCPs Shumuk et al. (2018). To my knowledge, there are no ADCP-glider integrations with the capability to re-gate in response to pitch and roll. This capability would incur additional costs and reduce mission endurance. However, the improved data quality and reduced piloting/trim constraints could make it worthwile

Gliders rarely dive and climb with perfect pitch and roll. The pitch must be adjusted to vary the glider's forward speed and regular rolling is essential to maintain course (Eriksen et al., 2001). Figure 4.5 shows two dive plots: a shallow poorly trimmed dive and a deep, well trimmed dive. In the shallow dive, the glider's pitch (bright green line) is highly variable and near 30 degrees for much of the dive. The roll (solid yellow line) is also variable, with the glider rolling during half of the whole dive. When well trimmed the pitch is near 20 degrees and the glider is rolled flat during most of the dive, as can be seen in the lower panel. The process of trimming is iterative. On each dive, the flight of the glider is reported and pilots adjust several parameters to improve it. The key parameters are the central values of buoyancy, pitch and roll and the sensitivity with which the glider changes these values. A well trimmed glider will dive symmetrically, with approximately equally pitched and timed descent and ascent. Good trimming enables the glider to cover more distance with less wasted energy, perform fewer rolls to maintain course and maximises the useful window of data collection for

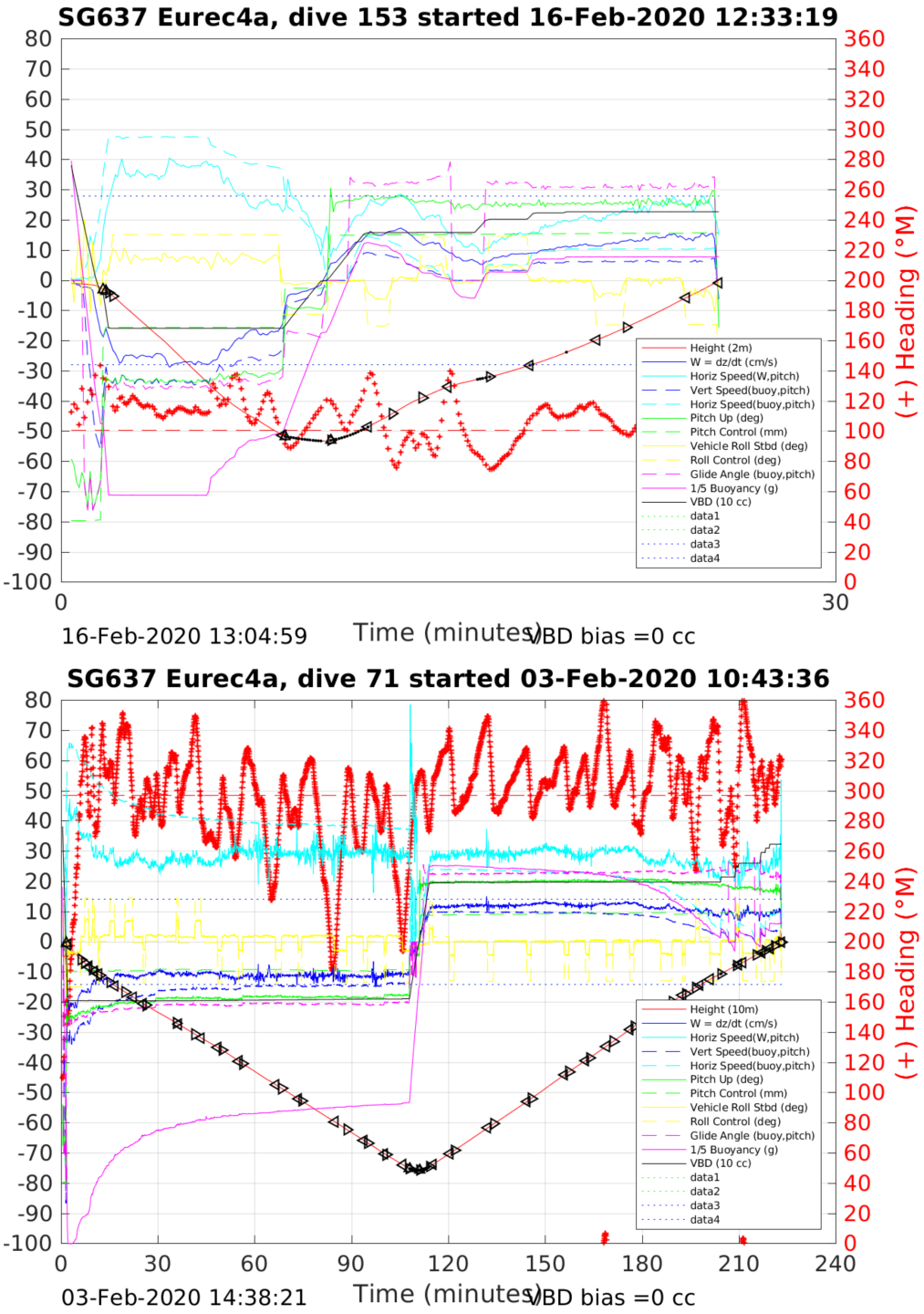

Figure 4.5: Diveplots from SG637. Top plot is a poorly trimmed shallow dive to 55 m. Bottom plot is a well trimmed deep dive to 750 m (y axis is multiples of 10 m).

pitch and roll sensitive sensors such as ADCPs.

Figure 4.6 shows the effect of deviating from the ideal pitch and roll. As ϕ_{pitch} and ϕ_{roll} move further from 17.4 and 0, the three θ values of the active transducers diverge, as do the values of z. z is the vertical distance between the transducer and the reflector. This divergence of z values represents the three beams measuring velocity from reflectors at different depths. The AD2CP does not correct for this divergence. This prevents accurate estimation of velocity shear. The maximum difference between values of z for the three active beams at a set distance from the glider is referred to as "beam miss". The glider must be piloted within a small parameter space if the active beams are to reflect off scatterers in the same vertical bin. As $z \propto l$, the parameter space of acceptable pitch and roll increases in direct proportion to the increase in bin size. For a bin size of 0.2 m, the operational minimum of the AD2CP, the glider must be kept within $\pm$ 0.7 $^\circ$ of roll $\pm$ 0.7 $^\circ$ pitch to keep beams sampling within the same vertical bin 15 m from the ADCP. For the maximum bin size of 2.0 m, this tolerance increases to $\pm$ 7.5 $^\circ$ roll. Pitch sensitivity is notably asymmetric, the ADCP can sample well if the flight steepens by up to 9 $^\circ$ but can only tolerate shoaling of the dive slope of 4 $^\circ$ (Figure 4.6). This is due to bin depth, and consequently beam miss, being a function of the cosine of pitch (Eq 4.1). At small values of pitch, cos(pitch) changes rapidly, as pitch increases, the rate of cos(pitch) change decreases due to the shape of the cosine function.

4.4.2 Arrival and bench tests

Omura was initially shipped to Plataforma Oceánica de Canarias (PLOCAN), Gran Canaria, for sea trials in February 2018. These trials were cancelled due to high winds. On return to the UK, Omura was delivered to UEA for testing.

Omura did not have any documentation for the AD2CP on arrival. The first challenge was to connect to the AD2CP and conduct bench tests. By trial and error, I connected a laptop to the AD2CP via the supplied Ethernet to Subsea cable and tested different settings of the AD2CP.

I tested the AD2CP on the bench and then in the glider ballasting tank to examine signal returns when operating in water. Due to the nature of the sensor, only limited tests can be performed in a tank. The reflecting sound waves from walls less than 2 m from the AD2CP transducers preclude the measurement of any meaningful relative velocities. I was, however, able to verify that the transducers all reported similar signal strength returns when firing in the tank (Figure 4.7).

The data from the glider AD2CP could not be read correctly by Nortek's display software, as the software expects 4 beams symmetrically arranged around the

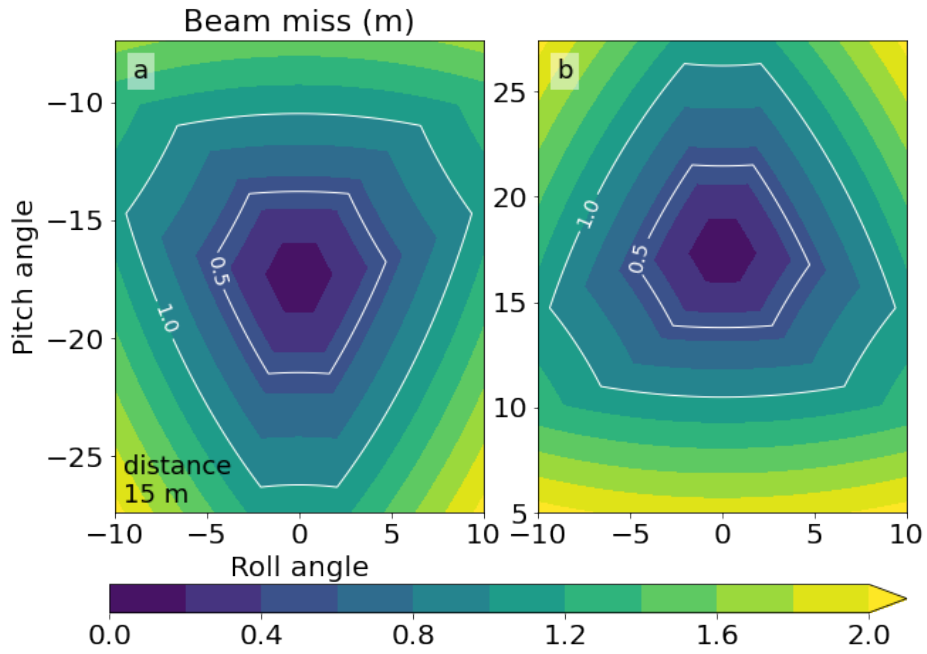

Figure 4.6: Inter beam vertical miss sampling over a range of glider pitch and roll values. The value plotted is the maximum vertical distance between reflectors sampled by each of the three active beams at a distance of 15 m from the glider. Black lines mark the 0.5 and 1.0 m contours.

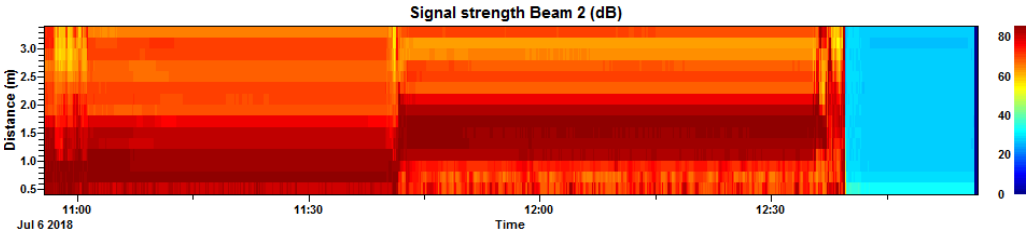

Figure 4.7: Signal strength of AD2CP beam 2 in dB during a tank test. The glider was pitched nose down until 11:40, then pitched nose up. The glider was removed from the water at 12:40, the ADCP continued recording.

vertical, not the three beams used by the glider AD2CP. I wrote scripts to take the Nortek generated netCDF files, extract the data and generate plots for quality control (Rollo, 2020b).

After a series of tests in the tank, we had confirmed that the AD2CP recorded data successfully and that the transducers were unlikely to be damaged. The next step was to trial Omura in the ocean, where the glider-AD2CP integration could be tested and data recorded from the full 30 m advertised range of the AD2CP.

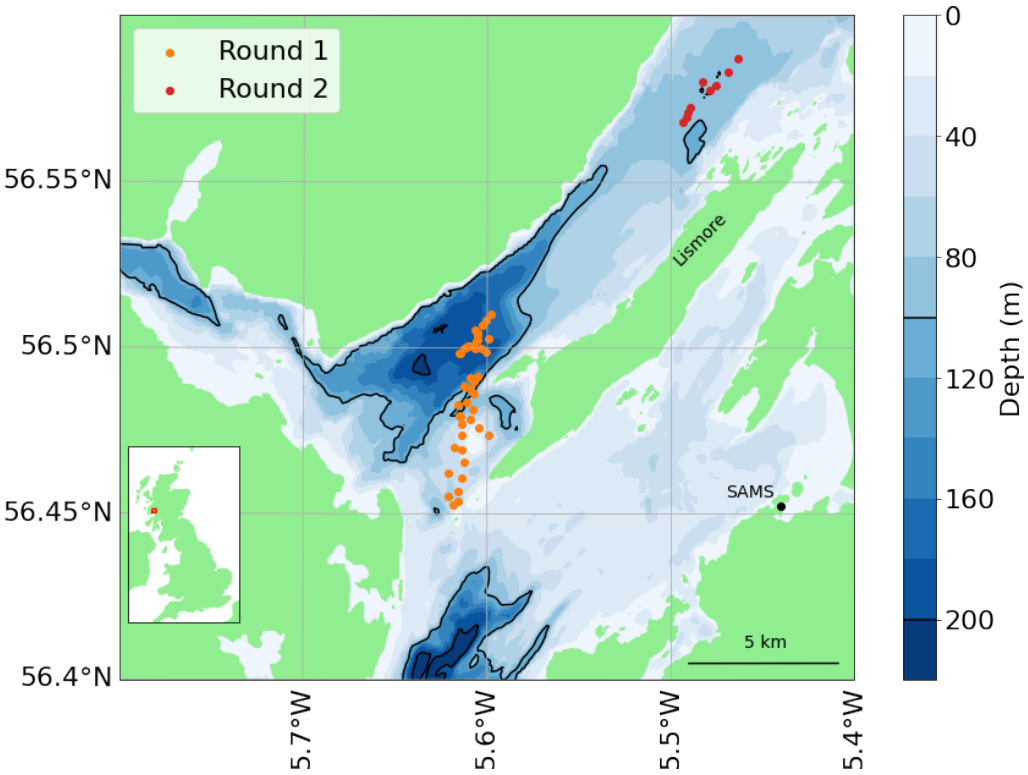

Figure 4.8: Bathymetric map of Loch Linnhe, west Scotland. Black lines mark 100 and 200 m depth contours. Bathymetry from the EMODnet Bathymetry Consortium (2018). Round 1 and round 2 refer to the two sets of trials of Omura. Dots are surfacings of the glider. Isle of Lismore and Scottish Association for Marine Science (SAMS) labelled. Red box in inset figure marks extent of map.

4.4.3 First Oban sea trials

In summer 2018, Omura was taken to Loch Linnhe near Oban, Scotland, for sea trials. Loch Linnhe was chosen for its 200 m water depth and proximity to the Scottish Association for Marine Science (SAMS) glider facility (Figure 4.8).

In preparation for sea trials, I modelled how the attitude of the glider would affect recorded AD2CP data, as described in Section 4.4.1. The principal consideration is keeping within the envelope for ideal data collection as shown in Figure 4.6. I chose to use the maximum bin size of 2 m to enable as broad a parameter space as possible. The AD2CP does not dynamically re-map bins by changing time gating in response to varying attitude, as some other ADCPs do (Shumuk et al., 2018). For this reason, the only way to ensure that all three beams sample water from the same depth bin is to control the glider attitude.

The flight control of Seagliders does not allow the pilot to specify a pitch (Seaglider, 2016a). This would be technically possible, but the manufacturer is not willing to change the operation mode to enable fixed pitch operation. Instead, the pilot must indirectly influence the glider to achieve the desired

pitch and roll as follows:

1. Trim glider in the usual way to achieve correct buoyancy, centred roll and pitch and symmetrical dives.
2. Adjust the pitch angle as close to the optimal angle of 17.4°as practically possible. 14-22°pitch from the vertical is good enough when using a 2m bin (Figure 4.6), as it keeps beam miss below 1 m, so bin remapping is not necessary. This is achieved by adjusting $D_TGT and $T_DIVE to encourage the glider into a steeper or shallower dive.
3. If the dive angle is too steep for large parts of the dive, reduce $GLIDE_SLOPE. This is the maximum glide angle in degrees. If the dive slope is too shallow, decrease $T_DIVE. There is no way to directly set a minimum glide angle.
4. Tighten the roll control to keep the glider within ± 2 degrees roll if possible, but ± 4 is sufficient. This can be achieved by decreasing $ROLL_DEG from its starting value of 40. If the glider is unable to meet the waypoints, increase $ROLL_DEG. Occasional rolls to stay on course are fine, as long as glider is within the parameter space of Figure 4.6 during 80 % of the dive.
5. Once the glider is navigating successfully, the time period between guidance and control phases can be increased e.g. from 60 to 180 seconds. This will decrease the proportion of time that the glider is changing attitude to stay on course.

The aim of these steps is to keep the glider within the ideal attitude envelope. The example dive plots in Figure 4.5 show the effect that following these steps has on the dive shape. Figure 4.6 shows how far the beams will vertically deviate from the bin depth with varying roll and pitch on descent (a) and ascent (b). The aim is to keep within the 0.5 m line if possible. Falling outside the 1.0 m line, the data must be discarded as the beams will sample different bins. This limit is half of the bin size. There is an inevitable tension between keeping the glider within the envelope of small beam miss to ensure the beams of the ADCP sample reflectors at the same depth, and allowing the glider to vary its pitch and roll to navigate. This is particularly difficult in shallow, tidal areas such as Loch Linnhe, where gliders struggle to keep station.

Omura was prepared, tested and sent on several sim dives the day before deployment. Sim dives are simulated dives where the glider runs through all the processes of a dive: pump, pitch, roll, sample from sensors, make satellite phone calls etc., while on dry land. It is the most comprehensive test that can be performed short of putting the glider in the water. Omura was then deployed in Loch Linnhe over the deepest section of the loch, NW of Lismore (Figure 4.8,

orange dots). Omura was left out overnight, on a transect through the deep trough at the south-western end of the loch . Strong currents at the mouth of the loch advected Omura over a shallow rise, reducing to water depth to less than 25 m and preventing Omura from navigating. Fortunately, Omura was successfully recovered without incident the following morning. On inspection of the memory card, the AD2CP had recorded no data.

After tests, sim dives and consultation with the manufactures, the source of this error was tracked to the glider firmware. The glider had been sending an incorrect command to the AD2CP to start recording. The AD2CP powered on and displayed the customary blue light, so this issue was not noticed when deploying Omura. The issue was subsequently fixed by a patch from Kongsberg. I applied this patch, upgrading the firmware from 66.11 ALBACORE to 66.12 DORADO in September 2018.

4.4.4 Second Oban sea trials

To test the system after the firmware upgrade, we sent Omura back to Loch Linnhe in November 2018. We decided to run a 3.5 km transect through the northeastern part of the loch, to avoid the strong currents that imperilled the first trials. The plan was to send Omura along a track in 90 - 100 m deep water off the northern tip of Lismore (Figure 4.8, red dots). This water depth is not ideal for glider operations, but it is sufficient for a short period of stable flight, suitable for ADCP testing. A transect between two waypoints, rather than a virtual mooring at a single waypoint, results in dives with a shallower dive slope, as desired by the AD2CP ideal glider flight model. A glider diving at an angle of 17.4 degrees over 100 m bathymetry will complete approximately 6 dives over a 3.5 km transect.

Due to the shallow water, testing opportunities were limited. However, Omura successfully recorded ADCP data for the first time. Results were promising, with high ping correlation and return amplitude out to 20 m beneath the glider (Figure 4.9). Over the 14 profiles recorded during the deployment, beam miss decreased. This shows as the dots on Figure 4.9 approaching the y axis. This is a positive result, indicating that trimming by the pilots following the steps in Section 4.4.3 improved glider flight. The correlation within ping ensemble displayed in this plot is also promising. Though the ADCP's advertised maximum range is 30 m, ping correlation fell to less than 50 % around 15 - 20 m from the glider. The glider collected an ADCP ensemble every 15 seconds. With a vertical speed of 0.1 m s^{-1} this results in an ADCP profile every 1.5 m vertically. If each ADCP profile has good correlation out to 15 m, we have a 90 % overlap between profiles. At 2 m bin diameter, each depth bin will have approximately 5 independent estimates of

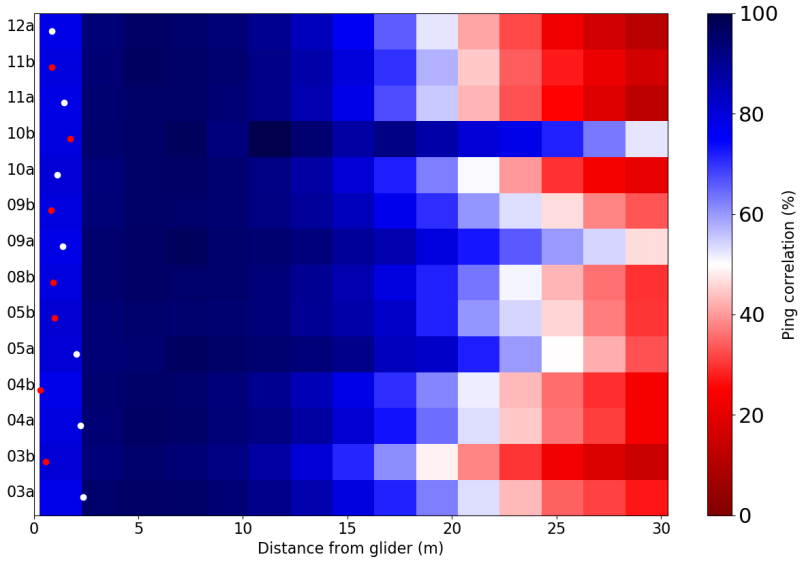

Figure 4.9: Average correlation per bin per dive. Y axis marks dive phases a descent, b ascent. Dots are the beam miss as plotted in Figure 4.6, white on descent, red on ascent.

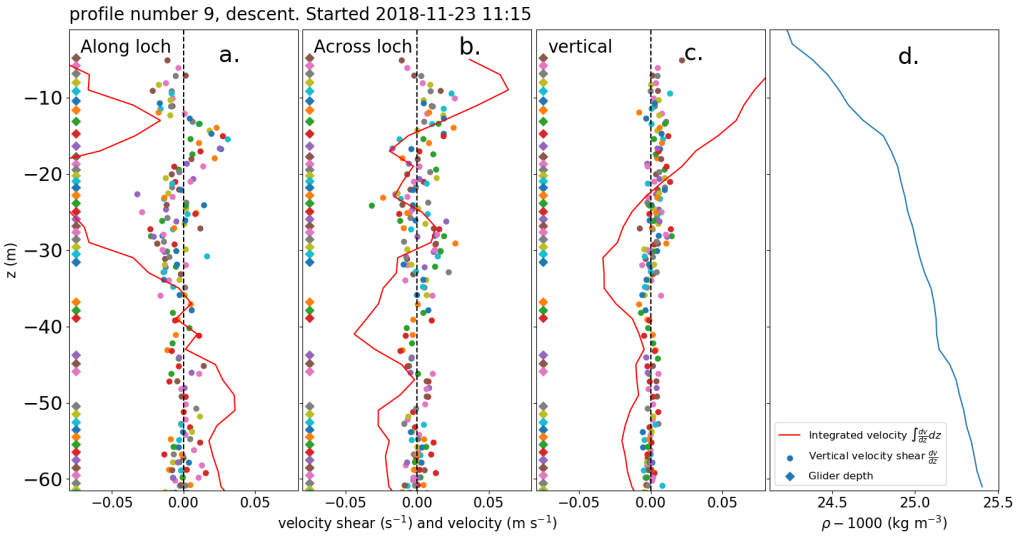

Figure 4.10: a-c) Vertical shear of velocity and velocity profiles in along loch, across loch and vertical directions. Each dot is an estimate of vertical velocity shear, dots of the same colour are taken from the same ensemble. Red line is the velocity profile calculated using the shear method. d) Potential density profile.

velocity shear.

I inspected the vertical shear of velocities, rotated to align with the long axis of the loch (Figure 4.10). A potential density profile is plotted in Figure 4.10 d. Initial results suggested increased current shear in along loch velocities around the base

of the pycnocline (Figure 4.10). This was a promising result, as the interface between less dense surface waters and more dense underlying water would be expected to have large velocity shear, though we had no in-situ data available for comparison. However, the glider was recording using the incorrect beams. When descending it was turning off the forward facing beam and when ascending it turned off the aft facing beam. This would not be discovered until after the EUREC^{4}A mission described in Section 4.5.3. As a consequence, the data in Figure 4.10 are improperly processed and do not represent the true velocity shear in the loch.

The successful trials increased our confidence in the ADCP glider. We planned a scientific deployment at the first available opportunity.

4.4.5 Faroe-Shetland Channel Deployment

After the trials in Loch Linnhe, we planned a full scientific deployment in the Faroe Shetland Channel (FSC) in Spring 2019. We would work from the Marine Scotland Science vessel RV *Scotia* during a regular mooring turnaround cruise. We planned to deploy over an ADCP mooring with a pressure inverted echo sounder (PIES) (Figure 4.11). The three data sources would enable independent estimates velocity shear. The FSC was chosen as a deployment site partly due to its deep pycnocline and depth varying flows (Turrell et al., 1999). This makes it an attractive site to test an ADCP glider, as large scale velocity shear structures should be relatively easy to observe. Conducting an ADCP-glider deployment with a collocated moored ADCP is a common method of validating ADCP-glider data (Ellis et al., 2015). The plan was:

1. Conduct a virtual mooring over a moored ADCP to resolve a tidal cycle (14 days +).
2. Transit to another mooring location 10s of km upslope and profile for a few days, ideally recording another 14 day cycle.
3. Continue profiling between the two moorings until recovery.

This deployment plan would have enabled us to observe the spatial and temporal variability of velocity shear as measured by the glider ADCP, with both ends of the transect corroborated by mooring data.

The deployment did not go as planned. Strong along slope currents of greater than 20 cm s^{-1} prevented station keeping by glider. Additionally, a previously unencountered software issue caused failure of the AD2CP. After final pre deployment tests, I switched the glider off while it was writing data to NVRAM. This caused issues with communication to sensors. As a consequence, no AD2CP data were collected and the glider struggled to navigate. This issue

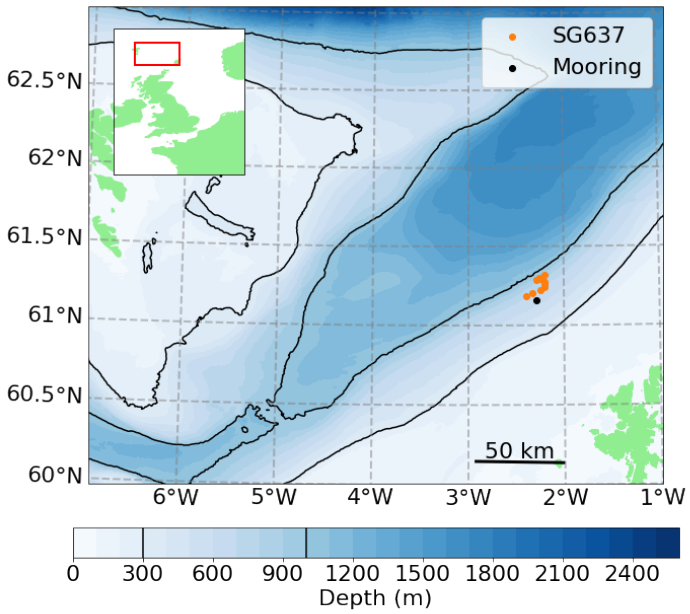

Figure 4.11: Deployment to the Faroe-Shetland Channel. 300 and 1000 m contours are black lines. Orange dots are glider surfacings. Black dot marks the primary mooring. Red box in inset figure marks extent of the map.

with turning off a glider while writing to NVRAM could occur to any glider, but had not been observed previously. The day after deployment, I recovered Omura to the RV *Scotia* under challenging conditions.

This deployment was further inconvenienced by the 2019 GPS rollover that occurred immediately before the *Scotia* sailed. This error occured when the integer number of weeks used by the glider to track GPS satellites increased from 1024 and rolled over to 1, causing the glider to incorrectly believe the date was 1024 weeks earlier. This prevented the glider from communicating with satellites. I applied an emergency firmware update in the field, upgrading to a rapidly produced prototype firmware supplied by Kongsberg. This may have contributed to the failure of the glider when writing to NVRAM. This GPS rollover affected several oceanographic devices, including 19 NOAA monitoring buoys (Duncombe, 2019).

As part of this deployment, I was aboard the RV *Scotia* with no access to the glider base station. I could not check the AD2CP snippet files for quality. To test that the AD2CP was working as anticipated at sea, I wrote scripts to process data from the snippet files the glider sends to the base station. The scripts could be run on the glider base station by the glider pilot. These scripts are detailed in Section 5.3.1 and archived by Rollo (2020a).

After recovery, Omura returned to UEA for servicing and bench tests. The failure mode was examined and reported to the manufacturer. Lessons were learned, and the glider group changed our Standard Operating Procedures to prevent this failure occurring on future deployments. We now avoid powering off gliders while they are writing to NVRAM. We also tes the AD2CP thoroughly in the lab before shipping it for deployment. The next opportunity to deploy Omura came in early 2020 as part of a large scale field experiment in the North Atlantic trade winds region, east of Barbados.

4.5 EUREC^{4}A Deployment

In early 2020, Omura completed a three week long deployment over the abyssal plain east of Barbados. The planning and scientific results of this deployment are detailed in Chapter 4. This was the first successful scientific deployment of Omura. Omura completed 155 dives over 25 days. This deployment was carried out from the RV *Meteor* during cruise M161 as part of the Elucidating the Role of Clouds-Circulation Coupling in Climate (EUREC^{4}A) field campaign (Bony et al., 2017; Stevens et al., 2021).

4.5.1 Automation

For EUREC^{4}A, I automated the snippet quality control script described in Section 5.3.1 to produce quality control images, with no manual intervention required. This was a partial success. The script overwrote early QC images with those from the most recent dive. I have since corrected this behaviour. The script still enabled the to pilots to confirm that the ADCP was turning on and recording expected amplitude and inter-ping correlations. These scripts are archived by Rollo (2020a).

I also wrote scripts to report the locations of gliders and the autonomous surface vehicle *Caravela*. *Caravela* is an uncrewed surface vehicle 5 m in length that can carry and deploy a Seaglider (Siddle et al., 2021). Scripts are archived by Rollo (2021c). These scripts sent the latest location of the gliders and *Caravela* to a central server every minute via the Message Queuing Telemetry Transport (MQTT) protocol. Locations were scraped from Seaglider basestation emails, *Caravela*'s control software telemetry files and the redundant Yellowbrick tracker aboard *Caravela*. These location data were used for real time mission planning during EUREC^{4}A. All platform locations were posted to the publicly accessible EUREC^{4}A dashboard map during the field campaign. The website is no longer online, but the source code has been made available by Kölling and Rollo (2020).

I set up scripts to sync near real-time (NRT) glider data to the National

Oceanography Centre's new Environmental Research Division's Data Access Program (ERDDAP) file server. This fileserver enables near real time access to in-situ observations for use in weather models, reanalyses and other use cases. I also created a process to transfer glider hydrographic data to the RV *Meteor* to assist in planning of CTD casts. To avoid overloading the satellite connection, the data were subsampled and compressed server side, then forwarded to the ship in the early hours of the morning when internet demand was low. I configured the netCDF reader to extract only the essential data: conductivity, temperature and pressure. Finally, I wrote a parser to create pseudo Seabird CTD files so that the glider data could easily be compared with ship collected CTD data in Ocean Data View, the visualisation software used in planning ship operations (Schlitzer, 2020).

4.5.2 ADCP data

Omura was recovered without incident after 25 days of data collection. Ultimately this deployment discovered another issue with the glider-AD2CP integration. The firmware written by Kongsberg had been sending the wrong parameter to the AD2CP, such that it turned off the forward facing beam on descent and turned off the aft facing beam on ascent. This is the opposite behaviour to what is needed for beam spread around the vertical as described in Section 4.4. This issue is visually represented in Figure 4.12. Figure 4.12.a shows the beam spread of the AD2CP when the correct transducers are firing. Figure 4.12.b shows the beam spread when the incorrect beams are firing. This was the case during EUREC^{4}A.

4.5.3 Discovery of fault

This issue with the AD2CP was discovered when examining the glider relative velocities measured during the EUREC^{4}A campaign. Velocity data for each dive are recorded in a matrix of shape S*3*B where S is the number of ADCP ensembles recorded during the dive limb, around 500 per dive limb during EUREC^{4}A. B is the number of time gated depth bins per sample, 15 during EUREC^{4}A. The three columns of the remaining dimension each represent the along beam Doppler velocities for the transducer heads used in recording. During a descent limb this should be fore, port and starboard. During an ascent limb it should be port, aft and starboard. We expect the port and starboard facing transducers to record velocities near zero, as the beams are oriented orthogonally to the direction of glider motion. The fore and aft facing transducers would observe a portion of the glider's forward motion. These would be the velocites in the first column during descent and the second column during the ascent. However, it is apparent from the data that the consistent

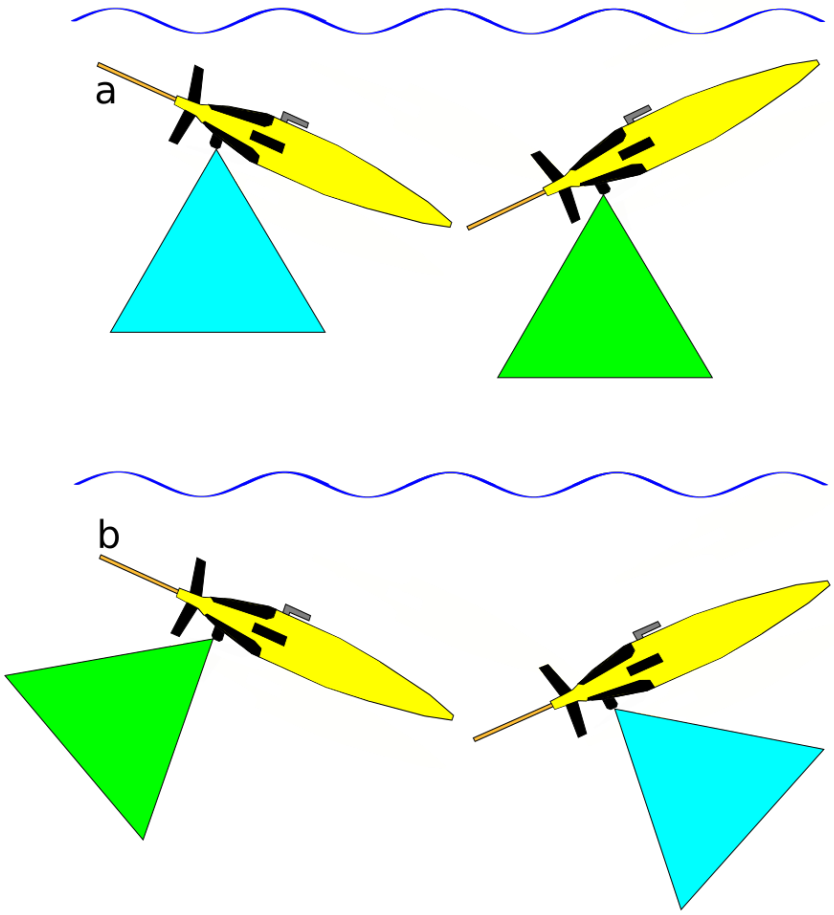

Figure 4.12: Schematic of beam spread of the AD2CP. When the aft transducer is turned off, the beam spread is as shown by the green triangle. When the fore transducer is turned off, the beam spread is as shown by the blue triangle. a) is the desired beam spread, obtained when using EAGLECP. b) is beam spread when the glider is using DORADO with the error in communication protocol.

non zero velocity was in the second column during the descent and the first column during the ascent (Figure 4.13). Following the convention described in Section 4.4, these would be the port transducer in both cases, leading to an initial interpretation of a physically unlikely sideslip motion.

The first cell velocities are approximately the motion of water relative to the glider. As the starboard and port transducers are oriented perpendicular to the glider's direction of travel during normal flight, assuming minimal sideslip and an angle of attack near zero degrees, the along beam velocities should be near zero. From Figure 4.13 it is apparent that the first and third columns during the descent and the second and third columns during the ascent are the port and

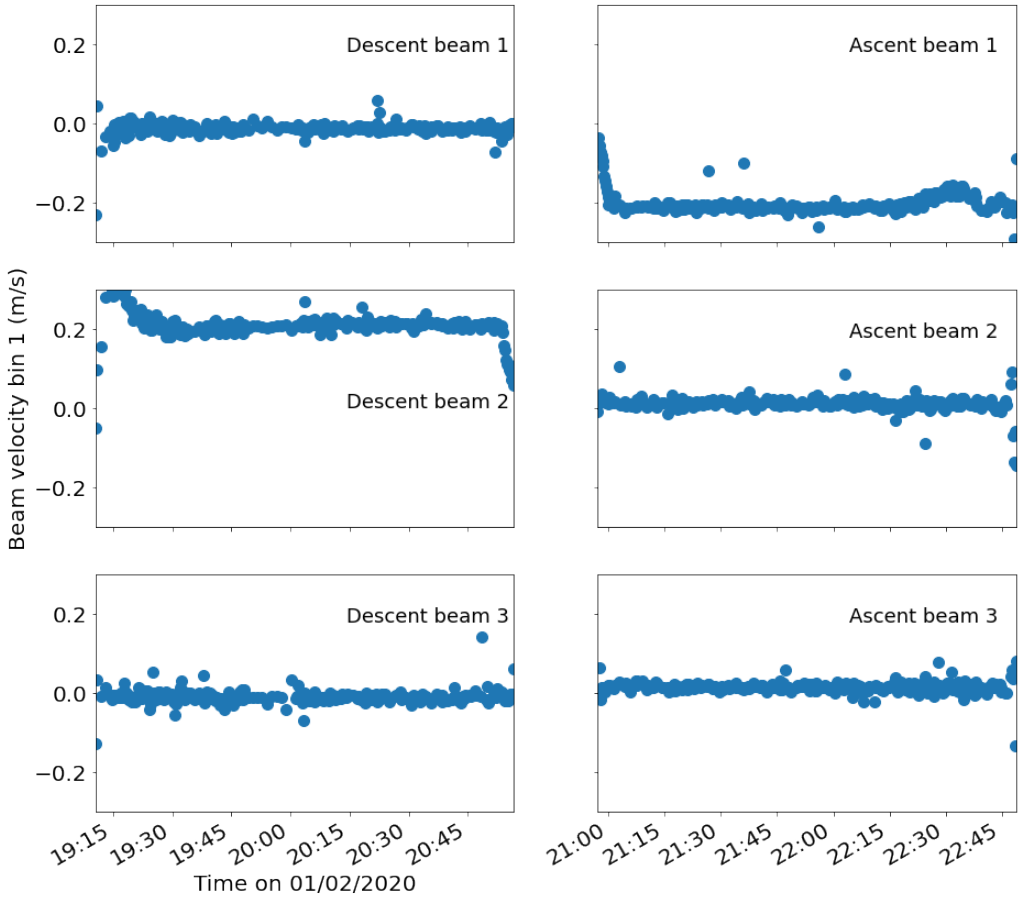

Figure 4.13: Average first cell Doppler velocities of the three beams recorded during descent and ascent limbs during dive 60 of the EUREC^{4}A deployment.

starboard beams. Thus, the beam numbering of the data does not match the beam numbering assumed in correct behaviour of the glider as shown in Figure 4.3 and described in Section 4.4.1.

4.5.4 Description of fault

In email discussions with Nortek technical support, the issue was eventually traced to the communication between the glider and the AD2CP. The critical parameter is **VD** (vertical direction). This parameter is sent to the AD2CP at the beginning of each dive limb to instruct it which beams to use, so as to avoid sampling on the aft beam during descent and fore beam during ascent.

This parameter is set as follows in the NCP_GO file. We used the NCP_GO file sent to us by Elizabeth Creed of Kongsberg 2018-09-05:

SETPLAN,MIAVG=15,AVG=1,BURST=0,**VD=%c**,MV=10,SA=35.0,
SV=0.00,FN="cp%d%a.ad2cp",SO=0

From this snippet, we see that VD is set to %c. From the Nortek Logdev user

guide Revision G 08/11/2016 Seaglider (2016b):

> "**%c** Cast number. Expands to 1 (dive) or 2 (climb). This is the sequential start number within a single dive cycle."

From Nortek support email sent to Callum Rollo 2020-04-24:

> The Kongsberg Seaglider use the VD parameter to select the beams when three beams is configured in a four or five beam system. VD=1 it will use physical beam 2,3 and 4, VD=2 it will use physical beam 1, 2 and 4.

In summary, during a descent limb, the glider sends VD=1 to the ADCP. The ADCP then uses physical beams 2, 3 and 4, so that the forward facing beam 1 is not used (Figure 4.3). During an ascent limb the glider sends VD=2 and the aft beam is not used. This is the opposite of the behaviour we desire for correct sampling. To resolve this issue, Nortek or Kongsberg needed to change their convention of **VD** or **%c**. Alternatively, the ADCP could be set up so that all four beams operate during both dive and climb, as is the case for the SeaExplorer (de Fommervault et al., 2019).

The issues escaped detection until this point due to several compounding factors:

- The AD2CP lacks specific documentation, so much of the interpretation is based on educated guesswork.
- The data files report a beam number, but not a physical identification (i.e. fore or aft facing).
- Technical glider trials were conducted in shallow, strongly tidal waters. Consequently, trial data contained only short periods of stable glider flight in an environment of strong velocity shear. The tell-tale signs of incorrect transducer identification were hidden by this noise.
- I did not think to physically test that the correct transducers were firing during bench tests. To prevent this issue occurring again in future, I designed a procedure detailed in Section 5.4.5 to test the transducers.

The key lesson learned from this experience is "trust, but verify". One cannot assume that sensors integrated by a platform manufacturer will work correctly. The data saved by the sensor may also not be as described. It is much more useful to design thorough lab tests before deploying a sensor in the ocean.

4.5.5 Remedy of fault

In summer 2020, Hydroid wrote a software patch to fix this issue. This patch was delivered as a new firmware for the glider, named EAGLECP. Before and

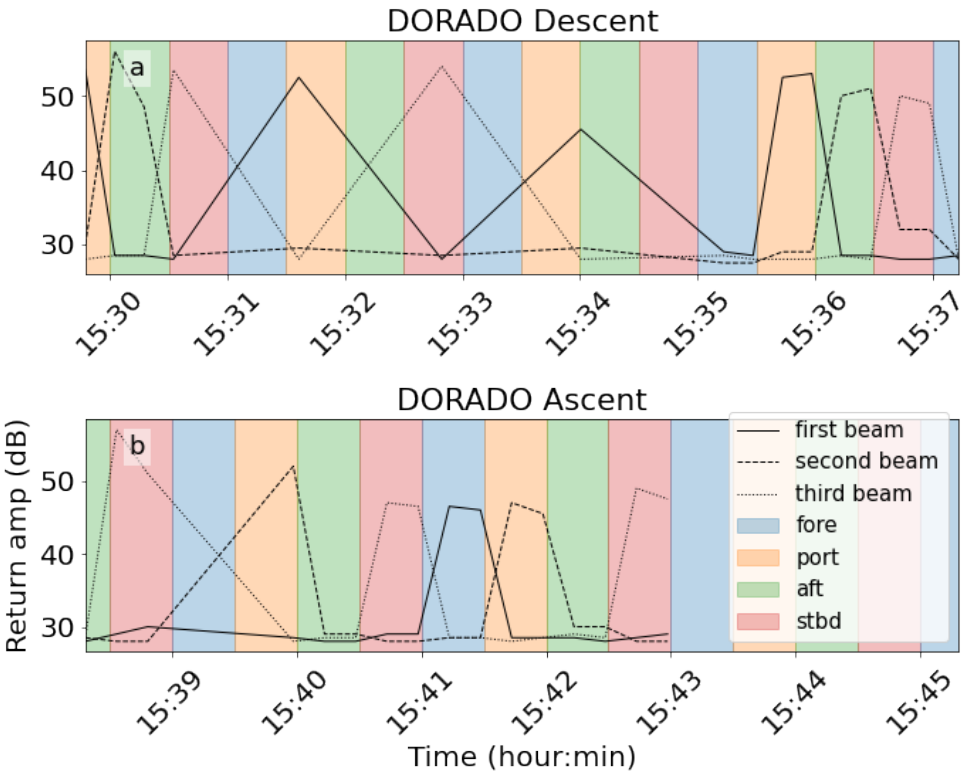

Figure 4.14: Signal return amplitude measured on each beam of the ADCP. The background colour shows which physical transducer is being covered at the time. In this figure, the glider is using the DORADO firmware. Data were recorded during a simulated dive by the glider a) is the descent, b) is the ascent.

after applying the software patch, I tested the AD2CP on the bench. The aims of these tests were:

- To concretely map each physical transducer to a transducer identification number in the output data.
- To definitively test that the correct transducers fire during descent and ascent limbs of a sim dive.

This was achieved by the application of a nitrile glove filled with water to each of the transducers in turn at set time intervals during a sim dive. I then compared the timing of the signal return amplitude increase of the transducers with the location of the water filled glove. The methodology is detailed in Section 5.4.5. ADCPs are designed to have a small acoustic impedance contrast between the material of the transducer face and water, so that the maximum amount of energy is transmitted to the water. As a consequence, an ADCP firing in air measures only a low amplitude response. This can be seen in Figure 4.7 where signal strength drops from $\approx$ 80 dB to $\approx$ 30 dB when the ADCP is removed from the tank. A greater signal return is reported when the transducer is covered by a

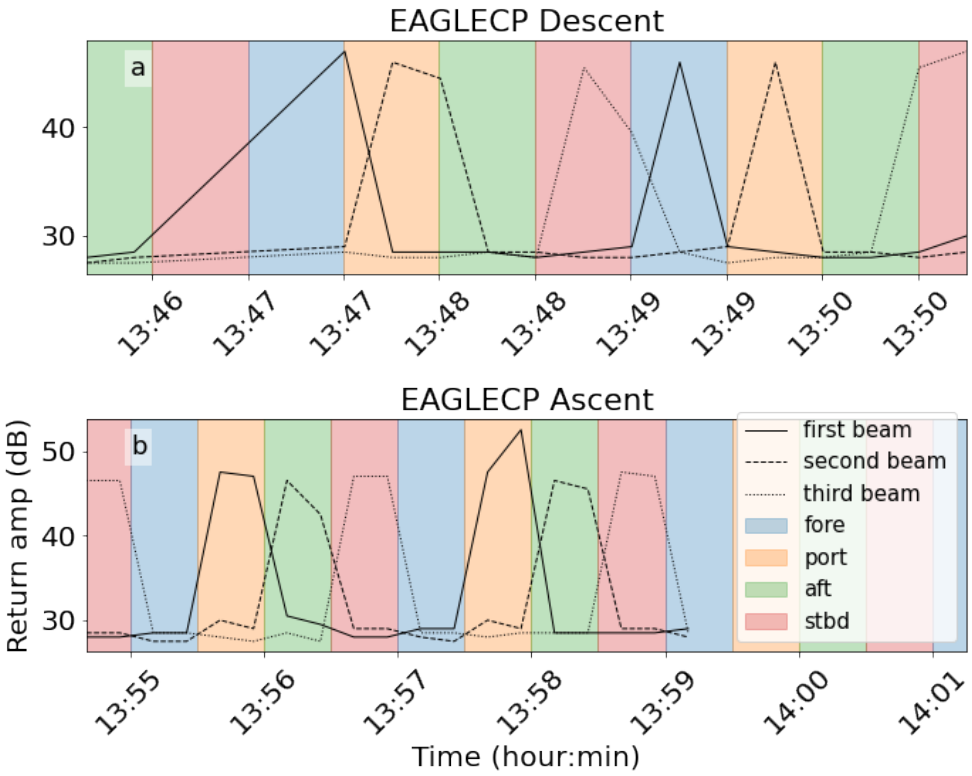

Figure 4.15: As Figure 4.14 for EAGLECP firmware

water filled glove than when it fires in air.

Figure 4.14 shows the results of this test. The background colour indicates which transducer is covered by the water filled glove at that time. An increase in signal return amplitude from one of the transducxers (black lines) indicates that it is covered by the glove. Transducers firing in air report a lower return amplitude. Only three beams are shown, as the ADCP only reports data from the three beams that are turned on. From Figure 4.14 a we see that, using the DORADO firmware, the ADCP turns off the fore facing transducer (purple background) during the descent. It should instead be turning off the aft facing beam (green background). In Figure 4.14 b) we see the opposite behaviour during the ascent; the glider turns on the fore beam and turns off the aft beam. In Figure 4.15 when the gilder is operating under the EAGLECP firmware, this issue is resolved and the aft facing beam (green background) is turned off during the descent. The forward facing beam (purple background) is turned off during the ascent. In case of changes to glider or ADCP firmware in future, this test can be performed in half a day.

4.5.6 Ready for future work

Due to the COVID-19 pandemic and ensuing lockdowns from early 2020 to the time of writing, I was unable to deploy SG637 to collect any further data. However, after the trials and tribulations that took up most of my PhD, SG637 Omura is now where she should have been in 2017. The AD2CP communicates with the glider, turns on the correct beams, and records data. Data are recovered from the memory card of the AD2CP and processed using the tools in Section 5.4.2. In brief this consists of:

1. Convert .ad2cp binary files to netCDF with Nortek MIDAS software.
2. Parse data from these into a table of average values per mission and a dictionary of class instances, which contain self describing data, for each dive limb (one descent and one descent per dive). This enables quick dive-to-dive comparisons of average data and full analysis of the ADCP dataset.
3. Carry out QC for low correlation and signal return. Following (Todd et al., 2017) we exclude data with an inter-ping correlation of less than 0.5 or a signal return of less than 13 dB above the noise floor.
4. Flag for pitch and roll outside of the acceptable space.
5. Construct profiles of shear at small scale (O 10 m).
6. Combine these shear profiles using an inverse method.
7. Use dive limb and timestamp matching to collocate ADCP data with CTD data from the glider.

The above process has been automated after Step 1 with freely available open source tools. I have written tests for the core scripts. In particular coordinate transforms. This software is archived by (Rollo, 2020b), with an actively developed version hosted on GitHub `https://github.com/callumrollo/adcp-glider`. The software succesfully extracts AD2CP data and combines it with data from the glider CTD. It can detect issues with physical misalignment of the AD2CP and calculate bulk estimates of data quality. As I have not succcesfully collected a dataset using the AD2CP during my PhD, I cannot confirm that the current profiles that it produces are accurate. These should be compared to in situ data from a fixed ADCP in trials such as those we undertook in the Faroe-Shetland Channel, using the fixed firmware.

The process of using a new sensor on a glider could be improved by better communication between the manufacturer and end-users. Other glider manufacturers such as ALSEAMAR include documentation on each sensor integration in their glider manuals [cite]. This would reduce the potential for mistakes during use. It would also be useful to have end-users evaluate data from initial trials by the manufacturer. This could have caught the issue with

incorrect beams caused by the Seaglider firmware.

Omura has now been deployed four times in a range of environments. Although we have not been able to collect an ideal dataset with the AD2CP, we have learned a lot about the system. The following Chapter has been written as a cookbook style description of the AD2CP glider system and how to use it.

5

ADCP Glider Guide

This Chapter is an archived copy of the document hosted on GitHub at `https://github.com/callumrollo/adcp-glider-guide` and archived by Rollo (2020a) in October 2020.

This informal guide was compiled using information from the Nortek Signature manuals, in particular the Integrator's Guide (Nortek Group, 2017b), correspondence with Nortek and Seaglider (now owned by Huntington Ingalls Industries, previously Kongsberg and Hydroid Inc.) support teams, published data from previous integrations on the Seaglider and Spray platforms, and personal experience working with the system 2018-2020. This guide comes with no warranty, guarantees of competence, or support. See licence file for full details. For qualified and competent technical support contact:

support@nortekgroup.com

seaglidersupport@hydroid.com

5.1 To the bench

To connect to the AD2CP for bench testing you will require:

- **AD2CP Signature Deployment and MIDAS software** from `https://www.nortekgroup.com/software` (software is Windows only as of October 2020).
- **A Windows computer with an Ethernet port**.
- **AD2CP manuals "Signature Operations" (Nortek Group, 2017b) and "AD2CP Integrator's Guide" (Nortek Group, 2017a)** from `https://www.nortekgroup.com/manuals-quick-guides`.
- **Powered Ethernet to standard Subsea 8 pin cable** this is included in the glider case.

The Nortek website is the authoritative source for all information regarding the AD2CP, and should be checked for the latest software and manuals.

5.1.1 Connect to the AD2CP

1. Ensure that both glider and AD2CP Ethernet cable are powered **off**. It is not necessary to disconnect the AD2CP to glider serial cable at the port marked "R"
2. Remove the dummy plug and connect the 8 pin Subsea connector to the starboard port of the AD2CP. The port is marked "E" for Ethernet. **N.B**

the serial and Ethernet ports on the glider AD2CP are the opposite way round to that shown in the Signature 1000 guide diagram.
3. Connect the Ethernet cable to your Windows computer.
4. Connect the power supply and power the cable. The Ethernet port on your computer should light up. The blue light between the transducers on the AD2CP should turn on.
5. Open the Signature Deployment software and wait 1-2 minutes for the AD2CP to assign an IP address.
6. In Signature Deployment select menu option "Discover,". You should see a row of data appear with the sensor highlighted in red. Right click this and select "view in browser" to see instrument information and download data files. Select "open in command mode" to control the instrument and conduct bench tests.

The Signature Deployment software expects sensors from the Nortek Signature range but has the capability to interact with the glider mounted AD2CP. Using this software it is possible to communicate with the AD2CP via a terminal emulator, download files from the AD2CP and start recording data. Data visualization/interpretation is not supported as of October 2020.

5.1.2 Bench test the AD2CP

For ease of reading I have printed all commands in **BOLD UPPERCASE** but the AD2CP is not case sensitive.

1. Open the command window as detailed above and send the following commands:
2. **INQ** to check the glider is in state 0002 ready to receive commands. Otherwise see instrument states (Table 5.1).
3. **LISTFILES** to see what files are already on the memory card.
4. **SETDEFAULT,ALL** a good place to start. This sets all AD2CP recording settings to their default values. No AD2CP data files will be affected.
5. **SETPLAN,FN="sensible_filename.ad2cp"** to ensure you do not overwrite pre-existing files. The previous command sets default filename Data.ad2cp. You must specify the .ad2cp file extension.
6. Change other variables as you see fit. There are some suggestions later in this guide.
7. **SAVE,ALL** to test if your configuration is possible with the instrument. If this returns **OK** you can deploy, otherwise **GETERROR** will tell you which settings are incompatible. It is a good idea to **SAVE,ALL** after each variable you change to ensure you entered a compatible value.

8. **START** this will put the instrument in record mode. Leave it to collect data.
9. To finish recording, use the GUI buttons "send break" and "switch to command mode" or send keyboard commands **CTRL-C** then **MC**.

5.1.3 Instrument modes

The AD2CP operates in various modes. Table 5.1 lists the numerical codes returned by the command **INQ** and the corresponding operating modes. Figure 5.1 shows the commands for switching between modes.

Mode number	Instrument Mode
0000	Bootloader/firmware upgrade
0001	Measurement
0002	Command
0004	Data retrieval
0005	Confirmation
0006	FTP-mode

Table 5.1: AD2CP operating modes

5.1.4 A sample plan for a glider deployment, as used in tank testing

SETDEFAULT,ALL

SETPLAN,FN="todays_date_and_start_time_tanktest.ad2cp"

SETPLAN,MIAVG=30

SETAVG,AI=2

SETAVG,NC=15

SETAVG,CS=2.0

SETAVG,NPING=8

START

This will record a profile every 30 s. Each profile will average 8 pings over a two second period. The ADCP will record 15 cells of 2 m size.

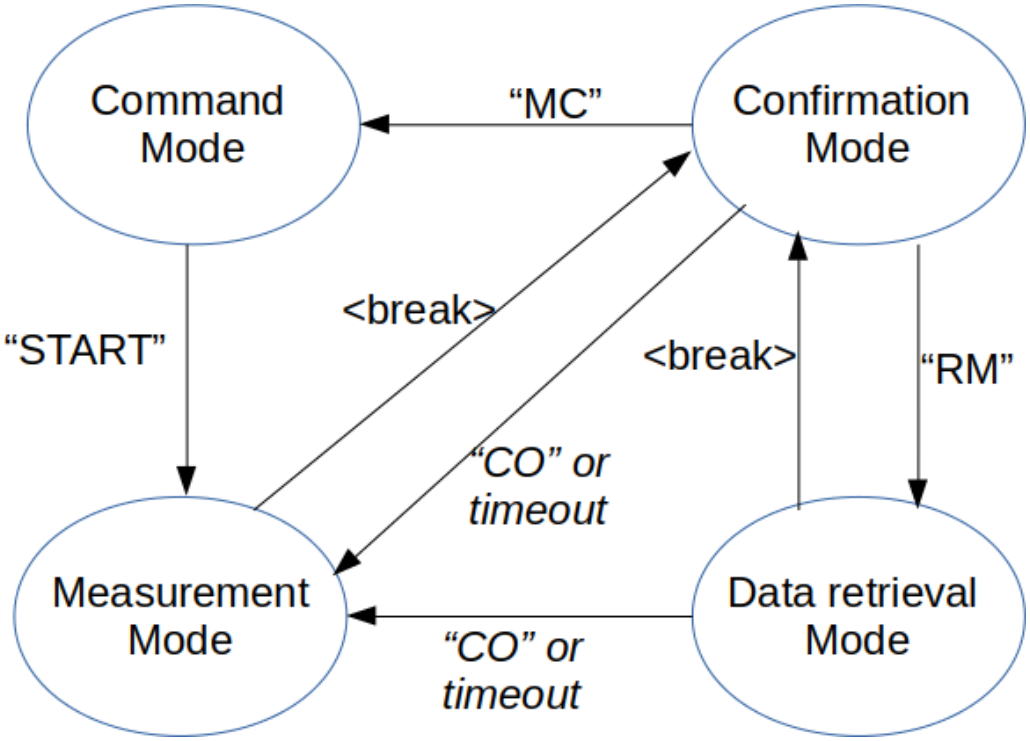

Figure 5.1: Modes of the AD2CP and commands to switch between them. Numbers from Table 5.1. Adapted from the Nortek AD2CP Integrator's Guide (Nortek Group, 2017a). ¡break¿ command is CTRL-C

5.2 More detail on the AD2CP

5.2.1 Handy commands

Commands for parameters typically have three key options: **GET** for the present setting, **GETLIM** for the acceptable range of values, and **SET** to assign a new value to a parameter. To confuse things, parameters are grouped into a number of categories which must be stated when interrogating that parameter. e.g. to interrogate the cell size **CS** parameter for the average profile use: **GETAVG,CS** to find its present value, **GETAVGLIM,CS** to find the accepted range of cell size values, and **SETAVG,CS=x** to set a new cell size of x metres. Values such as filename are controlled through the group **PLAN** rather than **AVG**. An example usage is **GETPLAN,FN** to return the current filename.

General commands:

- **BBPWAKEUP** when connected to instrument, wakes it up so it will receive commands.
- **INQ** get glider state. Glider must be in mode 002 to receive other commands.
- **GETSTATE** for more detailed info than **INQ** regarding deployment time etc.

- **GETPLAN** for details on the deployment plan, including the filename for data.
- **GETPLAN1** for the alternate plan parameters (these parameters are set to 0 by default).
- **GETALL** and **GETALLLIM** for most parameters and their ranges of accepted values.
- **GETPRECISION/GETPRECISION1** for precision in burst and avg mode (cm s^{-1}) for plan 0/plan 1.
- **RECSTAT** for recorder (memory card) information, free blocks etc.
- **LISTFILES** list all files on the memory card.
- **GETCLOCKSTR** to get the clock. This syncs from the glider clock on each dive.
- **SETTMAVG** for averaging of profiles. Used for generating snippet files. Snippet files are small subsets of data from the profile that are transmitted to the basestation when the glider surfaces.
- **ERASE,9999** wipes the recorder to free up space for more data. This will also reset any plans loaded. Make sure you copied all the data you need before using this.

N.B. **GETALL** will return some errors as the custom glider AD2CP lacks some of the functionality of the Signature 1000 such as a vertical beam. Don't panic, your sensor is fine.

5.2.2 On data limit formats (values returned by GETLIM commands)

The limits for the various arguments are returned as a list of valid values, and/or ranges, enclosed in parenthesis () (Table 5.2). An empty list, (), is used for arguments that are unused/not yet implemented. Square brackets [] signify a range of valid values that includes the listed values. Single characters are enclosed in single quotes ''.String arguments are encapsulated with double quotes "". A semicolon ; is used to indicate a range of values between two inclusive points, and as a separator between sets of valid values. The argument data type can be inferred from the limits. Integer values are shown without a decimal point. Floating point values are shown with a decimal point.

5.2.3 Explanation of Terms

- **SETPLAN,MIAVG** is the time period between successive average measurements. **SETAVG,AI** is the time interval over which the measurements are averaged. So setting **SETPLAN,MIAVG=20** and **SETAVG,AI=5** will instruct the sensor to record data for 5 seconds every every 20 seconds.

Value	Explanation
([1;128])	Integer value, valid from 1 to 128.
([1300.00;1700.00];0.0)	Floating point value, valid values are 0.0 and the range from 1300.00 to 1700.00.
([‘0’;‘9’];[‘a’;‘z’];[‘A’;‘Z’];‘.’)	String argument with valid characters being . and the character ranges a-z, A-Z, 0-9.
(“BEAM”)	String argument with BEAM being the only valid string.
(0;1)	Integer value with two valid values, 0 and 1.

Table 5.2: Example values returned by the **GETLIM** command

- The .ad2cp files store all the variables that the AD2CP was set to during recording, so there is no need to record what commands you sent to the instrument.
- The AD2CP will only use 3 beams at once, you must set the vertical direction to avoid disappointment! The glider will do this automatically when performing dives (including sim dives), but for bench tests you must change it manually with **SETPLAN,VD**.
- If a co-ordinate system other than **BEAM** is set (e.g. **XYZ**), the AD2CP will convert to this system at time of recording. This conversion is difficult to reverse later and an error in the compass/tilt sensor could negatively affect data. Nortek recommend recording in BEAM mode and carrying out any coordinate transformations in post processing.
- The coordinate systems are: **BEAM**, records along beam velocity, **XYZ** glider coordinate system with **X’** toward nose (Figure 4.3), **ENU** Earth coordinate system East North Up, shown as **X** in Figure 4.3.
- The AD2CP can run two average and two burst plans concurrently so many parameters have four settings, **SETBURST** for burst mode in plan 0, **SETAVG** for average mode in plan 0 and **SETBURST1**, **SETAVG1** for the same parameters in plan 1. See the Integrator’s Guide for more detail.

5.2.4 What to do if the AD2CP demands a password

The AD2CP occasionally requires a login, usually after being left powered on for more than 30 minutes with no input. The details should be

Signature Username: nortek
Password: (blank)

or Signature Username: nortek
Password: nortek

If neither of these work, temporarily interrupting the power supply and restarting Signature Deployment will get you back in. This stops the AD2CP from recording data but no data is lost. The password can be reset when connected via Ethernet.

5.2.5 Miscellaneous handy information

When connected to power, a steady blue light on the AD2CP indicates that it is drawing power and not actively recording. When deployed, the light blinks when the transducers sends out an acoustic ping. With each ping, there is a quiet but audible click.

Testing showed that the AD2CP's clock drifts at approx 1 second per week. However the clock syncs with the Seaglider clock at the start of every profile. The Seaglider in turn syncs its clock with GPS satellites, so this should not cause any issues.

The AD2CP has a 16GB memory card.

The AD2CP does not have:

- a vertical beam
- bottom tracking
- pulse coherence
- onboard power
- active beam remapping

The Ethernet comm port connects to a dedicated Linux processor. This can handle connections over telnet, raw connection and FTP. It should be possible to connect to the instrument this way, without using Nortek's dedicated software.

SETALTERNATE is a potentially useful but quite confusing feature of the AD2CP. It allows the user to run two completely independent AD2CP setups in tandem. The primary configuration runs for **PLAN** seconds, the unit then powers down for **IDLE** seconds. The secondary configuration runs for **PLAN1** seconds followed by an idle period of **IDLE1** seconds. The process then repeats. All data are recorded to the same file, so the filename **FN** in **SETPLAN** and **SETPLAN1** must be the same. The valid range for the various arguments should be verified using the **GETALTERNATELIM** command. Caution is recommended if using this functionality. Consult the Integrator's Guide for more detail (Nortek Group, 2017a).

5.3 Controlling the AD2CP through the Seaglider

This requires three things:

1. Seaglider must be using a main.run variant that works with the Nortek AD2CP. As of August 2020, firmware version EAGLECP is recommended by Hydroid. This is a version of firmware 66.12 EAGLERAY. This firmware version solves some timing issues that CLOWNFISH and earlier versions had with the AD2CP as well as an issue in DORADO where the AD2CP was turning the wrong beams on and off during ascent and descent. For further details contact Hydroid support.
2. The file ncp.cnf must be loaded to the glider memory card and stripped of padding bits, following the procedure in Seaglider (2016a). This contains low level commands for the glider-AD2CP interface.
3. The file NCP_GO must be present on the basestation and the settings stipulated in it must be valid for the AD2CP. i.e. the AD2CP does not return an error when you try to do a bench test with these settings. This file can be updated during a deployment to change the AD2CP settings.

Note: the NCP_GO file supplied to the UEA glider group by Elizabeth Creed in September 2018 is rejected by the glider, due to the inclusion of an incorrect command for the snippet file coordinate system, settmavg,cy="ENU". This should be set to "BEAM".

To toggle the return of snippet files (approximately 8 Kb per dive), use the command $CP_XMITPROFILE in the cmdfile on the glider base station. $CP_XMITPROFILE,1 to turn on snippet files or $CP_XMITPROFILE,0 to turn off.

5.3.1 Telemetry/snippet files

If telemetry is enabled, the glider will send back snippet files over Iridium. Once all the parts are uploaded to the basestation, two files will be generated for each dive: cpNNNNau.r for the descent and cpNNNNbu.r for the ascent, where NNNN is the four digit dive number. These data are then combined in pcp637NNNNa.dat

The telemetry files are made up of repeating blocks of National Marine Electronics Association (NMEA) 0183 messages. These are human readable ASCII files organised in rows with values separated by commas. The first row of each block specifies the instrument type (4=Signature), and other constants:

```
$PNORI1,4,100476,3,15,0.30,2.00,BEAM*0F
```

These NMEA strings consist of three parts:

1. `$PNORI1` is the "talker". In this case `P` identifies a proprietary system, `NOR` is the identifier for Nortek, and `I1` is the Nortek code for this message string.

2. `4,100476,3,15,0.30,2.00,BEAM` The comma separated values are the values of parameters specified by the manufacturer for this message type, identified by their position. Where data are not available, an empty space is left e.g. `4,100476,,,0.30,,BEAM` such that position is not lost. In this NMEA message type, the values are: number of transducers on instrument, instrument serial number, number of beams recording, number of cells, blanking distance (m), cell size (m), and coordinate reference frame.

3. `*0F` is an optional checksum in hexadecimal, calculated by bitwise exclusive OR of the ASCII characters between the `$` and `*` of the message.

For more information on NMEA, see the pdf guide from the pynmea2 library `https://github.com/Knio/pynmea2/blob/master/NMEA0183.pdf` this package performs a number of useful functions, including checksum calculation and NMEA string parsing (Flanagan, 2016).

The second row:

```
$PNORS1,112318,113108,0,2A4C0002,13.8,1497.3,0.00,
226.4,18.0,0.00,-1.5,0.00,63.305,0.00,11.83*7F
```

Specifies instrument constants: date (mmddyy), time (hhmmss), error code, status code, battery voltage (V), sound speed ($m^{-1}s$), heading standard deviation (°) heading (°), pitch (°), pitch standard deviation (°), roll (°), roll standard deviation (°), pressure (dbar), pressure standard deviation (dbar), temperature (°C).

After this there are multiple rows beginning $PNORC1, one for each sample taken.

```
$PNORC1,112318,113108,1,2.3,0.083,0.113,-0.039,64.0,63.3,63.4,86,
82,75*5D
```

The columns of this data following the talker string are as follows: date (mmddyy), time (hhmmss), cell number, cell distance from transducer, velocity head 1, velocity head 2, velocity head 3, return amplitude head 1, return amplitude head 2, return amplitude head 3, correlation head 1, correlation head 2, correlation head 3. Distance in m, velocity in $m\ s^{-1}$, amplitude in dB, correlation in %.

The python script `tele_checker.py` by Rollo (2020a) reads these text files and plots the beam amplitude and correlation for each dive in groups of 10 ensembles.

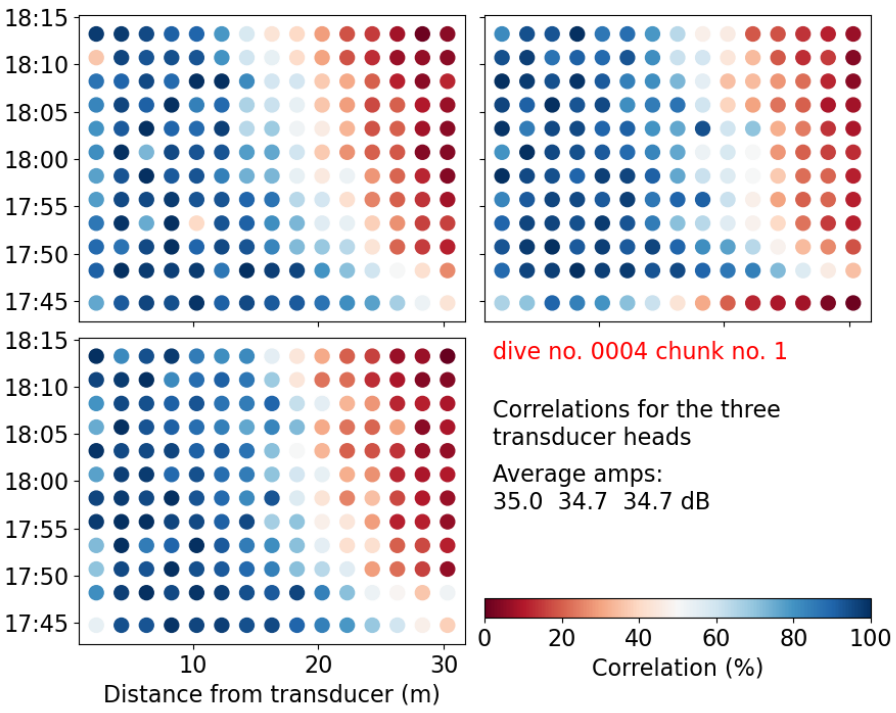

Figure 5.2: Inter-ping correlation from an AD2CP snippet file. Each dot represents a sample from the ADCP at the time and depth indicated on the axes. The three subplots each represent a beam. As each sample contains multiple pings, the ADCP reports the correlation between them.

Each plot typically covers 40 - 60 minutes of data. These plots are saved as in png format with file names `tele_amp_NNNN_X.png` and `tele_cor_NNNN_X.png` where NNNN is the dive number and X the chunk number. Figures 5.2 and 5.3 show example snippet file data from a deployment in oligotrophic waters with good quality data.

Snippet files can be interpreted by the glider pilot to determine if the AD2CP is functioning as expected. Figure 5.2 shows the percentage correlation between pings in an ensemble. Correlations greater than 50 % are in blue. We expect correlation great than 50 % out to 10 m at least. The range may be less in low scattering environments however. The first cell often has a lower correlation, typically due to ringing. Ringing is a consequence of the transducer design, with the same physical sensor transmitting and receiving the acoustic pulse. For the closest cell, the transducer head may still be vibrating from the sent pulse when it measures the returned pulse, this is referred to as ringing. Amplitude drops off rapidly with distance (Figure 5.3). This is raw return amplitude, not gain adjusted so this behaviour is expected. The pilot should check to ensure all three

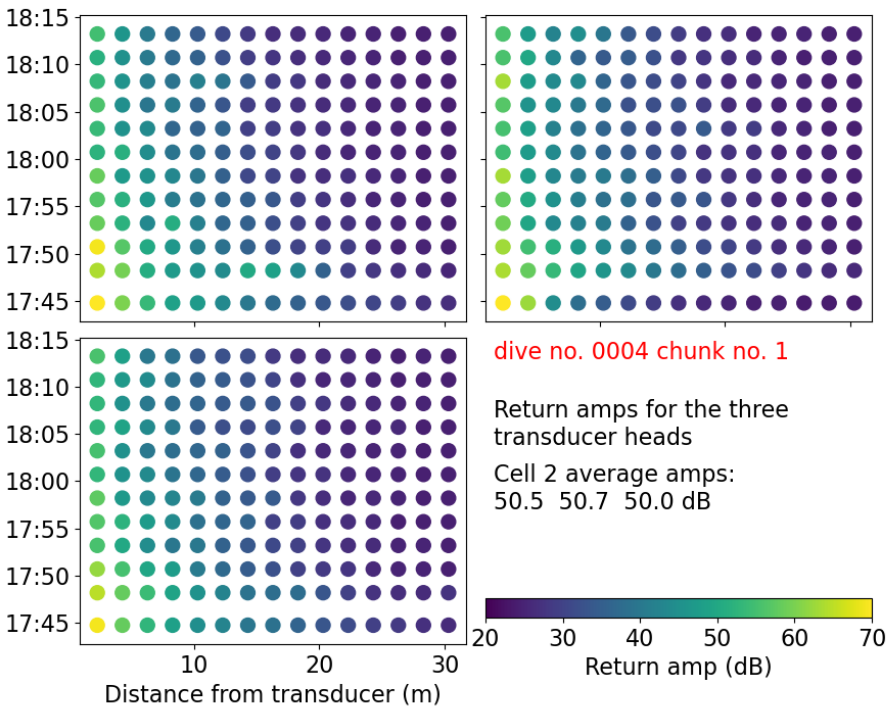

Figure 5.3: Amplitude return from an AD2CP snippet file. This follows the same structure as Figure 5.2 but for the return amplitude of the samples.

heads report similar return amplitudes. Return amplitude is dependent on the amount of suitable size scatterers in the water column. For the AD2CP, these scatterers are of a similar size to zooplankton (Rusello et al., 2012). As a result, return amplitude will decrease in clear water.

Call `tele_checker.py` from the terminal using **python telechecker.py -p 'path-to-your-adcp-snippet-files'**. Make sure that the Python libraries required by the script are in your shell path. Snippet files can be processed automatically by adding this command to a glider's `.logout` file. The script checks for existing figures, so only new snippet files are processed. If you wish to force reprocessing, remove the figures from the directory before calling the script. The script also produces average plots using all the snippet file data in the folder.

5.3.2 Further snippet files details

The settings for snippet files can be changed in NCP_GO with **SETTMAVG**. The following arguments can be specified:

- **EN** Enable Averaging Mode Telemetry. 1 to enable, 0 to disable

- **CD** Cells Divisor
- **PD** Packets Divisor
- **AVG** Average Telemetry Data
- **TV** Store Velocity
- **TA** Store Amplitude
- **TC** Store Correlation
- **CY** Coordinate System
- **FO** Enable File Output
- **SO** Enable Serial Output
- **DF** Data format **Do not change!**

5.4 Recommendations for operators

5.4.1 Deployment guidance

Average mode is best for shear velocity information. Low power consumption and good data quality can be achieved by averaging every 15 or 30 seconds using 4 or 8 ensembles. Burst mode is geared toward measurements of turbulence. This is more power hungry and will fill up the memory card faster. Burst mode allows more pings per second.

During deployment, the glider should be kept within an attitude envelope that orientates the three operating transducers at similar angles from the vertical. If the glider pitches or rolls outside of the envelope, the beams will sample water parcels at different depths (Figure 4.6). The AD2CP does not actively resample by changing time gating of data recording as some other ADCPs do (e.g. Shumuk et al. 2018).

I recommend using the maximum bin size of 2 m to ensure sufficient scatterers in each bin for reliable measurements. If a smaller bin is used, the glider attitude must be more tightly controlled.

I recommend recording in glider coordinates (BEAM). The conversions to XYZ and ENU rely on the AD2CP's attitude sensors. If there is an error with these, it is difficult to recover the original AD2CP data. Conversely, the conversion from glider coordinates to XYZ or ENU is trivial. Functions provided by Rollo (2020b) perform this conversion.

5.4.2 Data analysis options

The free Nortek software SignatureViewer will display data and show you that the sensor is recording at the intervals you set. However, it does not process the three beams correctly as it expects four beam input. You can use SignatureViewer to

export data files as an ntk Nortek binary file and then view them with another Nortek program.

Nortek MIDAS will read .adcp files and convert them to netCDF4, matlab or csv format. It will also convert to and replay ntk files.

5.4.3 How to convert the .ad2cp files for analysis

1. Open Nortek MIDAS
2. In the Data menu use the option "AD2CP to ntk" to convert your binary ad2cp file to a re-playable ntk.
3. In the same Data menu there are tools for exporting these ntk files to netCDF4, Matlab and ASCII format.
4. The netCDF4 files are open source standards that can be read into a number of programs with the netCDF4 library.

The repository provided by Rollo (2020b) contains Python scripts that takes as input the netcdf files created in step 3 and the output of the UEA Seaglider Toolbox (Queste, 2014).

5.4.4 Bench tests before and after all deployments

A number of bench tests are recommended before deploying the ADCP glider, particularly after making any changes to the AD2CP or glider firmware. The process for setting up the glider for bench tests is described in Section 5.1. As part of bench testing, sim dives should be performed.

It is recommended to carry out bench tests in a tank prior to deploying the glider. Testing in a tank will test that the four transducers record a similar signal return in water. If the signal return of the transducers differs by more than a few decibels, this could be a sign of a damaged transducer. Due to the amount of acoustic ringing in a tank, the measurements of water velocity reported will not be reliable.

5.4.5 Physically test transducers

Rationale: At least one Seaglider firmware version (66.12 DORADO) had an error that supplied the opposite orientation parameter to the AD2CP during descent and ascent phases (Section 4.5.3). This caused the incorrect beam to be switched off, though the AD2CP sent out pings and recorded data as normal. To test that the AD2CP is behaving as expected, I recommend that you physically test the transducers during a sim dive.

This can be accomplished by the simple expedient of a water filled nitrile glove and a timing source. Be sure that your timing source matches the AD2CP. The

Figure 5.4: A nitrile glove filled with water is pressed against the transducer heads of the AD2CP

simplest way to achieve this is to conduct a sim dive after the glider has synced its clock to GPS and use a similarly synced source. ± one second agreement between the clocks is good enough. To conduct this test, follow these steps:

1. Set the AD2CP up to record every 15 seconds (see example in Section 5.1.4) using the NCP_GO file on the base station.
2. Start the glider on a sim dive to at least 30 m, to ensure a long enough

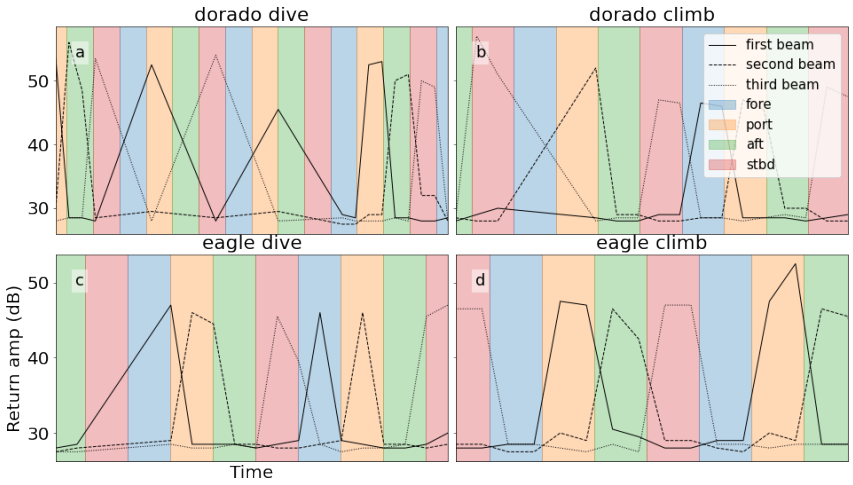

Figure 5.5: Example result of transducer testing when used to test a firmware fix. Under the old DORADO firmware (a and b) the fore facing beam was switched off during the dive and the aft facing beam was switched off during ascent, the opposite behaviour to what was desired. The issue was fixed with the EAGLECP firmware (c and d)

.

time series for recording.

3. Fill a nitrile glove, balloon or similar with water and place it over each transducer head in turn, recording the timing of each placement (Figure 5.4).
4. Once the sim dive is finished (both descent and ascent), turn off the glider and recover the data.
5. Plot the amplitude return of the transducers and compare with the timing of when each transducer was covered. Covering the transducer with a water filled glove significantly increases the return amplitude of the signal, in comparison with the other transducers that are firing in air (Figure 5.5). For detailed plotting, see the example at `https://github.com/callumrollo/adcp-glider/blob/master/notebooks/bench_tests.ipynb`, this is included in the repository provided by (Rollo, 2020b).
6. One transducer will not fire. This will show on the plots as the vertical strips of a single colour which have no large values of amplitude within them. Check that the transducer corresponding to this colour is the correct one. For ideal data collection, the aft-facing transducer should be switched off during the descent, the fore-facing transducer should be switched off during the ascent.

Carrying out this test will detect incorrect transducer setting instructions sent from the glider to the AD2CP. The transducers should be tested following this routine after every firmware update of the glider or the AD2CP.

This section contains the minimum information an operator would require to test and deploy Omura or a similar AD2CP-glider. I have only covered a subset of the capability of this system. The Nortek and Kongsberg guides should be consulted for more complete descriptions. The relevant suport teams should be contacted for updates.

6

Conclusions

This thesis has described the results of two successful glider missions in the North Atlantic and a novel glider-sensor integration. In the spirit of NEXUSS, this thesis has covered both technical and scientific progress. In this chapter, I will summarise the conclusions and lessons learned from these projects. I will also make recommendations for changes to SG637.

Using a previously unpublished dataset, Chapter 2 described the evolution of two upwelling events observed over the NW Iberian margin. Geostrophic transport estimates showed equatorward flow over the shelf and upper slope throughout the 70 day deployment (Figure 2.6). This is previously unobserved behaviour that occurred during one of the strongest upwelling seasons since observations began in 1967 (Figure 2.2). A temporal lag was observed between the peaks of chlorophyll *a* and dissolved oxygen during these events (Figure 2.8). This temporal lag is a previously unobserved phenomenon. However, a temporal lag was not observed during the second upwelling event (Figure 2.7). The reason for the differing response during the two upwelling events is an outstanding question. Better understanding the plankton community assemblage and growth dynamics could elucidate this, as the proxy of chlorophyll *a* concentration does not capture all of the variability of primary production. Future studies should combine physical oceanographic observations with ship based sampling of plankton during the evolution of an upwelling event. As part of this work, the glider dataset collected has been processed and made publicly available by Rollo et al. (2020b).

The NW Iberian margin is an area that could benefit from repeated glider observations of an upwelling system, such as the regular occupations of cross shelf transects in the Californian Current System (Rudnick et al., 2017). Increased observational frequency could elucidate the apparent delay in response between chlorophyll *a* and dissolved oxygen. This would improve our understanding of shelf break processes, especially in the subsurface where satellite observations are not available. A cross shelf break transect such as this is an ideal use case for an ADCP glider (Todd et al., 2017). A glider such as SG637 could be usefully deployed to the NW Iberian margin to observe ageostrophic flows around the shelf-break. The use of an ADCP would enable direct observation of onshore and offshore flows driven by Ekman pumping. These flows are oriented along the direction of the glider's cross-shelf transect, so cannot be estimated from geostrophy with this sampling pattern. The glider would still be limited by its inability to navigate in flows faster than 0.2 m s^{-1}. Direct observation with an ADCP mooring and glider over a 14 day + period would also enable direct estimates of tidal currents on the shelf, enabling more accurate detiding of the remaining currents. ADCP moorings could also ably cover the inner shelf that the glider cannot reach, and where the $<$ 50 m water

depth would allow the use of a high-resolution short range ADCP.

This work demonstrated a limitation of gliders. While the survey vessel was able to complete a transect of CTD casts across the shelf and upper slope in under 24 hours, it took the glider four days on average to cover this distance (Figure 2.6). This gap between subsequent observations of the inner shelf limited our ability to constrain the time lag between local peaks in chlorophyll *a* and dissolved oxygen concentration. At the time of this deployment on the NW Iberian margin, SG510 was the only glider operated by UEA glider group. This limitation in temporal resolution of cross-shelf processes could be avoided by deploying multiple gliders to the same transect. This strategy has been used successfully during several missions completed by the UEA glider group, including the EUREC^{4}A. Alternativily, this observatory could be improved by a glider completing a cross shelf transect between ADCP moorings. Moorings would be particularly valuable on the inner shelf to observe periods of high current flow which prevent the glider from navigating on the shelf.

In Chapter 3, the potential for automated classification of thermohaline staircases in glider profiles was explored. This work observed the edge of large scale thermohaline staircases in almost exactly the same location as the original C-SALT experiment 35 years ago (Figure 3.2). These are remarkably stable structures in the open ocean. To identify these staircases, we developed an automated classifier based on the work of van der Boog et al. (2021b). Our classifier is generalised vertical profiles of temperature and salinity at any regular spacing and gives the end user more control over critical parameters (Rollo, 2021a). We hypothesise that the incidence of thermohaline staircases is limited by large background gradients in conservative temperature and absolute salinity. We also used a fast thermistor to classify thermohaline staircases across a range of vertical scales. We concluded that thermohaline staircases are highly sensitive to vertical sampling resolution, and this is likely to be a limiting factor in their detection in 1 dbar argo profiles. Strong vertical gradients in temperature and salinity correlate with smaller maximum step size in our observations (Figures 3.10 & 3.13). Owing to this dependence of step size on background gradients in temperature and salinity, and staircases are more likely to be underestimated in regions with high background gradients in temperature and salinity.

Outstanding questions remain on the magnitude of this potential underestimation of thermohaline staircases in regions with strong background gradients in temperature and salinity. Enhancement of diapycnal mixing rates by salt finger dynamics is dependant on temperature and salinity gradient, not the sizes of the steps (van der Boog et al., 2021a), so the contribution of small

staircases could be substantial. Thermohaline staircases cover a large geographical area and are mostly found in the uppermost 1000 m of the water column. The limited vertical resolution of Argo floats can underestimate the incidence of these staircases, so a low cost platform with high vertical sampling resolution, such as a glider with a fast thermistor or rapid sampling CTD, could be a promising approach to better quantifying staircases in these regions. The work of van der Boog et al. (2021b) using automated methods to classify staircases, built on in this chapter, could enable identification of thermohaline staircases in already existing glider datasets, and those collected in the future.

EUREC^{4}A was the final deployment of SG637 during this PhD. Had we been able to diagnose and fix the issues with the ADCP beam setup prior to deployment, we could have directly observed velocity shear across thermohaline staircases. It would have been particularly interesting to observe the velocity structure of the front that was observed halfway through SG637's deployment (Figure 3.8). This event was accompanied by a substantial change in dive average currents and followed by the appearance of a strong thermohaline staircase (Figure 3.3 e). The temperature and salinity profiles collected by SG637 were of sufficient quality to enable analysis of thermohaline staircases, even with 6 dives lost to stalling.

In this thesis, I set out to test whether the ADCP glider SG637 could be used to observe currents in the uppermost 1000 m of the ocean. The results of this effort were mixed. Chapter 4 described the various trials, tests and deployments of SG637. This experience highlighted the importance of thorough testing of sensor-platform integrations, especially when they are supplied by different manufacturers. Ultimately, the integration of the ADCP was successful. However, a more cautious approach with thorough bench testing before deployment could have improved the outcomes of Omura's 4 deployments. Had the transducers of Omura been tested following the procedure in Chapter 5 before the EUREC^{4}A campaign, we could have collected an extensive ADCP glider dataset. This experience, along with those of other difficult sensor integrations on gliders, suggest that more end user tests must be performed before extensive operational use is made of novel sensors.

Ultimately, a high quality ADCP dataset was not collected. However, the EUREC^{4}A deployment was useful in testing the ability of SG637 to remain within pitch and roll parameter space required by the AD2CP (Figure 4.6). Pilots were able to constrain the roll and keep the pitch consistent to remain within the 1.0 m beam miss envelope (Figure 4.5). However, even when well trimmed, the glider could not depress its pitch angle shallower than 20 degrees (Figure 4.5 b). When attempting to decrease its pitch, SG637 stalled during 6 dives. This problem could be resolved with a small design change to the

AD2CP transducer face angles, shown in Figure 4.3. If the angle offset of the fore and aft transducers was steepened from 47.5 ° to 54.8 °, the ideal pitch angle of the glider would increase from 17.4 ° to 22 °. These calculations are demonstrated in Appendix A. An ideal pitch of 22 ° would substantially reduce the risk of stalling and decrease the beam miss of the AD2CP, ensuring optimum collection of velocity data. This change to the design of the AD2CP to better match the performance constraints of the glider would avoid lost data, as occurred during the EUREC^{4}A owing to the glider stalling out at low pitch angles. Any angle of glider pitch could be chosen, and the beam angles of the sensor adjusted accordingly. I recommend a pitch of 22 ° as this is a typical pitch angle for a Seaglider, such as Omura, conducting a waypoint based survey such as that completed in EUREC^{4}A. If a glider is intended to occupy a virtual mooring, diving to remain in a fixed location, changing the beam angle to collect optimal data at a steeper pitch angle would be preferable.

SG637 Omura has returned to the NMF equipment pool for use by the UK oceanographic community. Using the experience gained from the trials of Omura detailed in this thesis, a team at SAMS, led by Mark Inall, plan to use SG637 to observe currents across the Rockall Trough, NW of Scotland in Spring 2022. The upper reaches of the Rockall Trough are monitored as part of the Ellet Line, which has been regularly surveyed since 1975 (Holliday and Cunningham, 2013). This is an ideal environment for an ADCP glider. The Rockall Trough hosts strong ageostrophic currents and is a difficult location for traditional moorings, as these are frequently destroyed by commercial trawlers. If successful, the deployment of SG637 to this area could be a blueprint for sustained ADCP glider observations across a North Atlantic shelf-break. The four years since I started my PhD have seen a number of successful integrations and scientific deployments of ADCP gliders, all centred around the Nortek AD2CP (Todd et al. 2017, Jonker et al. 2019, de Fommervault et al. 2019). The work undertaken during this thesis was essential for the testing of the Kongsberg Seaglider and AD2CP integration. Although the deployment record of Omura thus far has been less than perfect, there is a promising career ahead of her. Future integrations of ADCPs into gliders should put more consideration into the handling characteristics of the glider. The beam angle of the Nortek AD2CP which necessitates a pitch angle of 17.4 °is unsuited for a glider which can and does stall at pitch less than 20 °. Additionally, care must be taken by operators to ensure that the manufactures of the glider and ADCP communicate to turn on the correct beams during descent and ascent phases of the dive cycle. ADCP gliders are most useful in regions with substantial ageostrophic currents, such as tidally influenced troughs and shelf breaks where wind influences, tides and upwelling dynamics can be difficult to disentangle.

A common thread that has stood out through these three disparate projects has been the importance of shared data, and the benefits of open source development. One of the most important outcomes of Chapter 2 was the publication of a decade old glider dataset. In the intervening 10 years, no glider deployments have been conducted in this region, and this dataset remains the longest record of continuous cross shelf transects in the NW Iberian margin. Chapter 4 described the difficulty of using a novel sensor-platform integration for which no documentation exists. In an attempt to improve the situation, the techniques developed in Chapter 5 have been archived and made available online, so that future users of SG637 can build on this experience. Chapter 3 was made possible by van der Boog et al. (2021b) openly publishing both their thermohaline staircase dataset and the code used to create it. These three chapters have all contributed to or benefited from, the open sharing of data and processing code.

Sharing of processing code can be as important as sharing data, but is much less common. Authors can improve the accessibility of their code by uploading it to open collaborative platforms such as GitHub, and using free archival services like zenodo. This offers the additional benefit of minting a DOI. With more time and effort, authors can use exclusively open source software, such as Python, R or Julia for their analysis. This improves accessibility be removing financial barriers to reproducing the work. In additional to sharing the code, authors can package their analysis into computational notebooks, as described in Perkel (2018). These notebooks make re-running and changing an analysis much simpler, both for the original author and the wider community. The development of code should be tracked with a version control software such as git, and commented to explain its internal logic (Blischak et al., 2016). With a greater investment of time, authors can work to ensure their code is error-free and reproducible by implementing software tests as part of code development (Crouch, 2021). These best practices, and more, are actively promoted by the UK Software Sustainability Institute (SSI, 2022).

Throughout my thesis I have endeavoured to follow the evolving best practices of open source, as applied to oceanography. Following this methodology, I have published in Open Access journals, archived datasets to BODC (Rollo 2021b , Rollo et al. 2020b) , uploaded my code to collaborative platforms and archived it in long term repositories (Rollo 2020b, Rollo 2021a, Rollo 2021c). I have published my work on SG637 as a cook-book style document that future users of the system can benefit from and add to (Rollo, 2020b). Alongside my PhD, I have worked to improve open source oceanographic tools such as GliderTools (Busecke et al., 2021) and erddapy (Fernandes et al., 2021). These packages, developed as collaborative repositories, enable powerful and efficient analysis of and access to glider data. I believe that these tools and communities have a great potential to

increase the effectiveness of research with ocean gliders.

A

Alternative transducer angles

A.1 Calculations of beam angles, Nortek 1 MHz AD2CP

This appendix is available as a self-describing computational notebook at `https://mybinder.org/v2/gh/callumrollo/ad2cp-angles/HEAD?filepath=AD2CP-angles.ipynb`

When in flight, the glider uses three of the four ADCP transducers. It turns off the aft facing transducer during the descent and the fore facing transducer during the ascent.

The goal is to pitch glider such that the three active transducers are at the same angle from the vertical, so that they use scatterers at the same depth. We define the following equations:

$$\begin{aligned}
\theta_1 &= \arccos(\cos(\vartheta_{fa} - \phi_{pitch})\cos(\phi_{roll})) \\
\theta_2 &= \arccos(\cos(\vartheta_{ps} - \phi_{roll})\cos(\phi_{pitch})) \\
\theta_3 &= \arccos(\cos(\vartheta_{fa} + \phi_{pitch})\cos(\phi_{roll})) \\
\theta_4 &= \arccos(\cos(\vartheta_{ps} + \phi_{roll})\cos(\phi_{pitch}))
\end{aligned} \tag{A.1}$$

Where:

θ_x is the angle between beam x and the vertical.

ϑ_{fa} is the angle of the fore and aft beams from the vertical. Currently 47.5 °.

ϑ_{ps} is the angle of the port and starboard beams from the vertical. Currently 25 °.

ϕ_{roll} and ϕ_{pitch} are roll and pitch of the glider.

This equation set can be formulated as a Python function. Printed angles are rounded to 3 decimal places for readability.

[2]:
```
import numpy as np
def angle_from_vertical(fore_aft_angle=47.5,␣
 ↪port_starboard_angle=25,
                        pitch=0, roll=0):
    """Calculate angles from vertical of the four beams of
     a Nortek AD2CP in Janus configuration.
    Angles supplied and returned are all in degrees."""
    phi_pitch = np.deg2rad(pitch)
    phi_roll = np.deg2rad(roll)
```

```
    angle_fa = np.deg2rad(fore_aft_angle)
    angle_ps = np.deg2rad(port_starboard_angle)
    theta_1 = np.rad2deg(np.arccos(
        np.cos(angle_fa - phi_pitch) * np.cos(phi_roll)))
    theta_2 = np.rad2deg(np.arccos(
        np.cos(angle_ps - phi_roll) * np.cos(phi_pitch)))
    theta_3 = np.rad2deg(np.arccos(
        np.cos(angle_fa + phi_pitch) * np.cos(phi_roll)))
    theta_4 = np.rad2deg(np.arccos(
        np.cos(angle_ps + phi_roll) * np.cos(phi_pitch)))
    print(f"fore angle: {theta_1:.3f}\n"
          f"port angle: {theta_2:.3f}\n"
          f"aft angle: {theta_3:.3f}\n"
          f"stbd angle: {theta_4:.3f}")
    return theta_1, theta_2, theta_3, theta_4
```

A.2 Original configuration

When the glider is pitched and rolled flat, angles from vertical are simply the angles presented in Figure 4.4.

[3]:
```
angle_from_vertical();
```

```
fore angle: 47.500
port angle: 25.000
aft angle: 47.500
stbd angle: 25.000
```

When pitched at 17.4 degrees up or down and rolled flat, the three active beams are at 30.1 degrees from the vertical. When descending (pitch +ve) the aft beam is not used, when ascending (pitch -ve) the forward beam is not used.

[4]:
```
angle_from_vertical(pitch=17.4);
```

```
fore angle: 30.100
port angle: 30.136
aft angle: 64.900
stbd angle: 30.136
```

[5]:
```
angle_from_vertical(pitch=-17.4);
```

```
fore angle: 64.900
```

```
port angle: 30.136
aft angle: 30.100
stbd angle: 30.136
```

A.3 Modified angles

The designed optimum pitch angle of 17.4 ° is not ideal for gliders. Seagliders frequently stall when the pitch angle is decreased below 20 °. Increasing ϑ_{fa} to 54.8 ° would result in a ideal pitch angle of 22 °.

[6]:
```
angle_from_vertical(pitch=22, fore_aft_angle=54.8);
```

```
fore angle: 32.800
port angle: 32.827
aft angle: 76.800
stbd angle: 32.827
```

This could equally be achieved by decreasing ϑ_{ps} to 13.2 °.

[7]:
```
angle_from_vertical(pitch=22, port_starboard_angle=13.2);
```

```
fore angle: 25.500
port angle: 25.487
aft angle: 69.500
stbd angle: 25.487
```

The changes to θ of the three active beams (θ_a) caused by these physical modifications would be modest. Increasing θ_a by 2.7 ° in the former case and decreasing it by 4.5 ° in the latter. If changing θ_a is an issue, it is possible to take a combined approach, steepening both sets of angles to preserve $\theta_a \approx 30.1$ ° while giving an optimal pitch angle of 22 °.

[8]:
```
angle_from_vertical(pitch=22, port_starboard_angle=21.1,␣
↪fore_aft_angle=52.1);
```

```
fore angle: 30.100
port angle: 30.115
aft angle: 74.100
stbd angle: 30.115
```

This suggested change in optimal pitch angle would improve pilotability of AD2CP gliders and the quality of velocity data collected.

Bibliography

Alkire, M. B., D'Asaro, E., Lee, C., Perry, M. J., Gray, A., Cetinić, I., Briggs, N., Rehm, E., Kallin, E., Kaiser, J., and González-Posada, A.: Estimates of net community production and export using high-resolution, Lagrangian measurements of O2, NO3-, and POC through the evolution of a spring diatom bloom in the North Atlantic, Deep Sea Research Part I: Oceanographic Research Papers, 64, 157–174, doi:10.1016/j.dsr.2012.01.012, 2012.

Álvarez-Salgado, X., Castro, C., Pérez, F., and Fraga, F.: Nutrient mineralization patterns in shelf waters of the Western Iberian upwelling, Continental Shelf Research, 17, 1247–1270, doi:10.1016/s0278-4343(97)00014-9, 1997.

Álvarez-Salgado, X., Gago, J., Miguez, B., Gilcoto, M., and Pérez, F.: Surface Waters of the NW Iberian Margin: Upwelling on the Shelf versus Outwelling of Upwelled Waters from the Rías Baixas, Estuarine, Coastal and Shelf Science, 51, 821–837, doi:10.1006/ecss.2000.0714, 2000.

Arístegui, J., Barton, E. D., Álvarez-Salgado, X. A., Santos, A. M. P., Figueiras, F. G., Kifani, S., Hernández-León, S., Mason, E., Machú, E., and Demarcq, H.: Sub-regional ecosystem variability in the Canary Current upwelling, Progress in Oceanography, 83, 33–48, doi:10.1016/j.pocean.2009.07.031, 2009.

Bakun, A.: Coastal upwelling indices, west coast of North America, NOAA Technical Report, URL `https://oceanview.pfeg.noaa.gov/references/Bakun_UI_1973.pdf`, 1973.

Baranowski, D. B.: CTD data RV Meteor, cruise M161 accessed 21/10/2020, URL `https://observations.ipsl.fr/aeris/eurec4a-data/SHIPS/RV-METEOR/CTD`, 2020.

Barnes, S. L.: Applications of the Barnes Objective Analysis Scheme. Part II: Improving Derivative Estimates, Journal of Atmospheric and Oceanic Technology, 11, 1449–1458, doi:10.1175/1520-0426(1994)011<1449:aotboa>2.0.co;2, 1994.

Barton, E.: Canary And Portugal Currents, in: Encyclopedia of Ocean Sciences, pp. 380–389, Elsevier, doi:10.1006/rwos.2001.0360, 2001.

Baumgartner, M. F. and Fratantoni, D. M.: Diel periodicity in both sei whale vocalization rates and the vertical migration of their copepod prey observed from ocean gliders, Limnology and Oceanography, 53, 2197–2209, doi:10.4319/lo.2008.53.5_part_2.2197, 2008.

Blischak, J. D., Davenport, E. R., and Wilson, G.: A Quick Introduction to Version Control with Git and GitHub, PLOS Computational Biology, 12, e1004 668, doi:10.1371/journal.pcbi.1004668, 2016.

Bony, S., Stevens, B., Ament, F., Bigorre, S., Chazette, P., Crewell, S., Delanoë, J., Emanuel, K., Farrell, D., Flamant, C., Gross, S., Hirsch, L., Karstensen, J., Mayer, B., Nuijens, L., Ruppert, J. H., Sandu, I., Siebesma, P., Speich, S., Szczap, F., Totems, J., Vogel, R., Wendisch, M., and Wirth, M.: EUREC4A: A Field Campaign to Elucidate the Couplings Between Clouds, Convection and Circulation, Surveys in Geophysics, 38, 1529–1568, doi:10.1007/s10712-017-9428-0, 2017.

Brenton, B.: Huntington Ingalls Industries Closes the Acquisition of Hydroid Inc. Accessed 30/09/2021, URL `https://newsroom.huntingtoningalls.com/releases/huntington-ingalls-industries-closes-the-acquisition-of-hydroid-inc`, 2020.

Brink, K. H.: The Sea, Vol. 10: The Global Coastal Ocean, John Wiley and Sons, 1998.

Brown, C. W.: Seaglider observations of biogeochemical variability in the Iberian Upwelling System, Ph.D. thesis, School of Envrionmental Sciences, University of East Anglia, URL `https://ueaeprints.uea.ac.uk/48788/`, 2013.

Bryden, H. L., Schroeder, K., Sparnocchia, S., Borghini, M., and Vetrano, A.: Thermohaline staircases in the western Mediterranean Sea, Journal of Marine Research, 72, 1–18, doi:10.1357/002224014812655198, 2014.

Buckley, M. W. and Marshall, J.: Observations, inferences, and mechanisms of the Atlantic Meridional Overturning Circulation: A review, Reviews of Geophysics, 54, 5–63, doi:10.1002/2015rg000493, 2016.

Buffett, G. G., Krahmann, G., Klaeschen, D., Schroeder, K., Sallarès, V., Papenberg, C., Ranero, C. R., and Zitellini, N.: Seismic Oceanography in the Tyrrhenian Sea: Thermohaline Staircases, Eddies, and Internal Waves, Journal of Geophysical Research: Oceans, 122, 8503–8523, doi:https://doi.org/10.1002/2017JC012726, _eprint:

https://agupubs.onlinelibrary.wiley.com/doi/pdf/10.1002/2017JC012726, 2017.

Busecke, J., Gregor, L., Balwada, D., Thomsen, S., Giddy, I. S., Rollo, C., and Ryan-Keogh, T. J.: GliderToolsCommunity/GliderTools: v2021.05.26, doi:10.5281/zenodo.4815417, 2021.

Cauchy, P., Heywood, K. J., Merchant, N. D., Queste, B. Y., and Testor, P.: Wind Speed Measured from Underwater Gliders Using Passive Acoustics, Journal of Atmospheric and Oceanic Technology, 35, 2305–2321, doi:10.1175/jtech-d-17-0209.1, 2018.

Cetinić, I., Perry, M. J., D'saro, E., Briggs, N., Poulton, N., Sieracki, M. E., and Lee, C. M.: A simple optical index shows spatial and temporal heterogeneity in phytoplankton community composition during the 2008 North Atlantic Bloom Experiment, Biogeosciences, 12, 2179–2194, doi:10.5194/bg-12-2179-2015, 2015.

Copernicus Climate Change Service (C3S): ERA5: Fifth generation of ECMWF atmospheric reanalyses of the global climate accessed 29/05/2019, URL `https://cds.climate.copernicus.eu`, 2017.

Crouch, S.: Testing your software. Accessed 28/05/2022, URL `https://www.software.ac.uk/resources/guides/testing-your-software`, 2021.

Cusi, S., Rodriguez, P., Pujol, N., Pairaud, I., Nogueras, M., Antonijuan, J., Masmitja, I., and del Rio, J.: Evaluation of AUV-borne ADCP measurements in different navigation modes, in: OCEANS 2017 - Aberdeen, IEEE, doi:10.1109/oceanse.2017.8084688, 2017.

Damerell, G. M., Heywood, K. J., Thompson, A. F., Binetti, U., and Kaiser, J.: The vertical structure of upper ocean variability at the Porcupine Abyssal Plain during 2012-2013, Journal of Geophysical Research: Oceans, 121, 3075–3089, doi:10.1002/2015jc011423, 2016.

Davis, R. E.: On the coastal-upwelling overturning cell, Journal of Marine Research, 68, 369–385, doi:10.1357/002224010794657173, 2010.

de Fommervault, O., Besson, F., Beguery, L., Le Page, Y., and Lattes, P.: SeaExplorer Underwater Glider: A New Tool to Measure depth-resolved water currents profiles, in: OCEANS 2019 - Marseille, pp. 1–6, doi:10.1109/OCEANSE.2019.8867228, 2019.

Duncombe, J.: NOAA Monitoring Stations Are Off-Line from a GPS Y2K Moment, Eos, 100, doi:10.1029/2019eo120511, 2019.

Durante, S., Schroeder, K., Mazzei, L., Pierini, S., Borghini, M., and Sparnocchia, S.: Permanent Thermohaline Staircases in the Tyrrhenian Sea, Geophysical Research Letters, 46, 1562–1570, doi:https://doi.org/10.1029/2018GL081747, _eprint: https://agupubs.onlinelibrary.wiley.com/doi/pdf/10.1029/2018GL081747, 2019.

Egbert, G. D. and Erofeeva, S. Y.: Efficient Inverse Modeling of Barotropic Ocean Tides, Journal of Atmospheric and Oceanic Technology, 19, 183–204, doi:10.1175/1520-0426(2002)019<0183:eimobo>2.0.co;2, 2002.

Ellis, D., Washburn, L., Ohlmann, C., and Gotschalk, C.: Improved Methods to Calculate Depth-Resolved Velocities from Glider-Mounted ADCPs, in: Currents, Waves and Turbulence Measurement (CWTM), IEE/OES 11th, St Petersburg, FL, USA, doi:10.1109/CWTM.2015.7098120, 2015.

Elson, P., de Andrade, E. S., Hattersley, R., Campbell, E., May, R., Dawson, A., Raynaud, S., Greg, scmc72, Little, B., Donkers, K., Blay, B., Killick, P., marqh, lbdreyer, Peglar, P., Wilson, N., Szymaniak, J., Andrew, Filipe, Bosley, C., Kirkham, D., Bradbury, M., Signell, J., Wieczorek, M., Krischer, L., van Kemenade, H., htonchia, Eriksson, D., and Smith, A.: SciTools/cartopy: Cartopy 0.18.0, doi:10.5281/zenodo.3783894, 2020.

EMODnet Bathymetry Consortium: EMODnet Digital Bathymetry (DTM 2018), doi:10.12770/18ff0d48-b203-4a65-94a9-5fd8b0ec35f6, 2018.

Eriksen, C., Osse, T., Light, R., Wen, T., Lehman, T., Sabin, P., Ballard, J., and Chiodi, A.: Seaglider: a long-range autonomous underwater vehicle for oceanographic research, IEEE Journal of Oceanic Engineering, 26, 424–436, doi:10.1109/48.972073, 2001.

Fer, I., Nandi, P., Holbrook, W. S., Schmitt, R. W., and Páramo, P.: Seismic imaging of a thermohaline staircase in the western tropical North Atlantic, Ocean Science, 6, 621–631, doi:10.5194/os-6-621-2010, publisher: Copernicus GmbH, 2010.

Fer, I., Peterson, A. K., and Ullgren, J. E.: Microstructure Measurements from an Underwater Glider in the Turbulent Faroe Bank Channel Overflow, Journal of Atmospheric and Oceanic Technology, 31, 1128–1150, doi:10.1175/jtech-d-13-00221.1, 2014.

Fernandes, F., Rollo, C., Signell, R., Kingston, Thomas, Kerney, A., Salazar, V., Fratantonio, B., Munroe, J., and Do, V.: ioos/erddapy: v1.1.0, doi:10.5281/zenodo.5138115, 2021.

Ferreira Cordeiro, N. G.: Numerical and observational processes study of Northwestern Iberian margin circulation, Ph.D. thesis, Departamento de Fisica, Universidade de Aveiro, URL `https://digital.csic.es/`, 2018.

Ferreira Cordeiro, N. G., Dubert, J., Nolasco, R., and Barton, E. D.: Transient response of the Northwestern Iberian upwelling regime, PLOS ONE, 13, doi:10.1371/journal.pone.0197627, 2018.

Fiuza, A. F., Hamann, M., Ambar, I., del Rio, G. D., Gonzalez, N., and Cabanas, J. M.: Water masses and their circulation off western Iberia during May 1993, Deep Sea Research Part I: Oceanographic Research Papers, 45, 1127–1160, doi:10.1016/s0967-0637(98)00008-9, 1998.

Flanagan, T.: pynmea2, python library for the NMEA 0183 protocol, URL `https://github.com/Knio/pynmea2`, 2016.

Fong, D. A. and Monismith, S.: Evaluation of the Accuracy of a Ship-Mounted, Bottom-Tracking ADCP in a Near-Shore Coastal Flow, Journal of Atmospheric and Oceanic Technology, 21, 1121–1128, 2004.

Frajka-Williams, E., Eriksen, C. C., Rhines, P. B., and Harcourt, R. R.: Determining Vertical Water Velocities from Seaglider, Journal of Atmospheric and Oceanic Technology, 28, 1641–1656, doi:10.1175/2011jtecho830.1, 2011.

Garau, B., Ruiz, S., Zhang, W. G., Pascual, A., Heslop, E., Kerfoot, J., and Tintoré, J.: Thermal Lag Correction on Slocum CTD Glider Data, Journal of Atmospheric and Oceanic Technology, 28, 1065–1071, doi:10.1175/jtech-d-10-05030.1, 2011.

Garcia, H. E. and Gordon, L. I.: Oxygen solubility in seawater: Better fitting equations, Limnology and Oceanography, 37, 1307–1312, doi:10.4319/lo.1992.37.6.1307, 1992.

Garcia, H. E. and Gordon, L. I.: Erratum: Oxygen solubility in seawater: Better fitting equations, Limnology and Oceanography, 38, 656, 1993.

Guizzo, E.: Defense Contractors Snap Up Submersible Robot Gliders. Accessed 30/09/2021, URL `https://spectrum.ieee.org/defense-contractors-snap-up-submersible-robot-gliders`, 2008.

Hall, R. A., Aslam, T., and Huvenne, V. A.: Partly standing internal tides in a dendritic submarine canyon observed by an ocean glider, Deep Sea Research Part I: Oceanographic Research Papers, 126, 73–84, doi:10.1016/j.dsr.2017.05.015, 2017.

Harris, C. R., Millman, K. J., van der Walt, S. J., Gommers, R., Virtanen, P., Cournapeau, D., Wieser, E., Taylor, J., Berg, S., Smith, N. J., Kern, R., Picus, M., Hoyer, S., van Kerkwijk, M. H., Brett, M., Haldane, A., del Río, J. F., Wiebe, M., Peterson, P., Gérard-Marchant, P., Sheppard, K., Reddy, T., Weckesser, W., Abbasi, H., Gohlke, C., and Oliphant, T. E.: Array programming with NumPy, Nature, 585, 357–362, doi:10.1038/s41586-020-2649-2, 2020.

Herrera, J., Rosón, G., Varela, R., and Piedracoba, S.: Variability of the western Galician upwelling system (NW Spain) during an intensively sampled annual cycle. An EOF analysis approach, Journal of Marine Systems, 72, 200–217, doi:10.1016/j.jmarsys.2007.07.007, 2008.

Holliday, P. and Cunningham, S.: The Extended Ellett Line: Discoveries From 65 Years of Marine Observations West of the UK, Oceanography, 26, doi:10.5670/oceanog.2013.17, 2013.

Hu, C., Lee, Z., and Franz, B.: Chlorophyll a algorithms for oligotrophic oceans: A novel approach based on three-band reflectance difference, Journal of Geophysical Research: Oceans, 117, doi:10.1029/2011jc007395, 2012.

Humon, J.: University of Hawaii Data Acquisition System, URL `https://currents.soest.hawaii.edu/docs/adcp_doc/index.html`, 2021.

Hunter, J. D.: Matplotlib: A 2D Graphics Environment, Computing in Science & Engineering, 9, 90–95, doi:10.1109/mcse.2007.55, 2007.

Huthnance, J. M., Aken, H. M. V., White, M., Barton, E., Cann, B. L., Coelho, E. F., Fanjul, E. A., Miller, P., and Vitorino, J.: Ocean margin exchange—water flux estimates, Journal of Marine Systems, 32, 107–137, doi:10.1016/s0924-7963(02)00034-9, 2002.

IOC, S. and IAPSO: The international thermodynamic equation of seawater – 2010: Calculation and use of thermodynamic properties., Intergovernmental Oceanographic Commission, Manuals and Guides no. 56, 2010.

IRobot: Seaglider 1KA User Guide, Revision D., Seattle, USA, 2012.

Johnston, T. M. S., Rudnick, D. L., Alford, M. H., Pickering, A., and Simmons, H. L.: Internal tidal energy fluxes in the South China Sea from density and velocity measurements by gliders, Journal of Geophysical Research: Oceans, 118, 3939–3949, doi:10.1002/jgrc.20311, 2013.

Joint, I., Groom, S. B., Wollast, R., Chou, L., Tilstone, G. H., Figueiras, F. G., Loijens, M., and Smyth, T. J.: The response of phytoplankton production to periodic upwelling and relaxation events at the Iberian shelf break: estimates

by the 14C method and by satellite remote sensing, Journal of Marine Systems, 32, 219–238, doi:10.1016/s0924-7963(02)00037-4, 2002.

Jonker, J., Shcherbina, A., Krishfield, R., Van Uffelen, L., Aravkin, A., and Webster, S. E.: Preliminary Results in Current Profile Estimation and Doppler-aided Navigation for Autonomous Underwater Gliders, in: OCEANS 2019 - Marseille, pp. 1–8, doi:10.1109/OCEANSE.2019.8867108, 2019.

Kierstead, E.: KONGSBERG's Seaglider® Autonomous Underwater Vehicle Division Transferred to Hydroid. Accessed 30/09/2021, URL `https://www.prnewswire.com/news-releases/kongsbergs-seaglider-autonomous-underwater-vehicle-division-transferred-to-hydroid-300949524.html`, 2019.

Kluyver, T., Ragan-Kelley, B., Pérez, F., Granger, B., Bussonnier, M., Frederic, J., Kelley, K., Hamrick, J., Grout, J., Corlay, S., Ivanov, P., Avila, D., Abdalla, S., and Willing, C.: Jupyter Notebooks – a publishing format for reproducible computational workflows, in: Positioning and Power in Academic Publishing: Players, Agents and Agendas, edited by Loizides, F. and Schmidt, B., pp. 87 – 90, IOS Press, 2016.

Kongsberg: KONGSBERG Obtains Rights to Commercialize Seaglider™ Technology . Accessed 30/09/2021, URL `https://www.kongsberg.com/maritime/about-us/news-and-media/news-archive/2013/kongsberg-obtains-rights-to-commercialize-seaglider-technology?OpenDocument`, 2013.

Kuhlbrodt, T., Griesel, A., Montoya, M., Levermann, A., Hofmann, M., and Rahmstorf, S.: On the driving processes of the Atlantic meridional overturning circulation, Reviews of Geophysics, 45, doi:10.1029/2004rg000166, 2007.

Kölling, T. and Rollo, C.: MQTT Dashboard for live data during EUREC4A, URL `https://github.com/eurec4a/mqtt_dashboard`, 2020.

Marmorino, G. O., Brown, W. K., and Morris, W. D.: Two-dimensional temperature structure in the C-SALT thermohaline staircase, Deep Sea Research Part A. Oceanographic Research Papers, 34, 1667–1676, doi:10.1016/0198-0149(87)90015-X, 1987.

Maxwell, K. and Johnson, G. N.: Chlorophyll fluorescence—a practical guide, Journal of Experimental Botany, 51, 659–668, doi:10.1093/jexbot/51.345.659, 2000.

McClain, C. R., Chao, S.-Y., Atkinson, L. P., Blanton, J. O., and Castillejo, F. D.: Wind-driven upwelling in the vicinity of Cape Finisterre, Spain, Journal of Geophysical Research, 91, 8470, doi:10.1029/jc091ic07p08470, 1986.

Mcdougall, T., Feistel, R., Millero, F., Jackett, D. R., Wright, D., King, B., Marion, G., Chen, C.-T. A., and Spitzer, P.: The International Thermodynamic Equation of Seawater 2010 (TEOS-10): Calculation and Use of Thermodynamic Properties, CSIRO Marine and Atmospheric Research Hobart, Tas, 2010.

McDougall, T. J., Barker, P. M., and CSIRO.: Getting started with TEOS-10 and the Gibbs Seawater (GSW) Oceanographic Toolbox : version 3.0 / Trevor J. McDougall and Paul M. Barker, CSIRO Marine and Atmospheric Research Hobart, Tas, 2011.

McKinney, W.: Data Structures for Statistical Computing in Python, in: Proceedings of the 9th Python in Science Conference, edited by Stéfan van der Walt and Jarrod Millman, pp. 56 – 61, doi:10.25080/Majora-92bf1922-00a, 2010.

McPhail, S., Templeton, R., Pebody, M., Roper, D., and Morrison, R.: Autosub Long Range AUV Missions Under the Filchner and Ronne Ice Shelves in the Weddell Sea, Antarctica - an Engineering Perspective, in: OCEANS 2019 - Marseille, IEEE, doi:10.1109/oceanse.2019.8867206, 2019.

Medagoda, L., Jakuba, M. V., Pizarro, O., and Williams, S. B.: Water column current profile aided localisation for Autonomous Underwater Vehicles, in: OCEANS'10 IEEE SYDNEY, pp. 1–10, doi:10.1109/OCEANSSYD.2010.5604016, 2010.

Merckelbach, L. M., Briggs, R. D., Smeed, D. A., and Griffiths, G.: Current measurements from autonomous underwater gliders, in: 2008 IEEE/OES 9th Working Conference on Current Measurement Technology, IEEE, doi:10.1109/ccm.2008.4480845, 2008.

NOAA: Argo Program Achieves Milestone with Two Million Ocean Measurements. Accessed 28/05/2022, URL `https://research.noaa.gov/article/ArtMID/587/ArticleID/2398`, 2018.

Nolasco, R., Pires, A. C., Cordeiro, N., Cann, B. L., and Dubert, J.: A high-resolution modeling study of the Western Iberian Margin mean and seasonal upper ocean circulation, Ocean Dynamics, 63, 1041–1062, doi:10.1007/s10236-013-0647-8, 2013.

Nortek Group: Integrator's Guide AD2CP N3015-007, Vangkroken, Norway, 2017a.

Nortek Group: Signature Operations AD2CP N3015-002, Vangkroken, Norway, 2017b.

Ordonez, C. E., Shearman, R. K., Barth, J. A., Welch, P., Erofeev, A., and Kurokawa, Z.: Obtaining absolute water velocity profiles from glider-mounted Acoustic Doppler Current Profilers, in: 2012 Oceans - Yeosu, IEEE, doi:10.1109/oceans-yeosu.2012.6263582, 2012.

Oschlies, A., Dietze, H., and Kähler, P.: Salt-finger driven enhancement of upper ocean nutrient supply, Geophysical Research Letters, 30, doi:https://doi.org/10.1029/2003GL018552, 2003.

Palmer, M., Stephenson, G., Inall, M., Balfour, C., Düsterhus, A., and Green, J.: Turbulence and mixing by internal waves in the Celtic Sea determined from ocean glider microstructure measurements, Journal of Marine Systems, 144, 57–69, doi:10.1016/j.jmarsys.2014.11.005, 2015.

Pauly, D. and Christensen, V.: Primary production required to sustain global fisheries, Nature, 374, 255–257, doi:10.1038/374255a0, 1995.

Peliz, Á.: Generation and unstable evolution of a density-driven Eastern Poleward Current: The Iberian Poleward Current, Journal of Geophysical Research, 108, doi:10.1029/2002jc001443, 2003.

Peliz, Á., Rosa, T. L., Santos, A. P., and Pissarra, J. L.: Fronts, jets, and counter-flows in the Western Iberian upwelling system, Journal of Marine Systems, 35, 61–77, doi:10.1016/s0924-7963(02)00076-3, 2002.

Perkel, J. M.: Why Jupyter is data scientists' computational notebook of choice, Nature, 563, 145–146, doi:10.1038/d41586-018-07196-1, 2018.

Phillips, A. B., Kingsland, M., Linton, N., Baker, W., Bowring, L., Soper, S., Johnson, D. T. R. A., Morrison, R., Ciaramella, K., Matterson, D., Pebody, M., Marlow, R., Consensi, A., Williams, V., Fanelli, F., Fenucci, D., Martin, A., and O'Hobain, E.: Autosub 2000 Under Ice: Design of a New Work Class AUV for Under Ice Exploration, in: 2020 IEEE/OES Autonomous Underwater Vehicles Symposium (AUV)(50043), IEEE, doi:10.1109/auv50043.2020.9267952, 2020.

Pietri, A., Testor, P., Echevin, V., Chaigneau, A., Mortier, L., Eldin, G., and Grados, C.: Finescale Vertical Structure of the Upwelling System off Southern Peru as Observed from Glider Data, Journal of Physical Oceanography, 43, 631–646, doi:10.1175/jpo-d-12-035.1, 2013.

Puertos del Estado: Upwelling Index, Rias Baixes accessed 22/01/2019, URL `http://www.indicedeafloramiento.ieo.es/HBaixas/uitimeseries.ui`, 2019.

Quaresma, L. S. and Pichon, A.: Modelling the barotropic tide along the West-Iberian margin, Journal of Marine Systems, 109-110, S3–S25, doi:10.1016/j.jmarsys.2011.09.016, 2013.

Queste, B.: Hydrographic observations of oxygen and related physical variables in the North Sea and western Ross Sea Polynya. Ph.D. thesis., Ph.D. thesis, School of Envrionmental Sciences, University of East Anglia, URL `https://ueaeprints.uea.ac.uk/48678/`, 2014.

Radko, T.: What determines the thickness of layers in a thermohaline staircase?, Journal of Fluid Mechanics, 523, 79–98, doi:10.1017/S0022112004002290, 2005.

Radko, T.: Suppression of internal waves by thermohaline staircases, Journal of Fluid Mechanics, 902, doi:10.1017/jfm.2020.563, 2020.

Radko, T. and Smith, D. P.: Equilibrium transport in double-diffusive convection, Journal of Fluid Mechanics, 692, 5–27, doi:10.1017/jfm.2011.343, 2011.

Relvas, P., Barton, E., Dubert, J., Oliveira, P. B., Peliz, Á., da Silva, J., and Santos, A. M. P.: Physical oceanography of the western Iberia ecosystem: Latest views and challenges, Progress in Oceanography, 74, 149–173, doi:10.1016/j.pocean.2007.04.021, 2007.

Ríos, A. F., Pérez, F. F., and Fraga, F.: Water masses in the upper and middle North Atlantic Ocean east of the Azores, Deep Sea Research Part A. Oceanographic Research Papers, 39, 645–658, doi:10.1016/0198-0149(92)90093-9, 1992.

Rollo, C.: adcp-glider-guide: A user guide to the Seaglider-1 MHz AD2CP integration. First public release v1.0, doi:10.5281/zenodo.4147102, 2020a.

Rollo, C.: adcp-glider: Python routines for processing data from an AD2CP Seaglider. Pre-release v0.2-alpha, doi:10.5281/zenodo.4147304, 2020b.

Rollo, C.: Thermohaline staircase classifier, doi:10.5281/zenodo.5541660, 2021a.

Rollo, C.: Physical and biogeochemical data from three Seagliders on a combination transect and virtual mooring deployment, NE of Barbados January - February 2020., doi:10.5285/C596CDD7-C709-461A-E053-6C86ABC0C127, 2021b.

Rollo, C.: MQTT scripts for UEA platforms contributing to the EUREC4A field campaign, doi:10.5281/zenodo.5524750, 2021c.

Rollo, C., Heywood, K. J., Hall, R. A., Barton, E. D., and Kaiser, J.: Glider Observations of the Northwestern Iberian Margin During an Exceptional

Summer Upwelling Season, Journal of Geophysical Research: Oceans, 125, doi:10.1029/2019jc015804, 2020a.

Rollo, C., Heywood, K. J., Hall, R. A., and Kaiser, J.: Physical and biogeochemical data from a Seaglider on an Eastwesterly transect across the shelfbreak on the Northwest Iberian margin from June - August 2010., doi:10.5285/9b3b453b-2afb-0abd-e053-6c86abc0a59c, 2020b.

Rossi, V., Garçon, V., Tassel, J., Romagnan, J.-B., Stemmann, L., Jourdin, F., Morin, P., and Morel, Y.: Cross-shelf variability in the Iberian Peninsula Upwelling System: Impact of a mesoscale filament, Continental Shelf Research, 59, 97–114, doi:10.1016/j.csr.2013.04.008, 2013.

Ruddick, B.: A practical indicator of the stability of the water column to double-diffusive activity, Deep Sea Research Part A. Oceanographic Research Papers, 30, 1105–1107, doi:10.1016/0198-0149(83)90063-8, 1983.

Rudnick, D. L., Zaba, K. D., Todd, R. E., and Davis, R. E.: A climatology of the California Current System from a network of underwater gliders, Progress in Oceanography, 154, 64–106, doi:https://doi.org/10.1016/j.pocean.2017.03.002, 2017.

Rusello, P. J., Yahnker, C., and Morris, M.: Improving depth averaged velocity measurements from Seaglider with an advanced acoustic current profiler, the Nortek AD2CP-Glider, in: 2012 Oceans, pp. 1–8, doi:10.1109/OCEANS.2012.6404897, 2012.

Schlitzer, R.: Ocean Data View. Accesed 10/06/2020, URL `https://odv.awi.de`, 2020.

Schmitt, R.: The Caribbean Sheets and Layers Transects (C-SALT) Program, Eos, Transactions American Geophysical Union, 68, 57–60, 1987.

Schmitt, R. W.: Form of the Temperature-Salinity Relationship in the Central Water: Evidence for Double-Diffusive Mixing, Journal of Physical Oceanography, 11, 1015–1026, doi:10.1175/1520-0485(1981)011<1015:fottsr>2.0.co;2, 1981.

Schmitt, R. W., Perkins, H., Boyd, J. D., and Stalcup, M. C.: C-SALT: An investigation of the thermohaline staircase in the western tropical North Atlantic, Deep Sea Research Part A. Oceanographic Research Papers, 34, 1655–1665, doi:10.1016/0198-0149(87)90014-8, 1987.

Schmitt, R. W., Ledwell, J. R., Montgomery, E. T., Polzin, K. L., and Toole, J. M.: Enhanced Diapycnal Mixing by Salt Fingers in the Thermocline of the Tropical Atlantic, Science, 308, 685–688, doi:10.1126/science.1108678, 2005.

Seaglider: Seaglider Piloting Tools Rev. G, Kongsberg Underwater Technology, Inc., Lynnwood, USA, 2016a.

Seaglider: Seaglider Logdev User Guide Rev. G, Kongsberg Underwater Technology, Inc., Lynnwood, USA, 2016b.

Sheehan, P. M. F., Berx, B., Gallego, A., Hall, R. A., Heywood, K. J., Hughes, S. L., and Queste, B. Y.: Shelf sea tidal currents and mixing fronts determined from ocean glider observations, Ocean Science, 14, 225–236, doi:10.5194/os-14-225-2018, 2018.

Shibley, N. C., Timmermans, M.-L., Carpenter, J. R., and Toole, J. M.: Spatial variability of the Arctic Ocean's double-diffusive staircase, Journal of Geophysical Research: Oceans, 122, 980–994, doi:10.1002/2016jc012419, 2017.

Shumuk, D., Michael, B., Velasco, D., and Douglas Wilson, W.: The Next Generation of Buoys Integrated with Current Profilers, in: OCEANS 2018 MTS/IEEE Charleston, pp. 1–6, doi:10.1109/OCEANS.2018.8604792, 2018.

Siddle, E., Heywood, K. J., Webber, B. G. M., and Bromley, P.: First measurements of ocean and atmosphere in the Tropical North Atlantic using Caravela , a novel uncrewed surface vessel, Weather, 76, 200–204, doi:10.1002/wea.4004, 2021.

Smeed, D. A., McCarthy, G. D., Cunningham, S. A., Frajka-Williams, E., Rayner, D., Johns, W. E., Meinen, C. S., Baringer, M. O., Moat, B. I., Duchez, A., and Bryden, H. L.: Observed decline of the Atlantic meridional overturning circulation 2004-2012, Ocean Science, 10, 29–38, doi:10.5194/os-10-29-2014, 2014.

SSI: Software Sustainability Institute website. Accessed 28/05/2022, URL `https://www.software.ac.uk`, 2022.

Stanway, M. J.: Water profile navigation with an Acoustic Doppler Current Profiler, in: OCEANS'10 IEEE SYDNEY, pp. 1–5, doi:10.1109/OCEANSSYD.2010.5603647, 2010.

Stern, M. E.: The "Salt-Fountain" and Thermohaline Convection, Tellus, 12, 172–175, doi:10.3402/tellusa.v12i2.9378, 1960.

Stevens, B., Bony, S., Farrell, D., Ament, F., Blyth, A., Fairall, C., Karstensen, J., Quinn, P. K., Speich, S., Acquistapace, C., Aemisegger, F., Albright, A. L., Bellenger, H., Bodenschatz, E., Caesar, K.-A., Chewitt-Lucas, R., de Boer, G., Delanoë, J., Denby, L., Ewald, F., Fildier, B., Forde, M., George, G., Gross, S., Hagen, M., Hausold, A., Heywood, K. J., Hirsch, L., Jacob, M., Jansen, F., Kinne, S., Klocke, D., Kölling, T., Konow, H., Lothon, M., Mohr, W.,

Naumann, A. K., Nuijens, L., Olivier, L., Pincus, R., Pöhlker, M., Reverdin, G., Roberts, G., Schnitt, S., Schulz, H., Siebesma, A. P., Stephan, C. C., Sullivan, P., Touzé-Peiffer, L., Vial, J., Vogel, R., Zuidema, P., Alexander, N., Alves, L., Arixi, S., Asmath, H., Bagheri, G., Baier, K., Bailey, A., Baranowski, D., Baron, A., Barrau, S., Barrett, P. A., Batier, F., Behrendt, A., Bendinger, A., Beucher, F., Bigorre, S., Blades, E., Blossey, P., Bock, O., Böing, S., Bosser, P., Bourras, D., Bouruet-Aubertot, P., Bower, K., Branellec, P., Branger, H., Brennek, M., Brewer, A., Brilouet, P.-E., Brügmann, B., Buehler, S. A., Burke, E., Burton, R., Calmer, R., Canonici, J.-C., Carton, X., Cato Jr., G., Charles, J. A., Chazette, P., Chen, Y., Chilinski, M. T., Choularton, T., Chuang, P., Clarke, S., Coe, H., Cornet, C., Coutris, P., Couvreux, F., Crewell, S., Cronin, T., Cui, Z., Cuypers, Y., Daley, A., Damerell, G. M., Dauhut, T., Deneke, H., Desbios, J.-P., Dörner, S., Donner, S., Douet, V., Drushka, K., Dütsch, M., Ehrlich, A., Emanuel, K., Emmanouilidis, A., Etienne, J.-C., Etienne-Leblanc, S., Faure, G., Feingold, G., Ferrero, L., Fix, A., Flamant, C., Flatau, P. J., Foltz, G. R., Forster, L., Furtuna, I., Gadian, A., Galewsky, J., Gallagher, M., Gallimore, P., Gaston, C., Gentemann, C., Geyskens, N., Giez, A., Gollop, J., Gouirand, I., Gourbeyre, C., de Graaf, D., de Groot, G. E., Grosz, R., Güttler, J., Gutleben, M., Hall, K., Harris, G., Helfer, K. C., Henze, D., Herbert, C., Holanda, B., Ibanez-Landeta, A., Intrieri, J., Iyer, S., Julien, F., Kalesse, H., Kazil, J., Kellman, A., Kidane, A. T., Kirchner, U., Klingebiel, M., Körner, M., Kremper, L. A., Kretzschmar, J., Krüger, O., Kumala, W., Kurz, A., L'Hégaret, P., Labaste, M., Lachlan-Cope, T., Laing, A., Landschützer, P., Lang, T., Lange, D., Lange, I., Laplace, C., Lavik, G., Laxenaire, R., Le Bihan, C., Leandro, M., Lefevre, N., Lena, M., Lenschow, D., Li, Q., Lloyd, G., Los, S., Losi, N., Lovell, O., Luneau, C., Makuch, P., Malinowski, S., Manta, G., Marinou, E., Marsden, N., Masson, S., Maury, N., Mayer, B., Mayers-Als, M., Mazel, C., McGeary, W., McWilliams, J. C., Mech, M., Mehlmann, M., Meroni, A. N., Mieslinger, T., Minikin, A., Minnett, P., Möller, G., Morfa Avalos, Y., Muller, C., Musat, I., Napoli, A., Neuberger, A., Noisel, C., Noone, D., Nordsiek, F., Nowak, J. L., Oswald, L., Parker, D. J., Peck, C., Person, R., Philippi, M., Plueddemann, A., Pöhlker, C., Pörtge, V., Pöschl, U., Pologne, L., Posyniak, M., Prange, M., Quiñones Meléndez, E., Radtke, J., Ramage, K., Reimann, J., Renault, L., Reus, K., Reyes, A., Ribbe, J., Ringel, M., Ritschel, M., Rocha, C. B., Rochetin, N., Röttenbacher, J., Rollo, C., Royer, H., Sadoulet, P., Saffin, L., Sandiford, S., Sandu, I., Schäfer, M., Schemann, V., Schirmacher, I., Schlenczek, O., Schmidt, J., Schröder, M., Schwarzenboeck, A., Sealy, A., Senff, C. J., Serikov, I., Shohan, S., Siddle, E., Smirnov, A., Späth, F., Spooner, B., Stolla, M. K., Szkółka, W., de Szoeke, S. P., Tarot, S., Tetoni, E., Thompson, E., Thomson, J., Tomassini, L., Totems, J., Ubele, A. A., Villiger, L., von Arx, J., Wagner, T., Walther, A., Webber, B., Wendisch,

M., Whitehall, S., Wiltshire, A., Wing, A. A., Wirth, M., Wiskandt, J., Wolf, K., Worbes, L., Wright, E., Wulfmeyer, V., Young, S., Zhang, C., Zhang, D., Ziemen, F., Zinner, T., and Zöger, M.: EUREC^{4}A, Earth System Science Data Discussions, pp. 1–78, doi:10.5194/essd-2021-18, 2021.

Szuts, Z. B., Bower, A. S., Donohue, K. A., Girton, J. B., Hummon, J. M., Katsumata, K., Lumpkin, R., Ortner, P. B., Phillips, H. E., Rossby, H. T., Shay, L. K., Sun, C., and Todd, R. E.: The Scientific and Societal Uses of Global Measurements of Subsurface Velocity, Frontiers in Marine Science, 6, doi:10.3389/fmars.2019.00358, 2019.

Teledyne RD Instruments: Acoustic Doppler Current Profiler Principles of Operation A Practical Primer. Accessed 20/07/2021, Poway, California USA, URL `http://www.teledynemarine.com/Documents/Brand%20Support/RD%20INSTRUMENTS-Technical%20Resources/Manuals%20and%20Guides/General%20Interest/BBPRIME.pdf`, 2011.

Teles-Machado, A., Peliz, Á., McWilliams, J. C., Couvelard, X., and Ambar, I.: Circulation on the Northwestern Iberian Margin: Vertical structure and seasonality of the alongshore flows, Progress in Oceanography, 140, 134–153, doi:10.1016/j.pocean.2015.05.021, 2015.

Testor, P., de Young, B., Rudnick, D. L., Glenn, S., Hayes, D., Lee, C. M., Pattiaratchi, C., Hill, K., Heslop, E., Turpin, V., Alenius, P., Barrera, C., Barth, J. A., Beaird, N., Bécu, G., Bosse, A., Bourrin, F., Brearley, J. A., Chao, Y., Chen, S., Chiggiato, J., Coppola, L., Crout, R., Cummings, J., Curry, B., Curry, R., Davis, R., Desai, K., DiMarco, S., Edwards, C., Fielding, S., Fer, I., Frajka-Williams, E., Gildor, H., Goni, G., Gutierrez, D., Haugan, P., Hebert, D., Heiderich, J., Henson, S., Heywood, K., Hogan, P., Houpert, L., Huh, S., Inall, M. E., Ishii, M., ichi Ito, S., Itoh, S., Jan, S., Kaiser, J., Karstensen, J., Kirkpatrick, B., Klymak, J., Kohut, J., Krahmann, G., Krug, M., McClatchie, S., Marin, F., Mauri, E., Mehra, A., Meredith, M. P., Meunier, T., Miles, T., Morell, J. M., Mortier, L., Nicholson, S., O'Callaghan, J., O'Conchubhair, D., Oke, P., Pallàs-Sanz, E., Palmer, M., Park, J., Perivoliotis, L., Poulain, P.-M., Perry, R., Queste, B., Rainville, L., Rehm, E., Roughan, M., Rome, N., Ross, T., Ruiz, S., Saba, G., Schaeffer, A., Schönau, M., Schroeder, K., Shimizu, Y., Sloyan, B. M., Smeed, D., Snowden, D., Song, Y., Swart, S., Tenreiro, M., Thompson, A., Tintore, J., Todd, R. E., Toro, C., Venables, H., Wagawa, T., Waterman, S., Watlington, R. A., and Wilson, D.: OceanGliders: A Component of the Integrated GOOS, Frontiers in Marine Science, 6, doi:10.3389/fmars.2019.00422, 2019.

Thomalla, S. J., Moutier, W., Ryan-Keogh, T. J., Gregor, L., and Schütt, J.: An optimized method for correcting fluorescence quenching using optical

backscattering on autonomous platforms, Limnology and Oceanography: Methods, 16, 132–144, doi:10.1002/lom3.10234, 2018.

Thurnherr, A., Visbeck, M., Firing, E., King, B., Hummon, J., Krahmann, G., and Huber, B.: A MANUAL FOR ACQUIRING LOWERED DOPPLER CURRENT PROFILER DATA. In The GO-SHIP Repeat Hydrography Manual: A Collection of Expert Reports and Guidelines. Hood, E.M., C.L. Sabine, and B.M. Sloyan, eds. IOCCP Report Number 14, ICPO Publication Series Number 134., URL `https://www.go-ship.org/Manual/Thurnherr_LADCP.pdf`, 2010.

Thurnherr, A., Symonds, D., and St. Laurent, L.: Processing Explorer ADCP Data Collected on Slocum Gliders using the LADCP Shear Method, in: Currents, Waves and Turbulence Measurement (CWTM), IEE/OES 11th, St Petersburg, FL, USA, 2015.

Thyng, K., Greene, C., Hetland, R., Zimmerle, H., and DiMarco, S.: True Colors of Oceanography: Guidelines for Effective and Accurate Colormap Selection, Oceanography, 29, 9–13, doi:10.5670/oceanog.2016.66, 2016.

Timmermans, M.-L., Toole, J., Krishfield, R., and Winsor, P.: Ice-Tethered Profiler observations of the double-diffusive staircase in the Canada Basin thermocline, Journal of Geophysical Research, 113, doi:10.1029/2008jc004829, 2008.

Todd, R. E., Rudnick, D. L., Mazloff, M. R., Davis, R. E., and Cornuelle, B. D.: Poleward flows in the southern California Current System: Glider observations and numerical simulation, Journal of Geophysical Research, 116, doi:10.1029/2010jc006536, 2011a.

Todd, R. E., Rudnick, D. L., Mazloff, M. R., Davis, R. E., and Cornuelle, B. D.: Poleward flows in the southern California Current System: Glider observations and numerical simulation, Journal of Geophysical Research, 116, doi:10.1029/2010jc006536, 2011b.

Todd, R. E., Rudnick, D. L., Sherman, J. T., Owens, W. B., and George, L.: Absolute Velocity Estimates from Autonomous Underwater Gliders Equipped with Doppler Current Profilers, Journal of Atmospheric and Oceanic Technology, 34, 309–333, doi:10.1175/jtech-d-16-0156.1, 2017.

Torres, R. and Barton, E.: Onset of the Iberian upwelling along the Galician coast, Continental Shelf Research, 27, 1759–1778, doi:10.1016/j.csr.2007.02.005, 2007.

Turrell, W. R., Slesser, G., Adams, R. D., Payne, R., and Gillibrand, P. A.: Decadal variability in the composition of Faroe Shetland Channel bottom

water, Deep Sea Research Part I: Oceanographic Research Papers, 46, 1–25, doi:10.1016/s0967-0637(98)00067-3, 1999.

van Aken, H. M.: The hydrography of the mid-latitude Northeast Atlantic Ocean, Deep Sea Research Part I: Oceanographic Research Papers, 47, 789–824, doi:10.1016/s0967-0637(99)00112-0, 2000.

van der Boog, C. G., Dijkstra, H. A., Pietrzak, J. D., and Katsman, C. A.: Double-diffusive mixing makes a small contribution to the global ocean circulation, Communications Earth and Environment, 2, doi:10.1038/s43247-021-00113-x, 2021a.

van der Boog, C. G., Koetsier, J. O., Dijkstra, H. A., Pietrzak, J. D., and Katsman, C. A.: Global dataset of thermohaline staircases obtained from Argo floats and Ice-Tethered Profilers, Earth System Science Data, 13, 43–61, doi:10.5194/essd-13-43-2021, publisher: Copernicus GmbH, 2021b.

You, Y.: A global ocean climatological atlas of the Turner angle: implications for double-diffusion and water-mass structure, Deep Sea Research Part I: Oceanographic Research Papers, 49, 2075–2093, doi:10.1016/s0967-0637(02)00099-7, 2002.